Rise of Titans, Silence of Emptiness

Exploring the Cosmic Dichotomy of Halos and Voids

Author:
Fabian Gunnink
s4144775

Supervisors:
Prof. dr. Rien van de Weygaert
Prof. dr. Saleem Zaroubi

A thesis submitted in partial fulfillment
of the requirements for the degree of
Bachelor of Science
in
Astronomy

Faculty of Science and Engineering
University of Groningen
Groningen, The Netherlands

2023

Abstract

The universe, a cosmic tapestry of structure and emptiness, houses two contrasting entities that shape its destiny: halos and voids [Bond and Myers 1996]. This thesis delves into the fascinating dichotomy between these cosmic counterparts, with a special emphasis on the enigmatic nature of voids. To gain insight into the large-scale structure of the universe, fully analytical methods are used to derive the evolutionary paths of both voids and halos. This is done by re-deriving the implications of the spherical model and using the results to construct the halo excursion set theory [Gunn and Gott 1972; Press and Schechter 1974; Bardeen et al. 1986; Bond et al. 1991]. Following the work of Sheth and Van de Weygaert 2004, the excursion set formalism is then equipped with a second barrier to incorporate the effects of voids. This reveals a symmetry breaking between halos and voids: voids can be squeezed out of existence by surrounding halos, but no such fate can come upon overdensities [Van de Weygaert and Van Platen 2009]. Using the approach introduced by Lacey and Cole 1993 for halos, an analogous merger tree algorithm is developed for voids. This leads to analytical expressions for the merger and absorption rates for voids of general size, thereby extending the work of Russell 2013. This thesis emphasizes the profound significance of voids in shaping the cosmic panorama, providing valuable insights into the cosmic order, and aims to contribute to the frontiers of analytical cosmological exploration.

Table of Contents

Introduction

In the cosmic theater, where stars shine and galaxies dance, a gripping drama unfolds. Titans of structure rise, battling the primal forces of gravity and feeling the never-ending tug of the ever-expanding universe, while silent voids patiently await their destiny in the shadows. Harmony does not last long in the celestial ballroom. Sooner or later, overdense halos combine their forces in merger events and eradicate any enclosed underdense voids, destroying all evidence of their existence. This thesis aims to unveil part of this complex interplay, where the clash between creation and nothingness shapes the destiny of the universe itself.

The study of large-scale structures in the universe has captivated scientists for many centuries. Galaxies, clusters, and superclusters have been studied for decades and act as cosmic fossils that preserve information about the universe at the time of their creation [Peebles 1980]. This leads to new insights into growth mechanisms and dynamics, and helps in constraining the values of various cosmological parameters [Allen, Evrard, and Mantz 2011; Hoessel, Gunn, and Thuan 1980; Bahcall and Soneira 1983; Voit 2005]. They offer testing grounds for cosmogonies and help in unraveling the intriguing theories of dark matter and dark energy, without a doubt the two most enigmatic components in the universe [Ryden 2017]. Large-scale structures are not positioned at arbitrary points in the universe: on the megaparsec scale, they form a complex network of sheets, filaments and clusters, interconnected by vast, seemingly empty pockets [Fabian 1992; Bond and Myers 1996]. This labyrinthine structure is often dubbed the cosmic web. The cosmic voids are characterized by their underdensity relative to the average density of the universe, turning them in a way into mirror images of the cosmic halos. The dynamics of halos and voids, however, are inherently different.

Halos are effectively gravity wells: the more matter is trapped in a region, to stronger the pull on closely lying material will be. In the case of a static universe, in which the gravitational interaction governs the dynamics on the largest scales, this would lead to a positive feedback loop: all the matter in the universe would concentrate in a small region. This does not necessarily mean that the density at a single point skyrockets to infinity, for the conservation of energy and angular momentum might forbid this. Instead, a new equilibrium is found that is often referred to as virtualization [Sparke and Gallagher 2007]. In the case of an expanding universe, the Hubble expansion should also be taken into account. This leads to the so-called Hubble flow, which drags matter along and increases the proper distances between objects [Ryden 2017]. These two external factors govern the structure formation of overdensities. In case two such halos come close together, they might combine their masses in merger or accretion events, a process reminiscent of two soap bubbles combining into one.

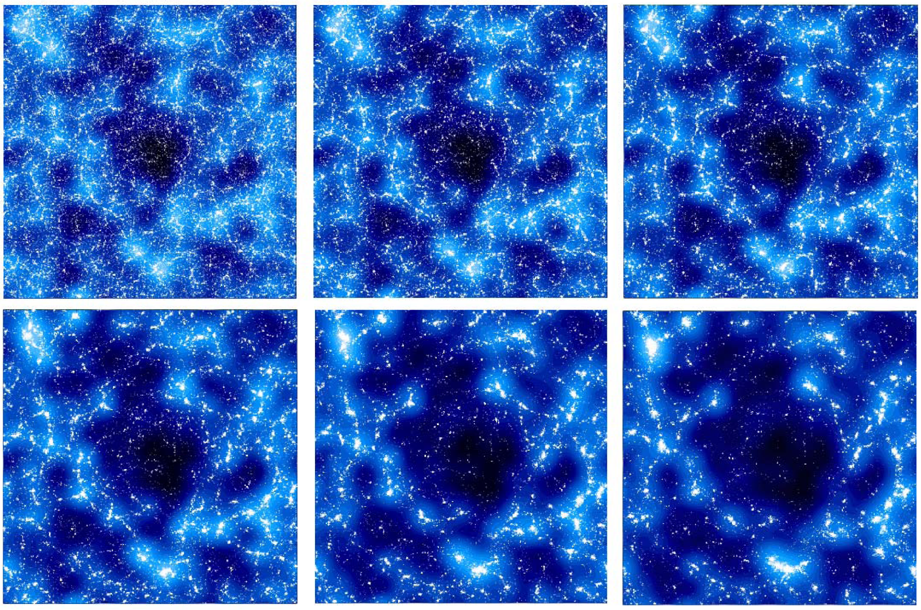

Figure 1: Growing voids. The six panels shows the time evolution of a growing void, as predicted by a numerical simulation of a ΛCDM universe. The blue regions represent smoothed density distributions. The empty, dark regions shown in the panels slowly expand as time progresses. From left-to-right, top-to-bottom, the panels correspond to the different times $a = 0.05, 0.15, 0.35, 0.55, 0.75$ and 1.0. Image courtesy: Erwin Platen.

While halos represent overdensities and fight against the overall Hubble expansion by means of their gravitational pull, voids are effectively left to their own devices since they lack a grip on the environment to keep themselves together. In other words, underdense regions tend to expand at a higher rate than the universal Hubble expansion, inevitably leading to voids blowing up in size over time [Van de Weygaert and Van Platen 2009]. The effective negative gravity found inside voids is stronger near the center. Matter close to the center hence experiences an outward push stronger than matter near the edge, which is why this evolution is sometimes dubbed an inside-out expansion. This so-called evacuation leads to a certain density profile that determines the moment at which the inner shells of the void surpass the outer regions, known as shell-crossing.

Two physical processes particularly relevant to the evolution of voids are merging and collapsing [Van de Weygaert and Van Platen 2009]. Consider the merging of two voids in the cosmic web that are separated by a filament of overdense matter. For this to happen, the two voids push on the matter strand in opposing directions, such that the material is pushed into thin filaments acquiring a velocity component tangential to the void boundaries. While these overdense regions slowly fade, the voids combine to form a single larger underdensity. The second process is particular to voids as it has no analog for their overdense siblings: a small-sized void may collapse when an underdense region is part of a larger overdense structure. When the latter collapses under the influence of their own gravity, the smaller voids contained in the halo are reeled into the regions of ever-increasing density. This ultimately leads to a point where the void is shrinking in size, until there simply no longer is an underdense region: the void has been squeezed out of existence. Voids are after all relatively empty regions in space that can be filled by matter, while halos are overdense objects whose content cannot suddenly disappear. In other words, halos always survive in voids, but the converse is not necessarily true. This dissimilarity will play a crucial role in the last chapter of this work. Over- and underdensities in the universe might seem like simple mirror images at first glance: halos collapse and voids undergo an inside-out expansion and undergo interactions with the external Hubble flow and with themselves through merging. However, this symmetry is broken due to the halos being able to eradicate voids found in overdense regions. The largest voids have little to fear: for them to disappear, they would need to be enclosed by an even larger overdensity, which might be rare. This collapsing mechanism is therefore of particular importance for the smallest voids.

Many current and upcoming surveys are designed and optimized to extract constraints on cosmological parameters from the overdense regions. Voids, however, play a crucial role in understanding the large-scale structure of the universe and fill 95% of the total galaxy distribution [Kirshner et al. 1981; Geller and Huchra 1989; da et al. 1994]. They form a prominent aspect in the megaparsec universe, whose evolution needs to be understood to predict the history and dynamics of the cosmic web itself [Van de Weygaert and Bond 2008]. Due to their unique low-density landscape, they also form the perfect playground to test theories on diffuse components such as neutrinos and dark energy, and on modified theories of gravity [Pisani, Massara, and Spergel 2019]. Studying the spatial distribution of voids, as well as their sizes and density profiles, provides an unprecedented opportunity to uncover many of the lingering mysteries in astronomy.

The aim of this thesis is to shine a light on the mechanisms by which halos and voids grow, how their evolution can be modeled mathematically, and what this implies for their statistics. Throughout this work, the emphasis will be on voids, given their recent increase in popularity to study cosmological parameters. Chapter 1 lays the foundation for the initial conditions for structure growth in the universe by means of Gaussian Random Fields [Bardeen et al. 1986; Adler 2009]. The next chapter reviews the theory behind linearized gravity, which is often invoked in structure formation theory to determine the evolution of complex mass distributions. The third chapter combines the results of the first two chapters and introduces a key model when analytically describing halos and voids, known as the Spherical Model. This opens up the possibility to predict when overdensities collapse to halos and when underdensities turn into cosmic voids. These three chapters form the key ingredients to analyze the time evolution of the seeds laid out by the initial density field. Further halo statistics are explored by means of the Press-Schechter theory and Excursion Set formalism in chapter 4. Chapter 5 concludes this thesis by introducing the Extended Excursion Set formalism by [Sheth and Van de Weygaert 2004], which is applicable to voids, and analyzes the differences between over- and underdense regions using the Lacey & Cole formalism [Lacey and Cole 1993].

Chapter 1

Gaussian Random Fields

Within the natural sciences, in particular the field of cosmology, understanding how spatial and angular correlations arise in the context of field fluctuations is a key element to unveiling the structure of the Universe, and is essential to recognize the interconnectedness of different branches of physics. The discovery of the Cosmic Microwave Background (CMB) has led to well-known cosmological inflationary theories [Guth 1981; Linde 1982; Hawking 1982; Starobinsky 1982]. The inflationary epoch is characterized by the rapid expansion of the primordial universe, due to which its size increased by approximately 60 e-foldings in 10^{-34} seconds, with the specific details depending on particular model at hand [Ryden 2017]. This shows the existence of an intrinsic connection between the physics at the smallest scales, governed by quantum field theories (QFTs), and that at the largest scales, described by General Relativity (GR), all connected through the theory of inflation [Liddle and Lyth 2000; Brandenberger 2011]. In other words, analyzing and understanding the statistics of field fluctuations is, evidently, a fruitful approach to unveiling the artwork of the Universe.

This chapter is structured as follows. In the first section, the initial conditions for the density field are explained through the theory of Gaussian Random Fields. The subsequent section deals with the question of how these statistics are shaped by the so-called correlation function. After representing the same quantities in Fourier space in the next section, it becomes clear that Gaussian Random Fields are surprisingly simple mathematical objects. To pave the way for the halo and void analysis in later chapters, the concepts of filter function and smoothed density fields are introduced in the last section.

1.1 The Primordial Density Field

In order to describe the fluctuation fields, the natural generalization of the Gaussian distribution comes into play: Gaussian Random Fields (GRFs) [Bardeen et al. 1986; Adler 2009; Peacock 1999]. In the same way that a normal distribution $P(x)$ might describe the probabilistic nature of some random variable x, a GRF $\phi(\vec{x})$ contains the statistics of infinitely many random variables positioned at each point $\vec{x}$ in real space[1] . Just as in the case of Gaussian distributions, one can calculate statistical moments such as the mean $\overline{\phi}$ or standard deviation σ for GRFs. Any field can thereby be decomposed into two components:

$$\phi(\vec{x}) = \overline{\phi} + \widetilde{\phi}(\vec{x}), \tag{1.1}$$

where $\widetilde{\phi}$ represents the fluctuation on top of the mean background value $\overline{\phi}$. There are numerous examples of scientific niches in which this type of random field is employed, examples ranging from statistical physics [Rubi and Bedeaux 1988; Cardy 1996], ergodic theory [Katok and Hasselblatt 1995], computational molecular biology [Shutta et al. 2022] to computer vision [Roth and Black 2005; Boykov and Funka-Lea 2006].

One of the main actors in this thesis will be the density fluctuation field δ defined by:

$$\delta(\vec{r}, t) \equiv \frac{\rho(\vec{r}, t) - \overline{\rho}(t)}{\overline{\rho}(t)}, \tag{1.2}$$

and is constructed from the primordial density field ρ [Bardeen et al. 1986; Van de Weygaert 2020; Ryden 2017]. A high value of $\rho(\vec{r})$ reflects a high concentration of mass at $\vec{r}$, while a value close to zero is indicative of the absence of any matter. The density background value $\overline{\rho}$ depends on the cosmological parameters and models used. For instance, in an Einstein-de Sitter (EdS) universe, the mean density would be the critical density ρ_c:

$$\overline{\rho} = \rho_c = \frac{3H_0^2}{8\pi G}, \tag{1.3}$$

with H_0 the Hubble constant and G Newton's gravitational constant [Ryden 2017]. In this context, $\delta(\vec{r})$ can hence be interpreted as the dimensionless fluctuation amplitude or the normalized density excess or shortage relative to the background of the current cosmology. Note also the range of $\delta(\vec{r})$: it is bounded from below by -1, meaning that space is completely free of matter at position $\vec{r}$. Values lower than this threshold make no sense, since this would mean a location is effectively 'emptier than empty'. On the other end, δ has no upper limit, since there is no threshold for the maximum matter density at any position in the field.

The primordial density fluctuation field δ is often taken to be a GRF. Before the full mathematical toolbox for GRFs is assembled, it might be wise to pause and question on what grounds this statement is justified. First and foremost, in the current models for the inflationary epoch, blown-up quantum fluctuations act as a seed for the inhomogeneous distribution of matter and subsequent structure formation [Guth 1981; Peebles 1980]. The Gaussianity of the primordial density field is thereby directly inherited from the statistics of vacuum fluctuations, which are often assumed to constitute a GRF [Coles 2014]. A second argument in favour of the density

---

[1] Of course, the field ϕ might also have a temporal dependence. This case will be relevant in later sections and will be denoted by $\phi(\vec{r}, t)$.

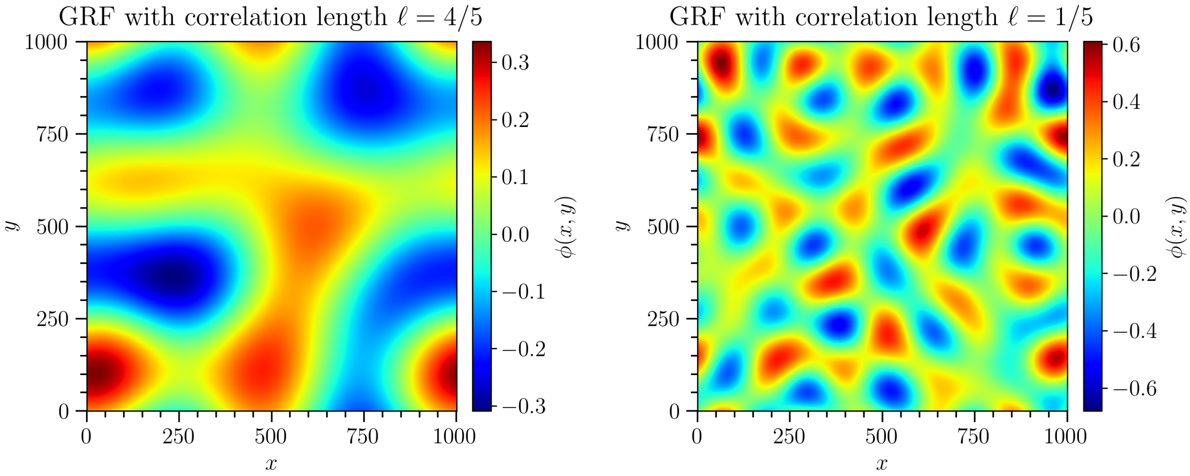

Figure 1.1: Plots showing a Gaussian Random Field with the two-point correlation function $\xi(|\vec{x}_1 - \vec{x}_2|) = \cos(2\pi\,|\vec{x}_1 - \vec{x}_2|\,/\ell)$. The parameter ℓ can be interpreted as a correlation length. GRFs are generated for values of $\ell = 4/5$ and $1/5$.

field being a GRF arises from the Central Limit Theorem: a variable that can be written as the linear combination of many independent random variables, all drawn from the same distribution, tends towards a Gaussian in the limit of large numbers. The cumulative effect of a myriad of microscopic fluctuations would transform the primordial density field into a GRF [Bardeen et al. 1986; Narayanan and Croft 1998]. Mathematically speaking, a GRF is a relatively simple object to work with: all of its higher-order moments can be described using the first- and second-order moments only. This opens up the possibility to perform a statistical analysis fully analytically.

1.2 Correlation Functions

Besides the well-known mean and standard deviation moments of any distribution, GRFs are characterised by their correlation functions. An N-point equal-time correlation function takes N random points in the GRF ϕ and returns the averaged value:

$$\begin{aligned} &\text{Two-point correlation function:} && \langle \phi(\vec{x}_1)\,\phi(\vec{x}_2)\rangle \\ &\text{Three-point correlation function:} && \langle \phi(\vec{x}_1)\,\phi(\vec{x}_2)\,\phi(\vec{x}_3)\rangle \\ &N\text{-point correlation function:} && \langle \phi(\vec{x}_1)\,\phi(\vec{x}_2)\,\ldots\,\phi(\vec{x}_N)\rangle \end{aligned}$$

This generalizes the concept of the Nth moment of a distribution by allowing $\vec{x}_1, \vec{x}_2 \ldots \vec{x}_N$ to be different vectors. By invoking the Cosmological Principle, we enforce the field δ to be statistically homogeneous and statistically isotropic [Ryden 2017]. As a direct consequence, the correlation function must be invariant under translations to respect homogeneity and be invariant under rotations to uphold isotropy. The resulting isometric state requires the correlation function to only depend on the separation between its input points, rather than their absolute locations. In other words, the physics at play governing the density fluctuations has no preference for specific points nor particular directions.

These two symmetries simplify the mathematics of correlation functions. For instance, the two-point correlation function transforms into:

$$\langle \phi(x_1)\,\phi(x_2)\rangle \equiv \xi(\vec{x}_1\,\vec{x}_2) = \xi(|\vec{x}_1 - \vec{x}_2|). \tag{1.4}$$

Note especially how in a 3-dimensional setting, ξ initially depended on 6 coordinates, 3 for each vector, and now simplifies to only depend on one unknown. Likewise, a three-point correlation function reduces from 9 independent input variables to only 3. Moreover, in the special case of a GRF, for an integer $k > 0$ the correlation function between $2k+1$ points is identically zero, in line with the fact that all odd moments of a 1D Gaussian distribution vanish after the mean. All higher-order even moments are determined by the standard deviation and carry no new statistics. GRFs are therefore completely characterized by their two-point correlation functions. Fig. 1.1 shows two examples of a GRF with slightly different two-point correlation functions of the form $\xi(|\vec{x}_1 - \vec{x}_2|) = \cos(2\pi\ |\vec{x}_1 - \vec{x}_2|\,/\ell)$, with $\ell = 4/5$ and $1/5$.

1.3 Fourier Decomposition

Until now, the GRFs were described in real space. It is enlightening to view the same objects from the view of frequency space via a Fourier transform. The fluctuations are then to be regarded as a linear superposition of simple waves, described by their wavevector $\vec{k}$. As will be calculated in more detail later, one of the reasons of performing this transformation is because the equations of motion for small fluctuations on the Friedmann–Robertson-Walker-Lemaître metric can be linearized, for which the Fourier modes will act independently. In other words, Fourier modes are the preferred basis when describing the density fluctuations in a near-flat universe [Van de Weygaert 2020; Scoccimarro 2021]. There exist different conventions on the definition of the Fourier transform. This work will abide the following rules for the forward and inverse transformations:

$$\phi(\vec{x}) = \int \frac{\mathrm{d}\vec{k}}{(2\pi)^3}\ \hat{\phi}(\vec{k})\ e^{-i\vec{k}\cdot\vec{x}} \tag{1.5}$$

$$\hat{\phi}(\vec{k}) = \int \mathrm{d}\vec{x}\ \phi(\vec{x})\ e^{i\vec{k}\cdot\vec{x}}, \tag{1.6}$$

where ϕ is a general field, though this will often come back to be the density fluctuation field δ. In the way that $\delta(\vec{x})$ refers to the density fluctuation at position $\vec{x}$, $\delta(\vec{k})$ refers to the contribution to the field of a wave with wavevector $\vec{k}$.

The power spectrum P is a function of the wavevector $\vec{k}$ defined by the following relation:

$$(2\pi)^3 P(\vec{k})\delta_D(\vec{k}_1 - \vec{k}_2) = \langle \hat{\phi}(\vec{k}_1)\hat{\phi}^*(\vec{k}_2)\rangle, \tag{1.7}$$

Its relation to the correlation function ξ becomes apparent upon expanding ϕ in terms of its Fourier decomposition:

$$\begin{aligned}
\xi(\|\vec{x}_1 - \vec{x}_2\|) &= \langle \phi(\vec{x}_1)\cdot\phi^*(\vec{x}_2)\rangle && (1.8)\\
&= \int\int \frac{\mathrm{d}\vec{k}_1}{(2\pi)^3}\frac{\mathrm{d}\vec{k}_2}{(2\pi)^3}\ \left\langle \hat{\phi}(\vec{k}_1)\ \hat{\phi}^*(\vec{k}_2)\right\rangle\ e^{-i\vec{k}_1\cdot\vec{x}_1}\ e^{i\vec{k}_2\cdot\vec{x}_2} && (1.9)\\
&= \int \frac{\mathrm{d}\vec{k}}{(2\pi)^3}\ P(k)\ e^{-i\vec{k}\cdot(\vec{x}_1 - \vec{x}_2)}. && (1.10)
\end{aligned}$$

In other words, with the definition of the power function $P(\vec{k})$ as in Eq. 1.7, it becomes clear that the correlation function ξ is nothing but the Fourier transform of P. Within the field of applied mathematics, this is sometimes referred to as the Wiener–Khinchin theorem [2] [Wiener 1930]. The standard deviation of the field σ comes in via $\sigma^2 = \langle \delta(\vec{x})^2 \rangle - \langle \delta(\vec{x}) \rangle^2 = \xi(\|\vec{x} - \vec{x}\|) = \xi(0)$, since the mean of the fluctuations $\langle \delta(\vec{x}) \rangle$ ought to be null. This second-order moment can therefore rewritten using the power function as:

$$\sigma^2 = \int \frac{\mathrm{d}\vec{k}}{(2\pi)^3} \, P(k). \tag{1.11}$$

$P(k)$ quantifies the contribution to the total deviation σ^2 via the spatial frequencies $\vec{k}$ [Van de Weygaert 2020].

The Fourier mode $\hat{\phi}(\vec{k})$ will generally be a complex quantity. Using the complex plane, this mode may therefore be written as:

$$\hat{\phi}(\vec{k}) = |\hat{\phi}(\vec{k})| e^{i\varphi(\vec{k})}, \tag{1.12}$$

where $|\hat{\phi}(\vec{k})|$ denotes the distance to the origin and $\varphi(\vec{k})$ is the angle with the positive real axis. GRFs have the special property that the real and imaginary parts of $\hat{\phi}(\vec{k})$ are independently distributed [Coles 2014]. Equivalently, the phase factor $\varphi(\vec{k})$ takes on truly random values within the interval $[0, 2\pi)$. This remains true for small perturbations of the field, in particular when considering linearized gravity, but fails for larger deviations [Peebles 1980]. Non-linear gravitational interactions between the regions in the density field causes the Fourier mode phases to slowly couple together, such that the evolving field no longer is a GRF.

1.4 The Power-Law

The power spectrum is shaped by physical processes having effects of various strengths on different $\vec{k}$. The theory of inflation suggests that the primordial density fluctuation field is described by a power spectrum of the form:

$$P(k) \propto k^n, \tag{1.13}$$

where $n \approx 1$ is the spectral index [Guth 1981; Ryden 2017]. The special case when $n = 1$ is often referred to as the scale-invariant or Harrison-Zeldovich power spectrum and was studied before the theory of inflation was introduced [Harrison 1970; Zeldovich 1972; Coles and Lucchin 1995]. Recent results from the Planck satellite from 2018 showed that CMB anisotropy measurements dictate a value of $n = 0.9649 \pm 0.0042$ for the primordial density fluctuation field, making the Harrison-Zeldovich spectrum relevant [Planck Collaboration 2019]. The initial spectral index will non-trivially evolve under the influence of both gravitational and non-gravitational interactions. Before recombination, interactions such as silk damping, free streaming and the Meszaros effect could alter the functional form of $P(k)$, while the distribution of dark matter is mainly of importance when the density perturbations start to grow significantly under gravity [Coles 2014; Ryden 2017; Peebles 1980]. Other non-gravitational effects include baryon and photon pressure and Jeans damping and oscillation. [Van de Weygaert 2020]

---

[2] Interestingly, the theorem was proved by Norbert Wiener in 1930 and later extended by Aleksandr Khinchin in 1932, but it was Albert Einstein that explained, though without proof, the idea behind this relation already in 1914 [Wiener 1930; Champeney 1987; Einstein 1914].

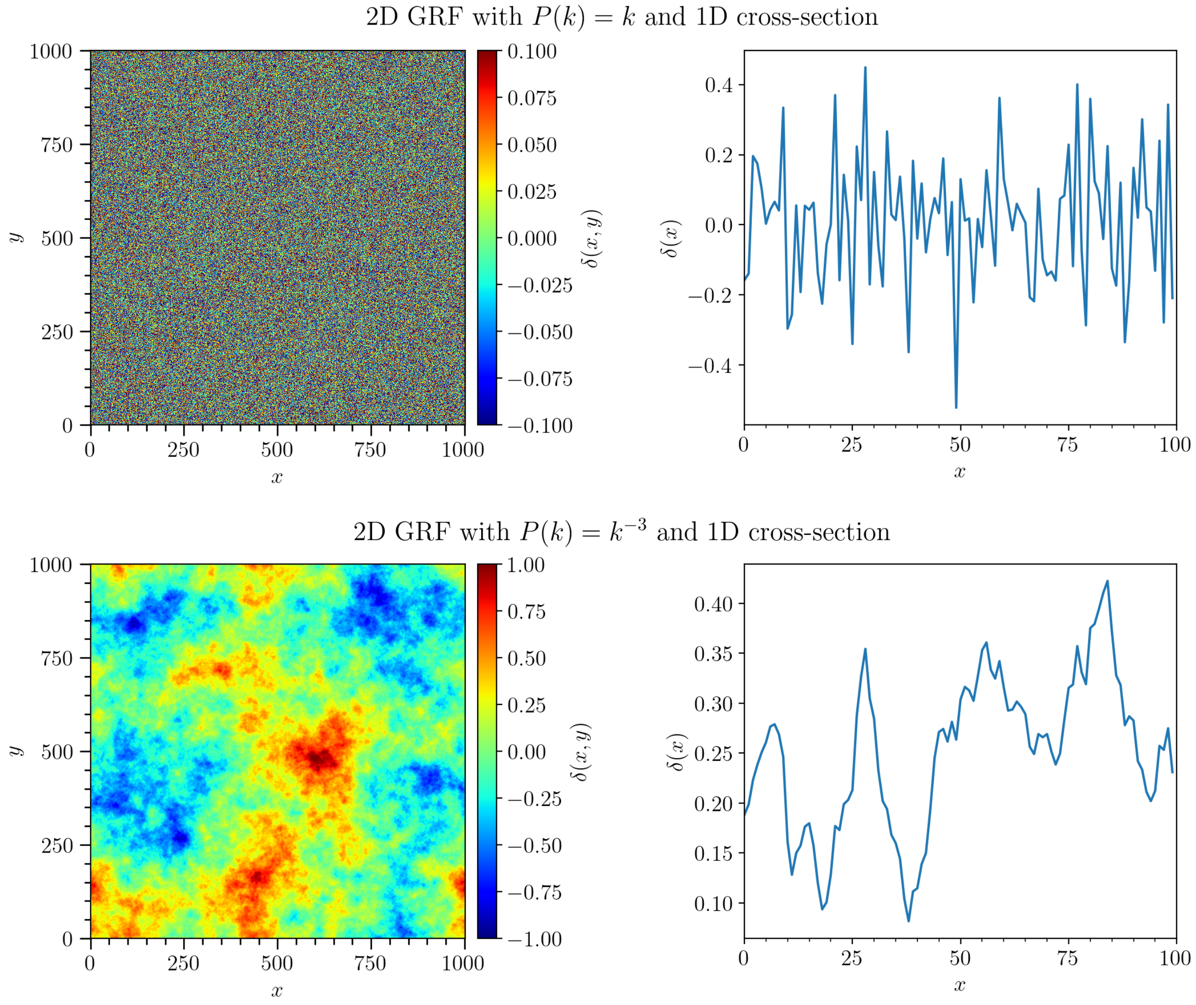

Figure 1.2: Two examples of 2D GRFs with a power-law as power spectrum, with spectral indices $n = 1$ and $n = -3$ respectively. In each row, the left-hand side shows a realization of a GRF with $P(k) = k^n$ and the right-hand side shows an arbitrary slice of this field. Note in particular that for $n = -3$, the power is dominated by the large k-values. For the $n = 1$ scenario, also the smaller fluctuations contribute to the total power significantly.

Two examples of 2D GRFs with power-laws as power spectra, as well as an arbitrary 1D cross-section, are shown in Fig. 1.2. From the slices through the density fluctuation field, it becomes clear that for $n = -3$ the largest waves dominate the power in the field. The small-scale fluctuations have a significant contribution to the power in the case that $n \approx 1$. This can be related to two different ways in which structure formation could take place. In the top-down scenario, the larger waves are more important in the sense that they have higher amplitudes. Here, the large-scale waves collapse on shorter time scales than that the small-scale fluctuations can condensate into smaller structures. Consequently, the larger objects emerge from the field first, after which they might break down into smaller clumps. This relates to the scenario visualized in the second row of Fig. 1.2. In the bottom-up scenario, also referred to as hierarchical clustering, small-scale waves have higher amplitudes than larger waves. The former dominate the observed fluctuations and collapse first. This means that smaller objects start to emerge from the field, then collide under gravity to form larger structures. Reality can be a mixture of both processes, which happens for example in the scale-invariant case where $n = 1$. In Fig. 1.2 this is depicted in the first row.

Based on the continuity and Poisson equation for fluids in an expanding universe, one can relate the power spectrum $P(k)$ for the density fluctuation field to the power spectra $P_v(k)$ and $P_\phi(k)$ for the velocity and gravitational potential fields, respectively. The main conclusion states that [Van de Weygaert 2020]:

$$P(k) \propto k^2 P_v(k) \propto k^4 P_\phi(k). \tag{1.14}$$

The implication is that the density perturbation spectrum is more sensitive to small-scale fluctuations. Likewise, the gravitational potential perturbation spectrum is most sensitive to large-scale fluctuations. Using Eq. 1.11, the fluctuation in the gravitational potential field ϕ can be explicitly calculated in the case that $P(k)$ takes on a power-law with general spectral index n:

$$\sigma_\phi^2 = \int \frac{\mathrm{d}\vec{k}}{(2\pi)^3} P_\phi(k) \propto \int \frac{\mathrm{d}k}{2\pi^2} \frac{P(k)}{k^2} = \int \frac{\mathrm{d}\ln k}{2\pi^2} k^{n-1}. \tag{1.15}$$

If $n = 1$, then this transforms into the simpler relation:

$$\sigma_\phi^2 \propto \int \frac{\mathrm{d}\ln k}{2\pi^2}, \tag{1.16}$$

hence the contribution to the gravitational potential perturbations is the same for each logarithmic bin. Each scale is thereby equally strong for the Harrison-Zeldovich spectrum. For the fluctuations in the density field, Eq. 1.11 can once again be invoked combined with a general power-law power spectrum:

$$\sigma^2 = \int \frac{\mathrm{d}\vec{k}}{(2\pi)^3} P(k) = \int \frac{\mathrm{d}\ln k}{2\pi^2} k^3 P(k). \tag{1.17}$$

In this case, one may view $k^3 P(k)$ as the power per logarithmic frequency band $\mathrm{d}\ln k$. Note in particular that this integral might not converge, based on how P depends on k. One way to circumvent this problem is by introducing filter functions, which act as an indicator or weighting functions to limit the range in k over which P is integrated. This way, diverging integrals are replaced by finite values such that σ^2 is still well-defined.

1.5 Filter Functions

Random fields can be filtered to more easily extract information about scales and size distributions. Integrals that previously diverged due to the infinite integration volume, might become finite again by slightly adapting the field that is being integrated over. For instance, integrating a density field with a non-zero mean over an infinite volume has no chance of limiting to a finite value, but when the field is multiplied by an indicator function that is only non-zero in some finite region, the same integral gives the total mass contained in this area. This example illustrates the first of three commonly used window functions, the top-hat filter of size R:

$$W_{\mathrm{TH}}(\vec{x},\vec{y},R) = \begin{cases} 1 & \text{if } \ \|\vec{x}-\vec{y}\| \ < R \\ 0 & \text{otherwise} \end{cases} \tag{1.18}$$

The top-hat filter extends the Heaviside step function to a higher-dimensional, spherically symmetric case. The function smoothens the field δ by averaging the contribution to the field in an N-sphere of radius R centered at some point $\vec{r}$, resulting in the filtered random field δ_f:

$$\delta_f(\vec{r}) = \int \mathrm{d}\vec{x}\ \delta(\vec{x})\ W_{\mathrm{TH}}(\vec{x},\vec{r},R). \tag{1.19}$$

Instead of using R as the scale parameter of the window function, one might just as well relate to different scales using the typical mass $\overline{M}_f$, related to R via the typical density:

$$\overline{M}_f \equiv \int \mathrm{d}\vec{x}\ \overline{\rho}(\vec{x})\ W(\vec{x},R) = \frac{4\pi}{3}\overline{\rho}R^3. \tag{1.20}$$

Similar to probability density functions, the filter function itself should be normalized to unity to be able to sensibly compare certain results. Eq. 1.18 should therefore be multiplied by the inverse of the volume of the non-zero region, in this case $3/4\pi R^3$. The mass fluctuations smoothened with a normalized filter on mass scale M_f can be shown to be:

$$\begin{aligned} \sigma_M^2 = \frac{\left\langle (M_f - \overline{M}_f)^2 \right\rangle}{\overline{M}_f^2} &= \frac{\left\langle \left\{ \int \mathrm{d}\vec{x}\ \delta(\vec{x}) W_f(\vec{x},R) \right\}^2 \right\rangle}{\left\{ \int \mathrm{d}\vec{x}\ W_f(\vec{x},R) \right\}^2} && (1.21) \\ &= \int \frac{\mathrm{d}\ln k}{2\pi^2}\ k^3\ P(k)\ \hat{W}_f^2(k,R) && (1.22) \\ &= \int \frac{\mathrm{d}k}{2\pi^2}\ k^2\ P(k)\ \hat{W}_f^2(k,R) && (1.23) \end{aligned}$$

Smoothening any field ϕ with some filter function W can also be done in Fourier space using the relations:

$$\phi(\vec{x}) = \int \mathrm{d}\vec{y}\ f(\vec{y}) W^*(\vec{y},\vec{x}) \qquad \text{and} \qquad W(\vec{y}-\vec{x}) = \int \frac{\mathrm{d}\vec{k}}{(2\pi)^3} \hat{W}(\vec{k}) e^{-i\vec{k}\cdot(\vec{y}-\vec{x})}. \tag{1.24}$$

With these conventions, the process of smoothening a random field in Fourier space can be shown to be equivalent to multiplying the Fourier transforms of the field and the window function:

$$\phi(\vec{x}) = \int \frac{\mathrm{d}\vec{k}\ \mathrm{d}\vec{p}\ \mathrm{d}\vec{y}}{(2\pi)^6}\ \hat{\phi}(\vec{k}) e^{-i\vec{k}\cdot\vec{y}}\ \hat{W}^*(\vec{p}) e^{i\vec{p}\cdot(\vec{y}-\vec{x})} = \int \frac{\mathrm{d}\vec{k}}{(2\pi)^3}\ \hat{f}(\vec{k})\ \hat{W}^*(\vec{k}) e^{-i\vec{k}\cdot\vec{x}} \tag{1.25}$$

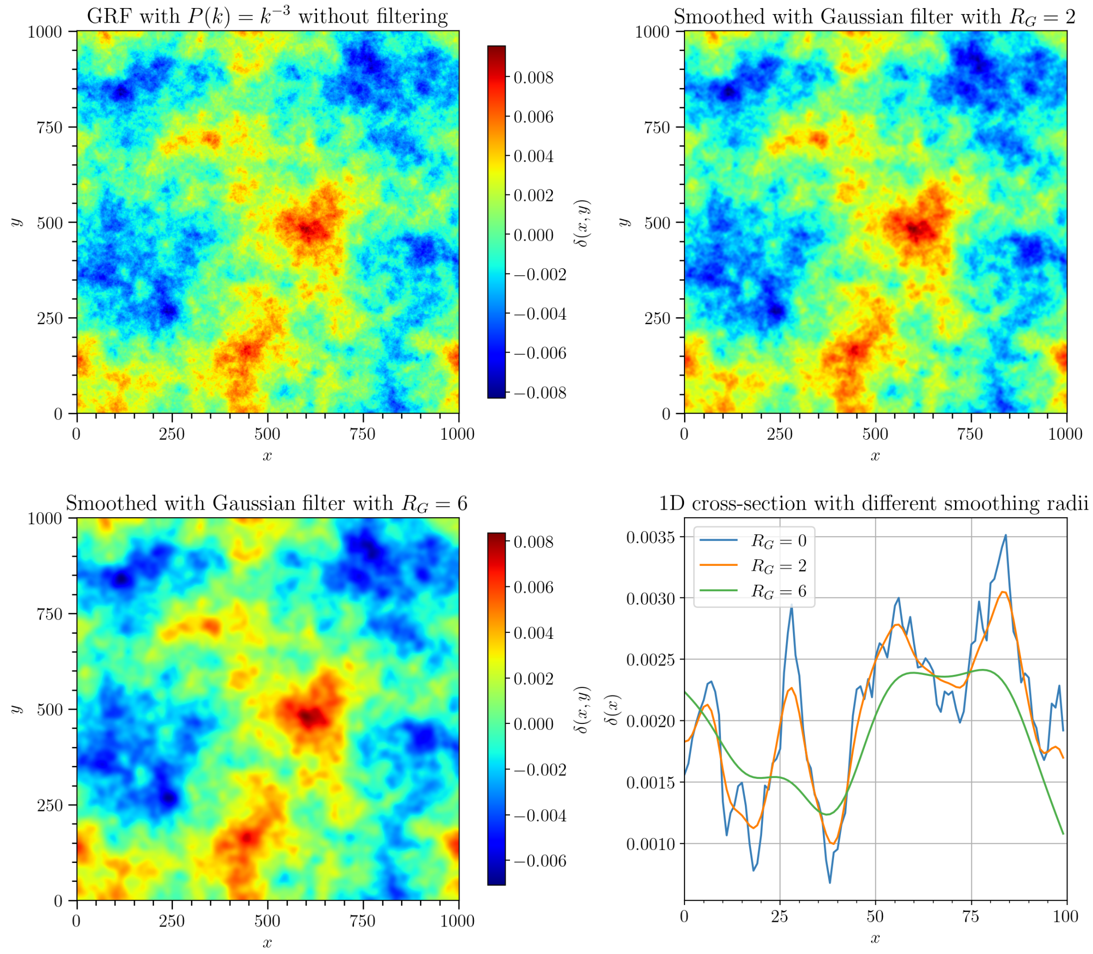

Figure 1.3: Examples of applying a Gaussian filter of various scales to a GRF with $P(k) = k^{-3}$. The first plot shows the unsmoothed GRF ($R_G = 0$), the top-right and bottom-left show the same field with $R_G = 2$ and $R_G = 6$ respectively. The plot on the bottom-right shows the cross-section at an arbitrary pixel, showing that smaller perturbations disappear for increasing filter size.

Calculating the Fourier transform of filter functions is thereby a necessary stepping stone. For instance, in the case of the top-hat filter from Eq. 1.18, the frequency representation is given by:

$$\hat{W}_{\mathrm{TH}}(k) = \int \mathrm{d}\vec{x}\; W_{\mathrm{TH}}(\vec{y}, \vec{x}) e^{i\vec{k}\cdot\vec{x}} = \frac{3\left[\sin\left(kR_{\mathrm{TH}}\right) - kR\mathrm{TH}\cos\left(kR\mathrm{TH}\right)\right]}{(kR\mathrm{TH})^3}. \tag{1.26}$$

One might note that this result is proportional to the spherical Bessel function of the first kind $j_1(kR_{\mathrm{TH}})$. Also note that the real space top-hat function had a clear border at $|\vec{x}| = R_{\mathrm{TH}}$, but that its Fourier transformation lacks such a clear boundary due to its ongoing oscillatory behaviour.

The top-hat filter has a jump discontinuity that could lead to some mathematical difficulties. It is therefore customary to introduce two other filters: the Gaussian filter and the sharp k-space filter. Its definition and Fourier transformation are given by:

$$W_G(\vec{x},\vec{y},R_G) = \frac{1}{(2\pi R_G^3)^{3/2}} \exp\left\{ -\frac{\|\vec{y}-\vec{x}\|^2}{2R_G^2} \right\}, \tag{1.27}$$

$$\hat{W}_G(kR) = \frac{1}{(2\pi R_G^2)^{3/2}} \int \mathrm{d}\vec{x}\ \exp\left\{ -\frac{\|\vec{y}-\vec{x}\|^2}{2R_G^2} \right\} e^{i\vec{k}\cdot\vec{x}} = e^{-k^2 R_G^2/2}. \tag{1.28}$$

Examples of Gaussian filtering can be seen in Fig. 1.3, in which a pure power-law with $n = -3$ GRF is shown, together with smoothened versions using a Gaussian filter with sizes $R_G = 2$ and 6. From an arbitrary cross-section on the bottom-right, it becomes clear that higher R_G hide more of the small-scale behaviour of the fluctuation field. Finally, a sharp k-space filter is essentially nothing but the Fourier transform of the top-hat filter, such that the spherical step-function is now located in k-space:

$$W_k(\vec{x},\vec{y},R_{\mathrm{k}}) = \frac{\sin\left(\|\vec{y}-\vec{x}\|/R_{\mathrm{k}}\right) - \left(\|\vec{y}-\vec{x}\|/R_{\mathrm{k}}\right)\cos\left(\|\vec{y}-\vec{x}\|/R_{\mathrm{k}}\right)}{2\pi^2\|\vec{y}-\vec{x}\|^3}, \tag{1.29}$$

$$\hat{W}_{kR_{\mathrm{k}}}(k) = \begin{cases} 1 & \text{if} \quad k < \dfrac{1}{R} \\ 0 & \text{otherwise} \end{cases} \tag{1.30}$$

This concludes a basic introduction to GRFs, their statistics and their relevance in the field of cosmology. Now that the fundamental quantities are on the table, it is time to take a closer look at how the evolution of the density fluctuation field δ relates to the formation of overdense halos and underdense voids.

Chapter 2

Linearized Gravity

The study of gravity is fundamental to humanity's understanding of the structure and evolution of the universe. In the field of cosmology, the behavior of gravitational interactions on the largest scales is of particular interest, for it provides insights into the evolutionary history of the universe and could be used to test different cosmogonies or constraint the values of cosmology parameters. Linearized gravity, a powerful theoretical framework, provides a mathematical description of the force of gravity within the context of small perturbations around a background spacetime. This chapter explores the concept of linearized gravity through the density fluctuation field and the cosmic fluid equations.

Analytical solutions to the time evolution of arbitrary mass distribution are scarce. In a discrete system, the future paths of two or, in highly exceptional cases, three point masses can be calculated explicitly using Newton's laws of gravitation. Adding more particles to the system generally prevents the system to be solved exactly. However, in the limit towards continuous mass distributions, exact solutions can still be found in highly symmetric configurations. To still get some sense of what happens in systems that cannot be solved analytically, it is fruitful to simplify the non-linear character of gravity to get a system of equations that can be solved exactly. Although only valid under limiting circumstances, these solutions can provide a first insight into the more complex behaviour of a general system. The linear regime focuses on regions in which the density perturbations are small, specifically when $|\delta| \ll 1$, which would depend both on observed scale and time. CMB measurements show that at the time of recombination, the matter perturbations satisfied $|\delta| \lesssim 10^{-5}$, for which the linear theory would be applicable [Burenin 2018; Planck Collaboration 2020a; Mo, Van den Bosch, and White 2010]. However, the ever-lingering pull of gravity has led the universe to become a highly non-linear region, at least on the scale of megaparsecs. On the largest spatial scales, the assumption of the density fluctuations being much smaller than unity becomes applicable again, as suggested by the Cosmological

Principle [Ryden 2017; Mo, Van den Bosch, and White 2010].

This chapter is structured as follows. First, the equations governing the evolution of the density perturbation field δ are explored. Then, after linearizing the system, the focus will be on the linear growth factors in an Einstein-de Sitter universe. These will be crucial in the next chapter, where the spherical model is introduced.

2.1 The Fluid Equations

To infer what equations δ should obey, one should first ask *what* δ describes in the first place. In the current context, this will often be cold dark matter, which is often taken to be a collisionless fluid [Mo, Van den Bosch, and White 2010; Weinberg et al. 2015; Nadler et al. 2019]. It could also describe tightly coupled photons and baryons in the epoch before recombination, or baryons that act like an ideal gas right after recombination. In each of these three cases, the fluid equations seem to come closest to describing the motion of δ. This description would be valid for collisionless fluids in case velocity dispersions are small enough such that physical processes as diffusion can be safely disregarded [Fraternali 2023]. Warm or hot dark matter fails to satisfy these conditions, due to their non-zero peculiar velocities and hence dispersion. The collisionless, pressureless and non-relativistic fluid equations form a set of five equations [Mo, Van den Bosch, and White 2010; Van de Weygaert 2004a]:

$$\begin{cases} \dfrac{\partial\delta}{\partial t} + \dfrac{1}{a}\nabla\cdot(1+\delta)\vec{v} = 0 & \text{Continuity equation} \\ \dfrac{\partial\vec{v}}{\partial t} + \dfrac{1}{a}(\vec{v}\cdot\nabla)\vec{v} + H\vec{v} = -\dfrac{1}{a}\nabla\Psi & \text{Euler equations} \\ \nabla^2\Phi = 4\pi G a^2 \delta\rho_m & \text{Poisson equation} \end{cases} \tag{2.1}$$

with a the scale parameter of the cosmology, $\vec{v}$ the velocity vector, H the Hubble parameter and Ψ the gravitational potential. This coupled system of partial differential equations is reduced in complexity by removing terms that depend on products of δ or $\vec{v}$, on the assumption that both these quantities are small. The result is the system of linearized fluid equations:

$$\begin{cases} \dfrac{\partial\delta}{\partial t} + \dfrac{1}{a}\nabla\cdot\vec{v} = 0 & \text{Continuity equation} \\ \dfrac{\partial\vec{v}}{\partial t} + H\vec{v} = -\dfrac{1}{a}\nabla\Psi & \text{Euler equation} \\ \nabla^2\Phi = 4\pi G a^2 \delta\rho_m & \text{Poisson equation} \end{cases} \tag{2.2}$$

Taking the time derivative of the continuity equation and the divergence of the Euler equation, the first two equations can be combined to give:

$$\frac{\partial^2\delta}{\partial t^2} + 2H\frac{\partial\delta}{\partial t} = \frac{\nabla^2\Psi}{a^2}, \tag{2.3}$$

and where $\nabla\cdot v = -a\frac{\partial\delta}{\partial t}$, which directly follows from the linearized continuity equation. Finally, the Poisson equation can be substituted for a generic cosmology,

$$\frac{\nabla^2\Phi}{a^2} = 4\pi G\delta\rho_m = \frac{3}{2}\Omega_{0,m}H_0^2\frac{\delta}{a^3}, \tag{2.4}$$

such that the fluid equations can readily be combined into one master equation:

$$\frac{\partial^2\delta}{\partial t^2} + 2H\frac{\partial\delta}{\partial t} = 4\pi G\delta\rho_m = \frac{3}{2}\Omega_{0,m}H_0^2\frac{\delta}{a^3}. \tag{2.5}$$

This equation is valid for $\delta \ll 1$ for a non-relativistic pressure-less fluid. The second term on the left represents the so-called Hubble Drag, and quantifies how the expansion of the surrounding environment suppresses perturbation growth. The first term of the right hand side promotes perturbation growth under influence of gravity. Another detail worth mentioning is what happens when taking the Fourier transform on both sides of Eq. 2.5:

$$\frac{\mathrm{d}^2\delta(\vec{k})}{\mathrm{d}t^2} + 2H\frac{\mathrm{d}\delta(\vec{k})}{\mathrm{d}t} = 4\pi G\delta(\vec{k})\rho_m. \tag{2.6}$$

This shows that the ordinary second-order differential equation that each Fourier mode $\delta(\vec{k})$ has to satisfy, makes no reference to any other Fourier mode [Mo, Van den Bosch, and White 2010]. In other words, in the linear theory, each Fourier mode evolves independently, thereby confirming an earlier statement in Chapter 1 [1] . An interesting observation is that Eq. 2.5 only contains derivatives of δ with respect to time, meaning that there seems to be no spatial dependence whatsoever. The spatial and temporal parts of δ behave in their own fashion and can thereby be distilled into two separate factors:

$$\delta(\vec{x},t) = \Delta(\vec{x})D(t), \tag{2.7}$$

where $\Delta(\vec{x})$ is a function depending only on the spatial coordinate, and $D(t)$ a function containing just the temporal variable. $\Delta(\vec{x})$ defines the primordial matter distribution, $D(t)$ governs how this spatial configuration of matter evolves over time and is referred to as the linear density growth factor. Most importantly, the function D is universal in the sense that it applies to all mass configurations at all times, and only applies a straightforward scaling of the initial distribution. In the linearized theory then, mass distributions change in size, not in shape.

2.2 Modes in the Einstein-de Sitter universe

Within an EdS universe, the previous equations simplify under the observation that:

$$\begin{cases} a(t) = \left(\frac{3}{2}H_0 t\right)^{2/3}, \\ H = \frac{\dot{a}}{a} = \frac{2}{3t}, \\ \frac{3}{2a^3}\Omega_{0,m}H_0^2 = \frac{2}{3t^2}. \end{cases} \tag{2.8}$$

In that case, the linearized fluid equation in terms of D transforms into:

$$\frac{\partial^2 D}{\partial t^2} + \frac{4}{3t}\frac{\partial D}{\partial t} = \frac{2}{3t^2}D. \tag{2.9}$$

---

[1] The Fourier transform of the generic master equation that would be valid in the non-linear regime as well, the differential equation contains terms in which quantities are integrated over $\vec{k}$-space [Van de Weygaert 2004b]. These contributions couple the different Fourier modes together and destruct the Gaussianity of the initial GRF.

This leads to two linearly independent solutions D_1 and D_2 [Van de Weygaert 2004a]:

$$D_1(t) \propto t^{2/3} \propto a(t) \quad \text{and} \quad D_2(t) \propto t^{-1/3}. \tag{2.10}$$

The most general solution in terms of the density fluctuation field is thereby a linear combination of the two components:

$$\delta(\vec{x}, t) = \Delta_1(\vec{x}) D_1(t) + \Delta_2(\vec{x}) D_2(t). \tag{2.11}$$

The temporal scale factor D is often normalized to unity at the present epoch t_0:

$$D_1(t) := \left(\frac{t}{t_0}\right)^{2/3} \quad \text{and} \quad D_2(t) := \left(\frac{t}{t_0}\right)^{-1/3}. \tag{2.12}$$

D_1 and D_2 are, respectively, referred to as the growing mode and decaying mode solutions. The total primordial density distribution is split between Δ_1 and Δ_2 which subsequently evolve in their own manner. The contribution of the mass component connected to the decaying mode solution slowly fades away over time and is therefore often omitted in further calculations [Van de Weygaert 2004a]. Note how the growing mode solution, which determines the rate at which the density fluctuation field δ changes over time within the linearized model, exactly mimics the time behaviour of the scale parameter a of the EdS universe. In a universe with $\Omega_{0,m} < 1$, the perturbations would grow at a slower rate since the rate of expansion is larger than inside an EdS cosmology. Moreover, in a static universe the growth would be an exponential, but because of the ongoing Hubble expansion, it is replaced by a power law in expanding cosmological models [Mo, Van den Bosch, and White 2010].

Chapter 3

The Spherical Model: Collapsing Clumps & Expanding Voids

One of the main results of the previous chapter is that the primordial density fluctuation field δ can be described using a GRF. The field evolves over time under the influence of both gravitational and non-gravitational interactions, which, in the non-linear regime, will de-randomize the distribution of the Fourier modes of δ. This mode-coupling causes the field to lose its Gaussianity and hence higher-order moments are required to completely specify the density fluctuation field. In general, no analytic solutions exist that fully describe the evolution of a system of arbitrary shape and properties. Sometimes, light can be shed on only a part of the full solution, through various approximating mathematical techniques. In the linear regime for instance, characterized by $|\delta| \ll 1$, the time evolution of mass distributions can be calculated through first-order perturbative techniques [Peebles 1980; Peacock 1999; Dodelson 2003]. This chapter relates the results of the non-linear regime to the linear theory by considering spherical over- and underdense objects, representing oversimplified halos and voids respectively, living in a universe governed by the FRWL equations. This spherical collapse model can be solved analytically and has important connections with the linearized theory and predictions on the evolution of more generic mass distributions in the universe [Gunn and Gott 1972; Peebles 1980; Padmanabhan 1999; Mo, Van den Bosch, and White 2010]. Although an analogous analysis can be done for more general universes, this derivation adapts the Einstein-de Sitter (EdS) universe with zero curvature and $\Omega_m = 1$.

This chapter is structured as follows. In the first section, the general equations of motion are developed for a spherically symmetric mass distribution. Of particular importance in this section are the implications for the overdense regions, that are on the verge of becoming halos. This is then connected with the results from linearized gravity and leads to the definition of the so-called halo barrier. The second section follows underdense structures, cosmic voids, and relates again their evolution to the linearized theory. This naturally leads to the second threshold, the void barrier. The last section reflects on the shortcomings and general validity of the spherical model.

3.1 The Spherical Collapse Model

This section is largely based on the derivations by Van de Weygaert 1995. Consider first a spherical object placed in an ever-expanding, otherwise homogeneous universe governed by the FRWL equations, described by a sufficiently nice density function ρ. To be more exact, ρ is required to be a function of time t and proper radius r only – that is, the object is only allowed to have a radial structure. The infinitesimally thin 2-sphere at radius r_i will be referred to as a shell. Such mass distributions in an expanding universe are subject to at least two physical processes: the attractive force of gravity between massive particles, and the Hubble expansion of the background [Ryden 2017]. With the assumption that ρ describes the density field of a collisionless fluid, other interactions, such as viscous or other frictional forces, are out of the question [Fraternali 2023]. This makes the spherical model especially relevant for dark matter halos, due to their apparent collisionless behaviour [Mo, Van den Bosch, and White 2010; Weinberg et al. 2015; Nadler et al. 2019]. An identical mass setup composed of baryonic matter immediately introduces more complexity since collisions would transform kinetic energy into heat and form shock waves [Fraternali 2023]. To solve the time evolution of this spherically symmetric system analytically, shells will be assumed not to cross one another, at least not until total collapse. Newton's Shell Theorem for classical mechanics dictates that the evolution of a shell is completely determined by the mass contained within the boundary[1] , so combined with the previous assumption, the mass within each shell will be constant up to shell-crossing [Newton 1687; Arens 1990].

For an object that eventually contracts under gravity, its evolution can be subdivided into different stages. In physical or proper coordinates, the initial density profile initially spreads out under the Hubble expansion. If the gravitational interaction is strong enough, the resulting acceleration toward the center of the sphere decelerates the expansion, until at some cosmological time the sphere's peculiar velocity cancels the Hubble expansion and reaches its maximum proper radius. From this point of turn-around onward, the shells shrink until all of them collapse to a single point in space. Physically speaking, this implies that all the mass of the original distribution is now concentrated at a single point, such that the density skyrockets. Of course, reality would deviate from this model long before this state is reached, but if one insists, then after this shell-crossing the radii of the shells start oscillating harmonically as energy flows from gravitational potential energy into kinetic energy and back. Realistic infalling matter would gain non-radial velocity components that prevent all the matter to concentrate at a single point in space and instead leads to virialization, a state in which kinetic and potential energy come into some sort of balance [Mo, Van den Bosch, and White 2010; Padmanabhan 1999; Lyth and Liddle 2009]. The subsequent analysis focuses on the evolution of shells up until the first full collapse of a spherically symmetric system.

---

[1] This theorem is the Newtonian limit of the more widely applicable Birkhoff's Theorem in GR [Padmanabhan 1996; Straumann 2014].

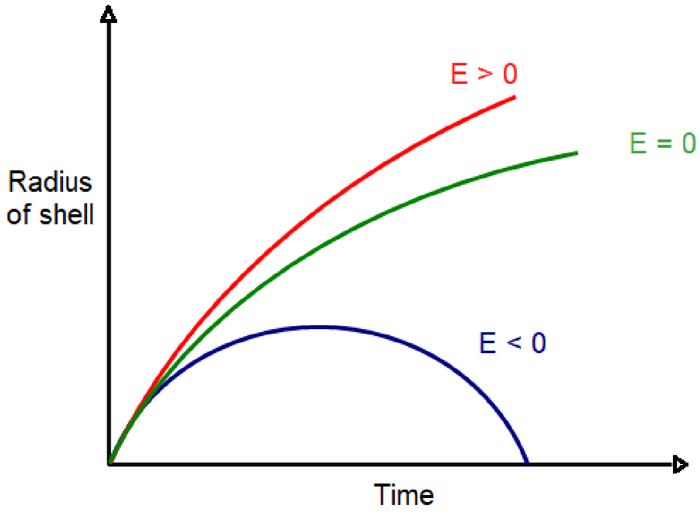

Figure 3.1: Shell evolution. This simple schematic shows the general form of the evolution of the radius of a shell of a given energy E. The red, green and blue curves show the open, critical and closed shells respectively.

3.1.a Equations of Motion

The dynamics of the spherical shell are described by the equations of motion. The first equation of this set comes from combining Newton's second law of classical mechanics with the law of universal gravitation, essentially expressing the Shell Theorem. The second equation is obtained by integrating the first, which introduces an integration constant E:

$$\begin{cases} \frac{\mathrm{d}^2 r}{\mathrm{d}t^2} = -\frac{GM(r)}{r^2}, \\ \frac{1}{2}\left(\frac{\mathrm{d}r}{\mathrm{d}t}\right)^2 - \frac{GM(r)}{r} = E. \end{cases} \tag{3.1}$$

Here, r denotes the proper radius, G Newton's gravitational constant, $M(r)$ the mass contained interior to the shell at radius r. It presents the law of conservation of energy in a spherically symmetric system, where the first term is proportional to the kinetic energy and the second to the internal potential energy of the shell at radius r. The constant E is thereby interpreted as the energy of a shell at radius r. It is interesting to compare the equations of motion in Eq. 3.1 to the set of FRWL equations with scale parameter a for a universe with no cosmological constant [Ryden 2017]:

$$\begin{cases} \frac{\ddot{a}}{a} = -\frac{H_0^2}{2}\frac{\Omega}{a^3}, \\ \left(\frac{\dot{a}}{a}\right)^2 = \frac{H_0^2\Omega}{a^3} - \frac{k}{a^2}, \end{cases} \quad \text{or} \quad \begin{cases} \ddot{a} = -\frac{H_0^2}{2}\frac{\Omega}{a^2}, \\ \frac{1}{2}\dot{a}^2 - \frac{H_0^2\Omega}{2a} = -\frac{k}{2} \end{cases} \tag{3.2}$$

These equations describe the motion of the background in which the spherical mass distribution is placed. In particular, note that the functional form of the system in Eq. 3.1 is identical to that of Eq. 3.2. This implies that the time dependence of the spherical density profile can be interpreted as the evolution of a bubble universe embedded in the background universe.

Similar to orbital mechanics, E can be subdivided into three distinct cases, leading to three types of solutions (also see Fig. 3.1) [Van de Weygaert 1995; Shi 2017]:

1. $E > 0$ (Open shell):
   The shell is said to be unbounded and its equations of motion can be solved to find that:

$$\begin{cases} r(\Phi_r) &= \dfrac{GM}{2E}(\cosh(\Phi_r) - 1) \\ t(\Phi_r) - t_i &= \dfrac{GM}{2E\sqrt{2E}}(\sinh(\Phi_r) - \Phi_r), \end{cases} \tag{3.3}$$

   where Φ_r is the so-called development angle at radius r, ranging from 0 at the initial time to 2π at the final time. Note that the development angle explicitly depends on the radius r.

2. $E = 0$ (Critical shell):
   The critical shell is a perfect balance between the kinetic and potential term in the conservation of energy equation. The solution can be shown to be:

$$r(t) = \left(\frac{9}{2}GM\right)^{1/3}(t - t_i)^{2/3}. \tag{3.4}$$

   In this case, there is no need to parameterize the solution through a development angle.

3. $E < 0$ (Closed shell):
   The shell is said to be bounded and its equations of motion can be solved to find that:

$$\begin{cases} r(\Phi_r) &= \dfrac{GM}{2E}(\cos(\Phi_r) - 1) \\ t(\Phi_r) - t_i &= \dfrac{GM}{2E\sqrt{-2E}}(\sin(\Phi_r) - \Phi_r), \end{cases} \tag{3.5}$$

3.1.b Relating Energy to Expansion & Density

The magnitude of E depends on the strength of the Hubble expansion and on the initial density profile of the spherical region. The mean density excess Δ for the shell at initial radius r_i is used to quantify the latter, and quantifies the relative over- or underdensity of ρ compared to the background $\overline{\rho}$:

$$\Delta(t, r_i) = \frac{3}{4\pi\overline{\rho}(t)r_i^3}\int r'^2 \sin\theta\,(\overline{\rho}(t) - \rho(r', t))\,\mathrm{d}r'\,\mathrm{d}\theta\,\mathrm{d}\phi = \frac{3}{r_i^3}\int_0^{r_i} r'^2\,\delta(r', t)\,\mathrm{d}r'. \tag{3.6}$$

$\Delta(t, r_i)$ is therefore completely determined by the internal mass distribution of the spherical object under consideration. In the case of a spherical mass distribution that is constant up to size $R \geq r_i$, Eq. 3.6 states that simply $\Delta(t, r_i) = \delta$. Two useful definitions are the critical mean density excess $\Delta_{c,i} = \Delta_c(t_i, r_i)$ and kinetic energy measure α_i for a shell at radius r_i:

$$1 + \Delta_{c,i} := \Omega_i[1 + \Delta(t_i, r_i)] \tag{3.7}$$

$$\alpha_i := \left(\frac{v_i}{H_i r_i}\right)^2 - 1, \tag{3.8}$$

where v_i denotes the peculiar velocity in shell r_i, which is then divided by the Hubble expansion term $H_i r_i$. α_i can be interpreted as a quantifier for the initial velocity perturbation. Using these two definitions, one can deduce that the specific energy of a shell can be re-expressed as:

$$E = \frac{1}{2}\left(\frac{\mathrm{d}r_i}{\mathrm{d}t}\right)^2 - \frac{GM(r_i)}{r_i} = \frac{1}{2}(H_i r_i)^2 - \frac{GM(r_i)}{r_i} = \frac{1}{2}(H_i r_i)^2(\alpha_i - \Delta_{c,i}), \tag{3.9}$$

allowing us to make the same subdivision for E as enumerated above, but now in terms of $\Delta_{c,i}$ and α_i. The main interest lies in the sign of E, so if one approximates the initial shell velocity to be mainly composed of the Hubble flow, $v_i \approx H_i r_i$, in Eq. 3.8, then Eq. 3.9 takes on the simpler form:

$$E \approx \frac{1}{2}(H_i r_i)^2 \left(1 - \Omega_i \left[1 + \frac{3}{r_i^3}\int_0^{r_i} r'^2\, \delta(r', t)\, \mathrm{d}r'\right]\right), \tag{3.10}$$

where Eqs. 3.6 and 3.7 were used [Mo, Van den Bosch, and White 2010]. The sign of E is, as expected, determined by Ω and δ only. In the case of an EdS universe $\Omega = 1$, such that E will have exactly the opposite sign compared to δ: any overdensity leads to a bound system and any underdensity is intrinsically linked to an open shell. However, for a more general universe, the fate of the matter distribution also depends on Ω. An overdensity in one open universe ($\Omega < 1$) might have $E > 0$, although the same mass distribution embedded in an EdS will definitely collapse at some finite time. In a sense, this reformulation of E allows one to compare density fluctuations to a common playground: the Einstein-de Sitter universe.

The physical radius r at any subsequent time can be related to the initial physical radius r_i through the linear relation $r(r_i, t) = \mathcal{R}(t, r_i)\, r_i$. This becomes evident when rewriting Eq. 3.9 into:

$$\sqrt{2E} = H_i r_i \sqrt{\alpha_i - \Delta_{c,i}}, \tag{3.11}$$

which is valid for each of the three cases. This allows Eqs. 3.3, 3.5 and 3.4 to be rewritten in terms of $\mathcal{R}$ and $H_i t$ [Van de Weygaert 1995]:

1. $E > 0$ ($\alpha_i > \Delta_{c,i}$, open shell):

$$\begin{cases} \mathcal{R}(t_i, r_i, \Phi_r) &= \dfrac{1}{2}\dfrac{1+\Delta_{c,i}}{\alpha_i - \Delta_{c,i}}(\cosh(\Phi_r) - 1) \\ H_i(t - t_i) &= \dfrac{1}{2}\dfrac{1+\Delta_{c,i}}{(\alpha_i - \Delta_{c,i})^{3/2}}(\sinh(\Phi_r) - \Phi_r), \end{cases} \tag{3.12}$$

2. $E = 0$ ($\alpha_i = \Delta_{c,i}$, critical shell):

$$\mathcal{R}(t, r_i) = \left(\frac{3}{2}H_i(1+\Delta_{c,i})^{1/2}\,(t - t_i)\right)^{2/3}. \tag{3.13}$$

3. $E < 0$ ($\alpha_i < \Delta_{c,i}$, closed shell):

$$\begin{cases} \mathcal{R}(t_i, r_i, \Phi_r) &= \dfrac{1}{2}\dfrac{1+\Delta_{c,i}}{\alpha_i - \Delta_{c,i}}(1 - \cos(\Phi_r)) \\ H_i(t - t_i) &= \dfrac{1}{2}\dfrac{1+\Delta_{c,i}}{(\alpha_i - \Delta_{c,i})^{3/2}}(\Phi_r - \sin(\Phi_r)), \end{cases} \tag{3.14}$$

Of particular interest in the theory of collapse is the evolution of the density profile. In terms of the density deficit, one can show that:

$$1 + \Delta(r, t) = \frac{1 + \Delta_i(r_i)}{\mathcal{R}^3}\left(\frac{a(t)}{a_i}\right)^3 = \frac{f(\Phi_r)}{f(\Phi_u)}, \tag{3.15}$$

where Φ_u is again a development angle, but this time corresponding to the universe in which the spherical object is embedded. The function f depends on the characteristic of the universe, and is given by:

$$f(\Phi) = \begin{cases} \dfrac{(\sinh\Phi - \Phi)^2}{(\cosh\Phi - 1)^3} & \text{if } \ \Omega < 1 \\ \dfrac{2}{9} & \text{if } \ \Omega = 1 \\ \dfrac{(\sin\Phi - \Phi)^2}{(1 - \cos\Phi)^3} & \text{if } \ \Omega > 1 \end{cases} \tag{3.16}$$

3.1.c The Evolution of Closed Shells

The overdense regions are of particular importance for the subsequent analysis in this work, for they represent the seeds of future structure formation. Depicted as the blue curve in Fig. 3.1, the shell reaches a maximum radius before it collapses. Eq. 3.10 dictates that all overdense regions, however small the density perturbation, will collapse at some finite time in an EdS universe. Before full collapse takes place at the development angle $\Phi_{\text{col}} = 2\pi$ and time t_{col}, from Eq. 3.14 it becomes clear that the shell first reaches a maximum scaling at $\Phi_{\text{ta}} = \pi$, which will be referred to as the time of turn-around t_{ta}. Using the deduced relations for $H_i t$, each of these two events can also be linked to a cosmic time:

$$\text{Turn-around:} \quad \begin{cases} \mathcal{R}(t_i, r_i, \Phi_{\text{ta}}) & = \dfrac{1 + \Delta_{c,i}}{\alpha_i - \Delta_{c,i}} \\ H_i t_{\text{ta}} & = \dfrac{\pi}{2} \dfrac{1 + \Delta_{c,i}}{(\alpha_i - \Delta_{c,i})^{3/2}}, \end{cases} \tag{3.17}$$

$$\text{Collapse:} \quad \begin{cases} \mathcal{R}(t_i, r_i, \Phi_{\text{col}}) & = 0 \\ H_i t_{\text{col}} & = \pi \dfrac{1 + \Delta_{c,i}}{(\alpha_i - \Delta_{c,i})^{3/2}} = 2 H_i t_{\text{ta}}, \end{cases} \tag{3.18}$$

Meanwhile, the density evolves in accordance with Eqs. 3.15 and 3.16 with $\Omega = 1$:

$$1 + \Delta(t) = \frac{9}{2} \cdot \frac{(\Phi - \sin\Phi)^2}{(1 - \cos\Phi)^3} \tag{3.19}$$

At the time of turn-around and full collapse, this relation reduces to:

$$1 + \Delta(t_{\text{ta}}) = \frac{9\pi^2}{16} \approx 5.551, \qquad \text{and} \qquad 1 + \Delta(t_{\text{col}}) \to \infty. \tag{3.20}$$

In other words, a top-hat density perturbation switches from the expanding to the collapsing phase precisely when $1 + \Delta(t_{\text{ta}}) \approx 5.551$, independent of the initial density measure Δ_i. This statement does not only hold for the top-hat density profile but works for the shells in a generic spherically symmetric density distribution. For the moment of collapse, the density measure approaches infinity, as previously anticipated. The time at which this happens, as predicted by Eq. 3.18, can also be expressed in terms of the scale parameter a for the EdS universe:

$$H_i t_{\text{col}} = \pi \frac{1 + \Delta_{c,i}}{(\alpha_i - \Delta_{c,i})^{3/2}} = \frac{2}{3} \frac{t}{t_i} = \frac{2}{3} \left(\frac{a}{a_i} \right)^{2/3}. \tag{3.21}$$

With these results, the spherical model has done it's job. It provides fully analytical expressions for the physical radius r, the scaling parameter $\mathcal{R}$ and time measure Ht, and predicts the evolution of the density excess Δ.

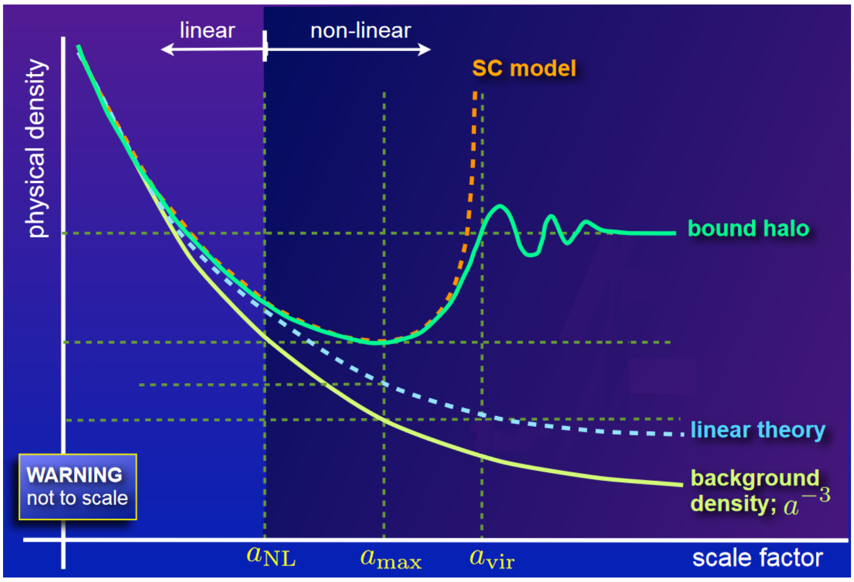

Figure 3.2: Density evolution in the spherical collapse model. Four density curves are sketched: the dashed orange line corresponds to the density evolution the spherical collapse model predicts, the solid green line shows reality in the sense that full collapse is replaced by virialization, the dashed blue line indicates the density predicted by the linear theory, and the solid yellow curve shows the background density. Up to a scale parameter $a_{\rm NL}$, the SC model and linear theory almost coincide. The sphere reaches its maximum radius at $a_{\rm max}$ and reaches collapse at $a_{\rm vir} = a_{\rm col}$. Of particular importance will be the value of the density predicted by the linear theory at this exact moment. Source Van den Bosch 2022.

3.1.d Relation to Linearized Gravity

To relate the linear theory described in the second chapter to the spherical model discussed in the first subchapter, the implications of the growth factors obtained in the linearized theory are applied to the same top-hat mass distribution. Fig. 3.2 shows this process visually. The density profile of the spherical collapse model, indicated by the dashed orange curve, was calculated in the previous section. The next goal is to relate the moment of collapse to the density value of the linearized model, shown by the dashed blue line, by evaluating it at $a_{\rm col}$. The linear regime is valid when $t \to 0$ in the equations governing the evolution of the spherical system, which is equivalent to the limit $\Phi \to 0$. Hence, one can perform a Taylor expansion of Eq. 3.19 around the point $\Phi = 0$ to extract the smallest-order terms:

$$\delta \sim \frac{3}{20}\theta^2 + \frac{37}{3800}\theta^4 + \frac{1}{1120}\theta^6 + \dots \tag{3.22}$$

Retaining only the first term, one can show that [Mo, Van den Bosch, and White 2010]:

$$\delta_{\text{lin},i} = \frac{3}{20}(6\pi)^{2/3}\left(\frac{t_i}{t_{\rm ta}}\right)^{2/3}. \tag{3.23}$$

Taken together with the growing mode D_1 of the EdS universe as deduced in Eq. 2.12, this implies that:

$$\delta_{\rm lin}(t) = \frac{3}{20}(6\pi)^{2/3}\left(\frac{t}{t_{\rm ta}}\right)^{2/3}. \tag{3.24}$$

This equation describes the time evolution of the density perturbation in the linearized setup of the spherical model, as opposed to the true evolution as predicted by Eq. 3.19. For instance, at the time of turn-around t_{ta}, Eq. 3.24 predicts that:

$$\delta_{\text{lin}}(t_{\text{ta}}) = \frac{3}{20}\,(6\pi)^{2/3} \approx 1.062, \tag{3.25}$$

as opposed to the actual value of 4.551 as derived in Eq. 3.20. More importantly, whereas the density at the time of collapse t_{col} reached non-finite values in the spherical model, the linear theory predicts that:

$$\delta_{\text{lin}}(t_{\text{col}}) = \frac{3}{20}\,(12\pi)^{2/3} \approx 1.686. \tag{3.26}$$

The importance of this particular result cannot be overstated. Any region in the universe for which the linearly extrapolated density field exceeds the value of 1.686, should have collapsed to a gravitationally bound object. This value therefore represents the critical density threshold for structure formation [Gunn and Gott 1972; Peebles 1980].

3.2 Evolution of Voids

Voids are characterized by their underdensity relative to the embedding space. As for the spherical mass distributions seen before, the dynamical properties of these growing bubbles can be calculated by approaching them as an evolving, low-density universe sitting in some background universe with generic density Ω. Similar to how overdensities experience Hubble drag and expand at a lower rate compared to the background, underdensities are subject to faster expansions since there is little mass holding them together. The voids are therefore described by the equations for the unbounded spherical shell derived earlier in Eq. 3.12, where now the energy $E > 0$. This corresponds to the red curve in Fig. 3.1. For the closed shells, shell-crossing was assumed to take place only at the very instant of collapse. In the case of open shells, this story is slightly adapted. As will become clear from the equations, it is possible for inner shells to expand at a higher rate than the outer shells, resulting in a relative velocity with which the inner parts of the void can overtake the outer shells. Moreover, this shell-crossing event introduces a natural timescale to consider in the overall evolution of cosmic underdensities.

3.2.a Voids as Unbound Shells

The expansion velocity of a shell of initial radius r_i can be calculated through the time derivative of the scaling factor $\mathcal{R}$ and the chain rule applied on the quantities in Eq. 3.12:

$$v(r,t) = r_i \frac{\mathrm{d}\mathcal{R}}{\mathrm{d}t} = r_i \frac{\mathrm{d}\mathcal{R}}{\mathrm{d}\Phi_r}\cdot\left(\frac{\mathrm{d}t}{\mathrm{d}\Phi_r}\right)^{-1} = r_i \frac{\mathrm{d}\mathcal{R}}{\mathrm{d}\Phi_r}\cdot\left(\frac{1}{H_i}\frac{\mathrm{d}H_i t}{\mathrm{d}\Phi_r}\right)^{-1} \tag{3.27}$$

$$= H_i r_i (\alpha_i - \Delta_{c,i})^{1/2} \frac{\cosh(\Phi_r)}{\sinh(\Phi_r) - 1}. \tag{3.28}$$

From here it is clear that the rate at which the shell expands has a dependence on the critical mean density excess, $\Delta_{c,i}$, which is a measure of how much mass is enveloped by a sphere of radius r_i. For a spherical mass distribution that reaches $\delta = -1$ on a plateau around the center and slightly higher values in the neighbourhood around, it is very well possible for the inner shells to grow at a higher rate than the outermost shells, inevitably leading to shell-crossing.

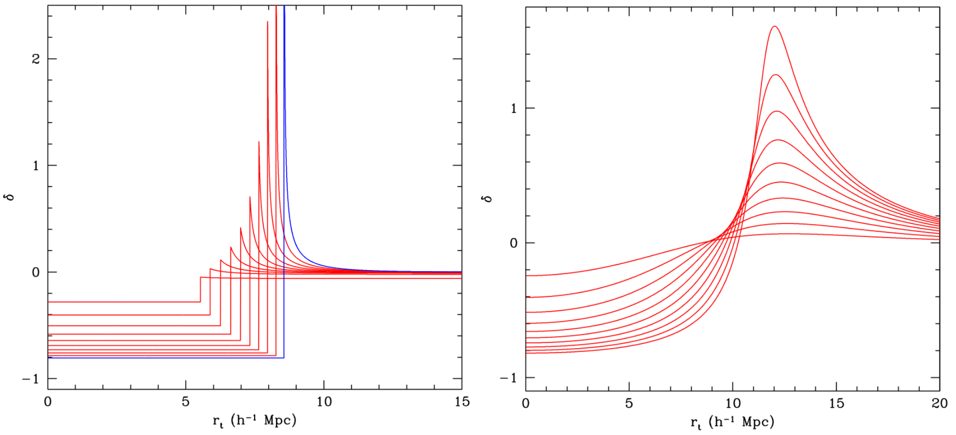

Figure 3.3: Evolution of two spherical voids. The plot on the left shows a void with a bucket or top-hat initial density profile, with $\Delta_i = -10.0$ and initial co-moving radius $r_i = 5.0\,\mathrm{h}^{-1}\mathrm{Mpc}$. The subsequent evolution of the density profile is depicted by the deeper and wider profile, right up to shell-crossing (the last step being the blue curve). Note how around the void an overdense ridge starts to grow, which is constructed from all the matter pushed outside the underdensity. The plot on the right has the same initial parameters but concerns a fallen-over S-shape initial density distribution. Note how the subsequent evolution transforms the distribution towards a top-hat profile. Image courtesy: Rien van de Weygaert.

In the theory of linear perturbation growth, the initial velocity measure α_i for the growing mode can be written as:

$$\alpha_i = -\frac{2}{3} f(\Omega_i)\Delta_i, \tag{3.29}$$

with the function f defined as in Eq. 3.16. This allows for Eq. 3.12 to be rewritten in a slightly simpler form. By Eq. 3.7, one deduces that in the growing mode:

$$\alpha_i - \Delta_{c,i} = -\frac{2}{3} f(\Omega_i)\Delta_i - \Omega_i(1+\Delta_i) + 1 = -A(\Omega_i)\Delta_i + B(\Omega_i) \equiv G(\Omega_i, \epsilon_i), \tag{3.30}$$

where $A(\Omega_i) \equiv \frac{2}{3} f(\Omega_i) + \Omega_i$, $B(\Omega_i) \equiv 1 - \Omega_i$ and $\epsilon_i = -\Delta_i$ to ease the notation. The reasoning behind this transformation becomes clear upon approximating the fraction:

$$\frac{1+\Delta_{c,i}}{\alpha_i - \Delta_{c,i}} \approx \frac{1}{\alpha_i - \Delta_{c,i}} = \frac{1}{-A(\Omega_i)\Delta_i + B(\Omega_i)} = \frac{1}{G(\Omega_i, \epsilon_i)}. \tag{3.31}$$

This allows Eq. 3.12 to be rewritten in the more accessible form:

$$\begin{cases} \mathcal{R}(t_i, r_i, \Phi_r) & = \dfrac{1}{2}\dfrac{1}{G(\Omega_i, \epsilon_i)}(\cosh(\Phi_r) - 1), \\ H_i t & = \dfrac{1}{2}\dfrac{1}{G(\Omega_i, \epsilon_i)^{3/2}}(\sinh(\Phi_r) - \Phi_r). \end{cases} \tag{3.32}$$

Again, to make the point clear, this is but a re-formulation of Eq. 3.12 and bears no new underlying mechanics.

3.2.b A Condition for Shell-Crossing

The physical radius of the shell is related to the initial radius via the scaling parameter $\mathcal{R}$:

$$r(\mathcal{R}, r_i) = \mathcal{R} r_i = \frac{1}{2} r_i \frac{1}{G(\Omega_i, \epsilon_i)}(\cosh(\Phi_r) - 1) = r(t, r_i, G, \Phi_r). \tag{3.33}$$

The main objective is now to find out when and where the first shell-crossing will take place. This problem will be approached by considering two adjacent shells at a small initial radius r_i, and calculate at what time the jump across radii, δr, becomes identically zero. After all, this is exactly what shell-crossing entails in the scenario of cosmic underdensities: an inner shell overtakes an outer shell, hence their radii must be equal at some point in time. Fig. 3.3 shows graphically what happens up until this epoch of shell-crossing. The plot on the left shows a general top-hat function that evolves over time, right until shell-crossing takes place. The evacuation of the center of the void and the formation of an overdense ridge around this void is clearly visible. The plot on the right shows a similar void, but now with a more physical initial density profile: there are no sudden discontinuities. However, as time evolves, it becomes clear that even this mass distribution tends towards the top-hat profile.

The quantity δr can be calculated by using the total derivative:

$$\delta r = \frac{\partial r}{\partial r_i}\delta r_i + \frac{\partial r}{\partial G}\delta G + \frac{\partial r}{\partial \Phi_r}\delta \Phi_r = \left(\frac{\partial r}{\partial r_i} + \frac{\partial r}{\partial G}\frac{\partial G}{\partial r_i} + \frac{\partial r}{\partial \Phi_r}\frac{\partial \Phi_r}{\partial r_i}\right)\delta r_i. \tag{3.34}$$

Though not immediately apparent, each of these terms can be evaluated with the knowledge at hand. The results can be summarized as:

$$\frac{\partial r}{\partial r_i} = \mathcal{R} = \frac{r}{r_i}, \tag{3.35}$$

$$\frac{\partial r}{\partial G}\frac{\partial G}{\partial r_i} = -\frac{r}{r_i}\frac{\partial \ln G}{\partial \ln r_i} \tag{3.36}$$

$$\frac{\partial r}{\partial \Phi_r}\frac{\partial \Phi_r}{\partial r_i} = \frac{3}{2}\frac{r}{r_i}\frac{\sinh(\Phi_r)\left[\sinh(\Phi_r) - \Phi_r\right]}{(\cosh(\Phi_r) - 1)^2}\frac{\partial \ln G}{\partial \ln r_i} \tag{3.37}$$

Putting this all together, Eq. 3.34 can now be written as:

$$\delta r = \frac{r}{r_i}\left(1 - \frac{\partial \ln G}{\partial \ln r_i}\left[1 - \frac{3}{2}\frac{\sinh(\Phi_r)\left[\sinh(\Phi_r) - \Phi_r\right]}{(\cosh(\Phi_r) - 1)^2}\right]\right)\delta r_i \tag{3.38}$$

The final partial derivative can be re-expressed as a derive in ϵ_i instead through use of the chain rule:

$$\frac{\partial \ln G}{\partial \ln r_i} = \frac{r_i}{G}\frac{\partial G}{\partial r_i} = \frac{r_i}{G}\frac{\partial G}{\partial \epsilon_i}\frac{\partial \epsilon_i}{\partial r_i} = \frac{r_i}{G}A(\Omega_i)\frac{\partial \epsilon_i}{\partial r_i} = \frac{A(\Omega_i)\epsilon_i}{A(\Omega_i)\epsilon_i + B(\Omega_i)}\frac{\partial \ln \epsilon_i}{\partial \ln r_i}. \tag{3.39}$$

The only derivative that remains to be found is how the density deficit changes with the radius. In the case of the spherical step function, this relation will be relatively easy to deduce.

3.2.c Top-hat Voids in an Einstein-de Sitter Universe

For a spherical void, the radius relates to the mass and mass deficit according to:

$$M(r_i) = \frac{4}{3}\pi r_i^3 \overline{\rho}_i (1 - \epsilon_i) = \overline{M}(r_i) + \Delta M(r_i), \tag{3.40}$$

where the overbar represents the mean background contribution, and where $\Delta M(r_i)$ essentially quantifies the strength of the underdensity. Outside any localized void, the simplest of which can be imagined as a spherical top-hat void, the mass deficit $\Delta M(r_i)$ would no longer vary, meaning that $\Delta M(r_i) = -\frac{4}{3}\pi r_i^3 \overline{\rho}_i \epsilon_i$ becomes a constant. The missing derivative can then immediately be calculated as:

$$\frac{\partial \ln \epsilon_i}{\partial \ln r_i} = \frac{\partial}{\partial \ln r_i}\left[\ln(r_i^{-3}) + C\right] = -3, \tag{3.41}$$

where C is some constant factor that disappears anyway. In that case, Eq. 3.39 further reduces to:

$$\frac{\partial \ln G}{\partial \ln r_i} = \frac{r_i}{G}\frac{\partial G}{\partial r_i} = -3\frac{A(\Omega_i)\epsilon_i}{A(\Omega_i)\epsilon_i + B(\Omega_i)}. \tag{3.42}$$

This finally allows the condition for shell-crossing to be made explicit by setting Eq. 3.38 equal to zero. In the case of an EdS universe $\Omega_0 = \Omega_i = 1$ and thus $B(\Omega_i) = 1 - \Omega_i = 0$, so the above condition can be expressed in terms of the development angle Φ_r only:

$$1 + 3\frac{A(\Omega_i)\epsilon_i}{A(\Omega_i)\epsilon_i + B(\Omega_i)}\left[1 - \frac{3}{2}\frac{\sinh(\Phi_r)\left[\sinh(\Phi_r) - \Phi_r\right]}{(\cosh(\Phi_r) - 1)^2}\right] = 0 \tag{3.43}$$

$$\implies \frac{\sinh(\Phi_r)\left[\sinh(\Phi_r) - \Phi_r\right]}{(\cosh(\Phi_r) - 1)^2} = \frac{8A(\Omega_i)\epsilon_i + 2B(\Omega_i)}{9A(\Omega_i)\epsilon_i} = \frac{8}{9}. \tag{3.44}$$

This transcendental equation can only be solved numerically. The development angle is determined to be $\Phi_{\text{s-c}} \approx 3.488$ at the time of shell-crossing.

3.2.d Relation to Linearized Gravity

From Eq. 2.10 it is clear that density fluctuations are proportional to the scaling parameter $a \propto t^{2/3}$ in an EdS universe. Since $\delta_i(t) \approx (\delta M/M)(t)$ (Eq. 1.2) and as $\delta_i = \epsilon_i$ for a top-hat distribution, one can deduce based on these three observations that, indeed,

$$\left(\frac{\Delta M}{M}\right)(t) = -\epsilon_i\frac{a(t)}{a(t_i)} = -\epsilon_i\left(\frac{t}{t_i}\right)^{2/3}. \tag{3.45}$$

The second line in Eq. 3.32 can be rewritten using that $H_i = \frac{2}{3t_i}$ in an EdS, resulting in:

$$\frac{t}{t_i} = \frac{3}{4}\frac{1}{G(\Omega_i,\epsilon_i)^{3/2}}(\sinh(\Phi_r) - \Phi_r), \tag{3.46}$$

or in terms of the scaling parameter a as:

$$\frac{a}{a_i} = \left(\frac{2t}{3t_i}\right)^{2/3} = \left(\frac{3}{4}\right)^{2/3}\frac{1}{G(\Omega_i,\epsilon_i)}(\sinh(\Phi_r) - \Phi_r)^{2/3}. \tag{3.47}$$

At the time $t_{\text{s-c}}$ of shell-crossing, $\Phi_{\text{s-c}} \approx 3.488$ according to Eq. 3.44. The mass fluctuation at this time may be approximated as:

$$\left(\frac{\Delta M}{M}\right)(t_{\text{s-c}}) = -\left(\frac{3}{4}\right)^{2/3}\frac{\epsilon_i}{G(\Omega_i,\epsilon_i)}(\sinh(\Phi_{\text{s-c}}) - \Phi_{\text{s-c}})^{2/3} \approx -4.528\frac{\epsilon_i}{G(\Omega_i,\epsilon_i)}. \tag{3.48}$$

which corresponds to the following in terms of the scale parameter:

$$\frac{a_{\text{s-c}}}{a_0} = 4.528\frac{1}{G(\Omega_i,\epsilon_i)}\frac{a_i}{a_0} = \frac{4.528}{A(\Omega_i,\epsilon_i)}\frac{a_i}{a_0}\frac{1}{\epsilon_i} = \frac{4.528}{A(\Omega_i,\epsilon_i)}\frac{1}{\tilde{\epsilon}_i}, \tag{3.49}$$

where $\tilde{\epsilon}_i \equiv a_0\epsilon_i/a_i$ is dubbed the linearly extrapolated initial density deficit. For the EdS universe, where $G = 1$ effectively, this means that:

$$\frac{a_{\text{s-c}}}{a_0} = \frac{4.528}{5/3}\frac{1}{\tilde{\epsilon}_i} = \frac{2.717}{\tilde{\epsilon}_i}, \tag{3.50}$$

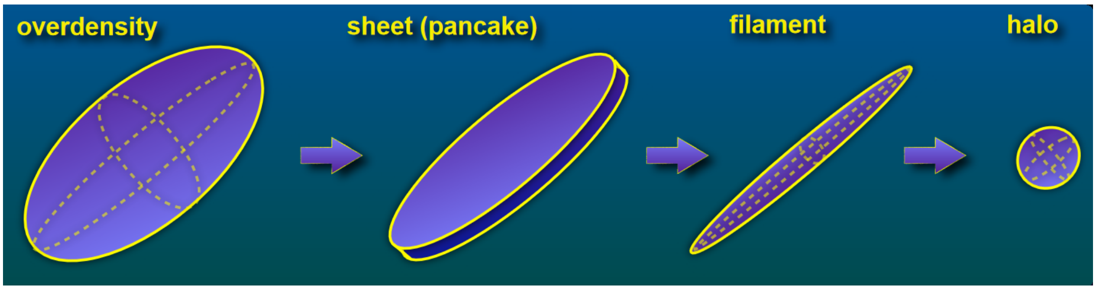

Figure 3.4: Ellipsoidal collapse. Instead of collapsing along all three axes at exactly the same rate, an ellipsoidal mass distribution first collapses into a sheet, then into a filament, and only then to a halo. During every collapse, the dimensionality of the object is decreased by one. Source: Van den Bosch 2022.

or, equivalently, $\delta_{\text{lin}}(t_{\text{s-c}}) \approx -2.717$. This result is analogous to Eq. 3.26 from the theory of Halo collapse and acts as a bridge between the spherical model of void shell-crossing and the linearized theory. Whenever a region in space shows a linearly extrapolated density smaller than -2.717, then this bubble is to be regarded as a cosmic void. This value therefore represents the critical density threshold for void formation.

To make a statement about the size of the underdense sphere at the time of shell-crossing, Eqs. 3.35 and 3.47 can be combined to find that:

$$\frac{r}{r_i} = \frac{1}{2}\left(\frac{3}{4}\right)^{2/3} \frac{\cosh\Phi - 1}{(\sinh\Phi - \Phi)^{2/3}} \left(\frac{t}{t_i}\right)^{2/3}, \tag{3.51}$$

which, at the time of shell-crossing $t_{\text{s-c}}$, evaluates to:

$$\frac{r_{\text{s-c}}}{r_i} = 1.697\left(\frac{t_{sc}}{t_i}\right)^{2/3} = 1.697 \cdot \frac{a_{\text{s-c}}}{a_i}. \tag{3.52}$$

In terms of the scaling parameter $\mathcal{R}$, it follows immediately that

$$\mathcal{R}_{sc} = 1.697\mathcal{R}_i, \tag{3.53}$$

so shell-crossing takes place when the co-moving radius of the void has expanded by a factor of 1.697.

3.3 Validity of Results

The spherical collapse model was introduced in the seminal paper of Gunn & Gott to describe the evolution of infalling matter in clusters. The theory has been extended and improved in many subsequent articles [Fillmore and Goldreich 1984; Bertschinger 1985; Hoffman and Shaham 1985; Avila-Reese, Firmani, and Hernandez 1998; Ryden and Gunn 1987; Subramanian, Cen, and Ostriker 2000; Ascasibar et al. 2004; Hoffman 1986; Zaroubi and Hoffman 1993; Williams, Babul, and Dalcanton 2004; Del Popolo, Pace, and Lima 2013], for instance, to generalize the results of infalling matter to shapes with different symmetries or to make the model more realistic by including effects of shell-crossing, shear velocities or angular moment in generic cosmologies. The background universe of the spherical collapse model can also be generalized to be different than the Einstein-de Sitter universe often assumed in this work. Analytical solutions might not always exist in these generic cases. The collapse barrier for overdensities, accurate to within 1%, can be approximated as [Mo, Van den Bosch, and White 2010]:

$$\delta_{\mathrm{lin},\Omega_m\neq 1}(t_{\mathrm{col}}) = \frac{3}{5}\left(\frac{3\pi}{2}\right)^{2/3} \cdot \left[\Omega_m(t_{\mathrm{col}})\right]^{0.0185} = \delta_{\mathrm{lin},\Omega_m=1} \cdot \left[\Omega_m(t_{\mathrm{col}})\right]^{0.0185}, \tag{3.54}$$

where $\delta_{\mathrm{lin},\Omega_m=1} \approx 1.686$. In a flat universe with a non-zero cosmological constant, there is an extra contribution to the acceleration term due to an effective density term. In this case, one can show that [Mo, Van den Bosch, and White 2010]:

$$\delta_{\mathrm{lin},\Omega_m\neq 1}(t_{\mathrm{col}}) = \frac{3}{5}\left(\frac{3\pi}{2}\right)^{2/3} \cdot \left[\Omega_m(t_{\mathrm{col}})\right]^{0.0055} = \delta_{\mathrm{lin},\Omega_m=1} \cdot \left[\Omega_m(t_{\mathrm{col}})\right]^{0.055}. \tag{3.55}$$

In both scenarios, Eqs. 3.54 and 3.55 show an extremely weak dependence on Ω_m. This suggests that the collapse barrier found in an EdS, Eq. 3.26, can be safely used in more general contexts. The implications of the spherical collapse model, in particular its applications for mass functions predicted in the yet-to-be-treated (Extended) Press Schechter formalism, show reasonable fits to the results of N-body simulations in the high mass range, but deviates substantially in the lower mass regimes [Press and Schechter 1974; Lacey and Cole 1994; Bond et al. 1991; Sheth and Tormen 1999]. The discrepancy is not unsurprising considering the many assumptions made in the spherical model to obtain an analytical solution, and given that density perturbations in the Gaussian field are sometimes thought to be triaxial [Bardeen et al. 1986; Doroshkevich 1970].

These fits are greatly improved upon by not considering the infall of a spherical shell, but rather of an ellipsoidal distribution [White and Silk 1979; Eisenstein and Loeb 1995; Sheth, Mo, and Tormen 2001]. The critical density threshold for structure formation δ_c is independent of the initial size of the overdensity or its final mass in the case of a spherical model, but this no longer holds for the ellipsoidal model. In that case, the barrier starts to depend on the initial overdensity and the shear field surrounding the object. During the ellipsoidal collapse, the axis ratio quickly changes while the ellipsoid transforms into a flat pancake [White and Silk 1979]. As a consequence, small impurities or anisotropies in an otherwise spherical mass distribution could result in a more elongated shape along some axis, after which ellipsoidal collapse is imminent: the spherical symmetry is lost and a runaway axially symmetric infall takes over. Collapsing overdensities that exhibit spherical symmetry can be seen as an inherently unstable equilibrium that quickly loses their azimuthal regularity due to small perturbations. Fig. 3.4 shows the idea behind ellipsoidal collapse graphically.

From the argument that asphericities are magnified during collapse, it might not be surprising that during expansion asphericities are minimized. In other words, underdense voids become more spherically symmetric as time advances [Icke 1984; Van de Weygaert and Van Platen 2009; Ryden and Peterson 2011; Aragon-Calvo and Szalay 2013]. This hypothesis has been tested by numerical N-body simulations and sky surveys and indeed confirms that cosmic voids tend to be more spherical than their overdense counterparts [Centrella and Melott 1983; Foster and Nelson 2009]. Full sphericity is, however, not always apparent. Instead, most voids are found to be slightly prolate [Van Platen, Van de Weygaert, and Jones 2008; Park and Lee 2007; Shandarin et al. 2006]. Underdensities, after all, are never environmentally isolated objects in the way they are treated in the spherical model [Bertschinger 1985; Colberg, Krughoff, and Connolly 2005; Mathis and White 2002]. The internal void dynamics push the system towards a sphere, but external factors, such as the creation of matter filaments at the boundaries between neighbouring voids, lead to asymmetries [Van de Weygaert and Van Platen 2009].

Chapter 4

Hierarchical Halo Population: Excursion Set Description

The key quantities and concepts are now on the table: the primordial density field δ can be modeled as a Gaussian random field, which initially evolves in accordance with linearized gravity and in which halos form when the linearly extrapolated density exceeds δ_c. This chapter will look deeper into how these three observations can be combined to make general statements about hierarchical structure formation. To this end, a powerful statistical framework has been developed and improved upon since its introduction by Press & Schechter, which can be used to deduce number densities and mass distributions for halos [Press and Schechter 1974; Bond et al. 1991]. It is no surprise that this theory has become a cornerstone in the current understanding of the formation of, for instance, galaxies, clusters, and other cosmic structures. This chapter hence fully concentrates on how these models arise from the theory and how they can be applied to the cosmic overdensities. The last chapter will generalize the formalism to make it compatible with the underdensities as well, providing the key to quantities such as the void number density and size distributions.

Within the linearized theory, Eq. 2.7 predicts that the density perturbation field δ scales with the linear growth rate $D(t)$. The cosmology of interest determines $D(t)$ and by knowing the initial profile $\delta(t_i)$ at time t_i, one can deduce what the density field looks like through time when extrapolated using the linear growth rate. The Spherical Model already showed that there exists a relation between the linear and non-linear collapse through the linear collapse barrier δ_c and linear shell-crossing barrier $\delta_{\text{s-c}}$. The same evolution can be seen from two different perspectives: the density field grows proportionally to $D(t)$ in the linear regime until some part of the field passes δ_c or $\delta_{\text{s-c}}$ to form a virialized bound object or evacuated void, respectively. This will be referred to as the *evolving-field* picture. In the second approach, the field is taken to be constant in time, and instead the barriers $\delta_c(t) \equiv \delta_c/D(t)$ and $\delta_{\text{s-c}}(t) \equiv \delta_{\text{s-c}}/D(t)$ are decreasing over time. This *moving-barrier* picture is equivalent to the evolving-field picture but is sometimes easier to work with. Fig. 4.1 shows a cross-section of a 2D GRF, where the points whose linearly extrapolated density exceeds δ_c or falls below δ_v are shaded, signifying collapsed halos and expanding voids respectively.

The Spherical Model assumed that the flat universe was otherwise homogeneous. Nevertheless, it is illuminating to see how the non-linear evolution of the field can be explored by using the initial density field and its linearized extension. To this end, the central assumption in this chapter is that the long wavelength modes of the true, non-linear evolution of the field are well-approximated by the predictions of the linear theory. The main idea is, then, to combine the deterministic Spherical Model with the probabilistic nature of Gaussian random fields, in order to statistically describe the properties of overdense halos and underdense voids. Bardeen et al. 1986 (hereafter BBKS) explored this idea for halos in full analyticity by focusing on the statistical properties of the peaks in a GRF. In this so-called peak formalism, they assumed that the region that collapses to a virialized dark matter halo has a mass that can be associated with those places in the smoothed density field whose density exceeds δ_c. Here, the smoothed density field is given by filtering the initial density field on a scale corresponding to that mass. The halo mass function, the co-moving number density of halos of a given mass, then directly relates to the number density of peaks in the smoothed density fluctuation field as a function of the filtering size. Although the statistics of these peaks could be worked out in full rigor in the case of a GRF, it soon became clear that the central assumption has a serious shortcoming [Bardeen et al. 1986].

Imagine some point massive particle in the fluctuation field, for which the smoothed density field is $\delta_{M_1} > \delta_c$ on a filter scale M_1, but also $\delta_{M_2} > \delta_c$ on the larger filter scale $M_2 > M_1$. The relevant question is whether the test particle belongs to a halo of mass M_1 or M_2. If $\delta_{M_1} > \delta_{M_2}$, nothing peculiar is happening, for this can be imagined as a density peak surrounded by a slightly less dense annulus: the particle will first be part of the halo of mass M_1 and at some later time merges or grows to form the halo of mass M_2, hence it is part of both. However, in the case of the opposite hierarchy $\delta_{M_1} < \delta_{M_2}$, the particle can never be part of a halo of mass M_1 and should instead be immediately incorporated into a halo of mass M_2. This implies that δ_{M_1} ought to be removed from the list of collapsed objects of mass M_1. As has become clear, peaks in the smoothed density field can in fact not always be associated with halos, contrary to the initial assumption. This problem has become known as the cloud-in-cloud problem for halos [Liddle and Lyth 2000; Jedamzik 1995].

This chapter is structured as follows. The first section replaces the peak formalism discussed so far, with the slightly less sophisticated Press-Schechter theory. However, as it turns out, these results can be derived formally using so-called excursion sets, which will be the topic of the second section. Since this chapter focuses on the overdensities, a discussion on their merging behaviour cannot be left out and is hence treated in the last section. It has to be stated that this is merely an introduction to the topic and worked out in full detail for voids in the next chapter.

4.1 Press-Schechter Formalism

The rigorous peak statistics developed in BBKS cannot be easily adapted to this one shortcoming, though numerical models exist that approach this modified version numerically [Bond and Myers 1996]. To deal with this drawback, the mass function can be determined using the less mathematically found Press-Schechter (PS) formalism [Press and Schechter 1974]. This heuris-

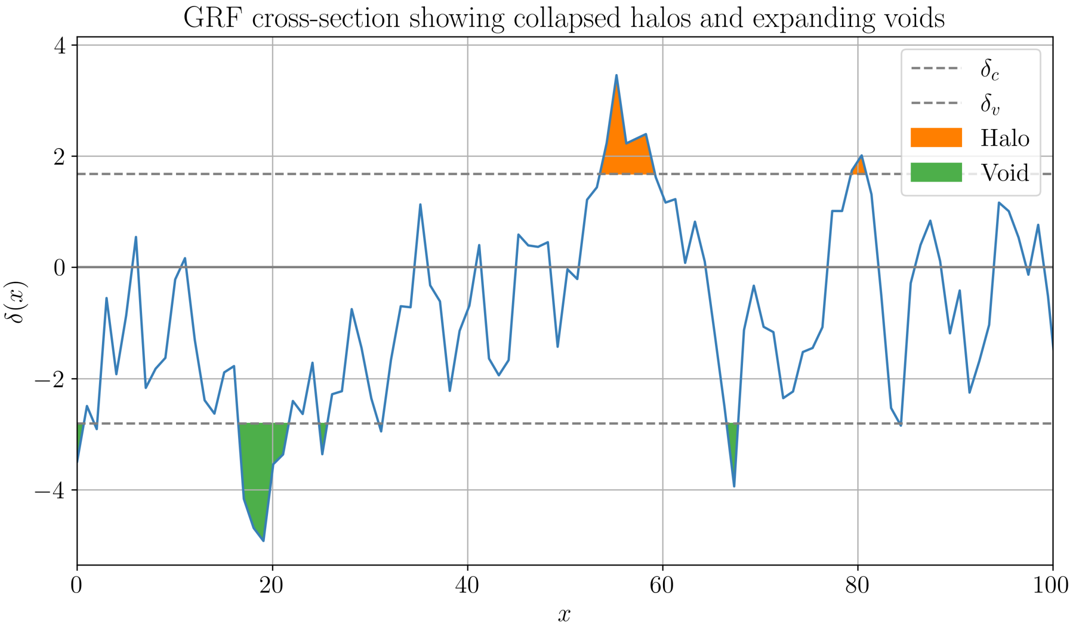

Figure 4.1: A cross-section of a 2D GRF, representing the density fluctuation field δ. The dashed lines represent the two critical barriers: $\delta_c = 1.686$ for halos and $\delta_v = -2.717$ for voids. In the evolving-field picture, the points x with a linearly extrapolated density $\delta(x)$ exceeding δ_c will have collapsed to a virialized halo, while those points that fall below δ_v have undergone shell-crossing and are seen as voids. These regions are shaded in orange and green respectively.

tic approach was later re-derived from a different perspective using excursion sets and is now commonly referred to as the Extended Press-Schechter (EPS) formalism [Bond et al. 1991]. This section focuses on deriving the halo mass function within the PS approach, where voids are completely ignored. In that sense, only the halo collapse barrier δ_c is important, rather than also taking the void barrier δ_v into account.

4.1.a Variances in the Smoothed Field

Recall that the density field δ can be smoothed on a scale R_f by means of the convolution integral with the window function W (Eq. 1.19):

$$\delta(\vec{x}, R_f) = \int \delta(\vec{y})\, W(\vec{x} - \vec{y}, R_f)\, \mathrm{d}\vec{y} \tag{4.1}$$

The variance of the smoothed field generalizes that of the original field, and is thereby written either in terms of R_f or the associated mass M_f:

$$\sigma^2(R_f) = \frac{1}{2\pi^2} \int \mathrm{d}k\; k^2 P(k) \hat{W}^2(kR_f) \equiv \sigma_R^2, \tag{4.2}$$

$$\sigma^2(M_f) = \left\langle \left(\frac{M(\vec{x}, R_f) - \overline{M}(R)}{\overline{M}(R)} \right)^2 \right\rangle \equiv \sigma_M^2. \tag{4.3}$$

R_f and M_f are related through some constant γ_f which is determined by the shape of the window function.[1] In hierarchical structure formation models, such as the CDM universe, the variance σ will be a monotonically decreasing function with increasing smoothing radius R_f [Mo, Van den Bosch, and White 2010]. This is not true for a Hot Dark Matter (HDM) universe, since in that case there is a threshold scale on which structure formation can take place. In the particular case that the power function can be written as a pure power law with spectral index n, Eq. 4.3 can be recast into the more explicit form:

$$\sigma_M^2 \propto M^{-(n+3)/3} = M^{-\alpha}, \tag{4.4}$$

where $\alpha \equiv (n+3)/3$. The exact proportionality constant can be deduced from the well-known cosmic parameter σ_8:

$$\sigma_8^2 \equiv \sigma^2(R_f = 8\,\text{Mpc}) = \frac{1}{2\pi^2} \int \mathrm{d}k\; k^{n+2}\; \hat{W}_{\text{TH}}^2(kR_f), \tag{4.5}$$

where $\hat{W}_{\text{TH}}$ is the top-hat filter function as defined in Eq. 1.18. The parameter σ_8 is hence defined as the field fluctuation when using a spherical unit step function filter of radius 8 Mpc, which then in turn specifies Eq. 4.4. Recent observations by Planck show that $\sigma_8 \approx 0.811 \pm 0.006$ [Planck Collaboration 2020b]. $\delta(\vec{x})$ has been assumed to be a Gaussian field and the act of smoothing the field on some scale R_f does not destroy this Gaussianity [Mo, Van den Bosch, and White 2010]. Hence, in terms of masses, the probability of finding a linear density deviation of size δ_M is simply given by the normalized Gaussian:

$$\mathbb{P}(\delta_M) = \frac{1}{\sqrt{2\pi}\,\sigma_M} \exp\left\{-\frac{\delta_M^2}{2\sigma_M^2}\right\}. \tag{4.6}$$

The goal is now to assign masses to the peaks in the density distribution. The first step is to find a peak within the field that satisfies $\delta > \delta_c$. Then, some smoothing function W is introduced with a small filtering radius R_f and with its center on the peak. By increasing R_f, the smoothed linear density excess will eventually start to decrease, as in the limit where $R_f \to \infty, \delta \to 0$ per the definition of the fluctuation field. At some point, the size of the filtering function is such that $\delta = \delta_c$, and this is exactly the size R_f that will be assigned to the overdensity.

4.1.b The Halo Mass Function

Press and Schechter postulated that for the density δ_m smoothed on the scale M that:

> The fraction of matter that satisfies $\delta_M > \delta_c(t)$ is the same as the mass fraction that at time t is contained in halos with mass greater than M.

With the mathematics developed so far, this translates into the preliminary definition:

$$\widetilde{\mathbb{F}}(>M,t) \;=\; \mathbb{P}(\delta_M > \delta_c) = \frac{1}{\sqrt{2\pi}\,\sigma_M} \int_{\delta_c}^{\infty} \mathrm{d}\delta_M\; \exp\left\{-\frac{\delta_M^2}{2\sigma_M^2}\right\} = \frac{1}{2}\mathrm{erfc}\left(\frac{\delta_c}{\sqrt{2}\sigma_M}\right). \tag{4.7}$$

Here, $\widetilde{\mathbb{F}}(>M,t)$ is a function that represents the fraction of matter on a mass scale larger than M that exceeds the critical density δ_c. In the limiting case where $M \to 0$, Eq. 4.7 predicts that 50%

---

[1] For the often applicable top-hat filter $\gamma_f = 4\pi/3$ and the Gaussian filter uses $\gamma_f = (2\pi)^{3/2}$. The sharp k-space function has $\gamma_f = 4\pi^2$.

of all matter is contained in collapsed halos. This might seem sensible at first when realizing that $\mathbb{P}(\delta < 0) = \frac{1}{2}$, so only the initially overdense regions collapse. Underdense parts of the universe, however, might be enclosed within larger overdense regions, which would allow them to have a non-vanishing probability of being incorporated into a larger collapsing object. So, even underdense regions can be labeled as being part of some collapsed structure. This problem was adverted by introducing the infamous fudge factor of 2:

$$\mathbb{F}(> M, t) \equiv 2\widetilde{\mathbb{F}}(> M, t) = \operatorname{erfc}\left(\frac{\delta_c}{\sqrt{2}\sigma_M}\right). \tag{4.8}$$

Note that this particular problem bears a resemblance to the cloud-in-cloud problem. The solution was only heuristic: Press & Schechter argued that all initially underdense regions would be incorporated in collapsed structures at some point in time, hence only the frequencies would have to be doubled in $\widetilde{\mathbb{F}}(> M, t)$ to get the true functional form $\mathbb{F}(> M, t)$. The number of haloes with masses between M and $M + \mathrm{d}M$ at time t per co-moving volume will be denoted by $n(M, t)\,\mathrm{d}M$ [Van de Weygaert 2004c]:

$$n(M, t)\,\mathrm{d}M = \frac{\mathrm{d}n}{\mathrm{d}M} = \frac{1}{M}\frac{\mathrm{d}n}{\mathrm{d}\ln M}. \tag{4.9}$$

At the same time, $\frac{\partial F}{\partial M}\,\mathrm{d}M$ gives the fraction of mass in the range $[M, M + \mathrm{d}M]$ exceeding the critical density. Multiplying this by $\overline{\rho}$ gives the mass per unit volume stored in the haloes, and subsequent division by M then gives a number density of these objects with masses between M and $M + \mathrm{d}M$:

$$n(M, t)\,\mathrm{d}M = \frac{\overline{\rho}}{M}\frac{\partial \mathbb{F}}{\partial M}\mathrm{d}M = \frac{\overline{\rho}}{M^2}\sqrt{\frac{2}{\pi}}\frac{\delta_c}{\sigma_M}\exp\left\{-\frac{\delta_c^2}{2\sigma_M^2}\right\}\left|\frac{\mathrm{d}\ln\sigma_M}{\mathrm{d}\ln M}\right|\mathrm{d}M. \tag{4.10}$$

This is the so-called Press-Schechter mass function which gives the co-moving number density of objects in the mass range M and $M + \mathrm{d}M$. By the simple change of variables $\nu := \delta_c(t)/\sigma_M$, Eq. 4.10 can be rewritten as:

$$n(M, t)\ \mathrm{d}M = \frac{\overline{\rho}}{M^2}\sqrt{\frac{2}{\pi}}\nu\exp\left\{-\frac{\nu^2}{2}\right\}\left|\frac{\mathrm{d}\ln\sigma_M}{\mathrm{d}\ln M}\right|\mathrm{d}M. \tag{4.11}$$

The leftover derivative depends on the functional form of the power function. As done before, the focus will lie on the implications of a pure power law, for which Eq. 4.4 already stated:

$$\sigma(M)^2 = AM^{-(n+3)/3} = AM^{-\alpha}, \tag{4.12}$$

where A is now the explicit proportionality factor. This relation allows one to express masses in terms of a characteristic mass M_*:

$$\frac{\nu}{\sqrt{2}} = \frac{\delta_c}{\sqrt{2}\sigma(M)} = \frac{\delta_c}{\sqrt{2A}}M^{(n+3)/6} = \left(\frac{M}{M^*}\right)^{(n+3)/6} = \left(\frac{M}{M^*}\right)^{\alpha/2}, \tag{4.13}$$

where the mass M^* is now defined as [Van de Weygaert 2004c]:

$$M^* \equiv \left(\frac{\sqrt{2A}}{\delta_c}\right)^{6/(n+3)} = \left(\frac{2A}{\delta_c^2}\right)^{3/(n+3)} = \left(\frac{2A}{\delta_c^2}\right)^{1/\alpha}. \tag{4.14}$$

Thereby, the mass function predicted by the Press-Schechter formalism (Eq. 4.10) for a pure

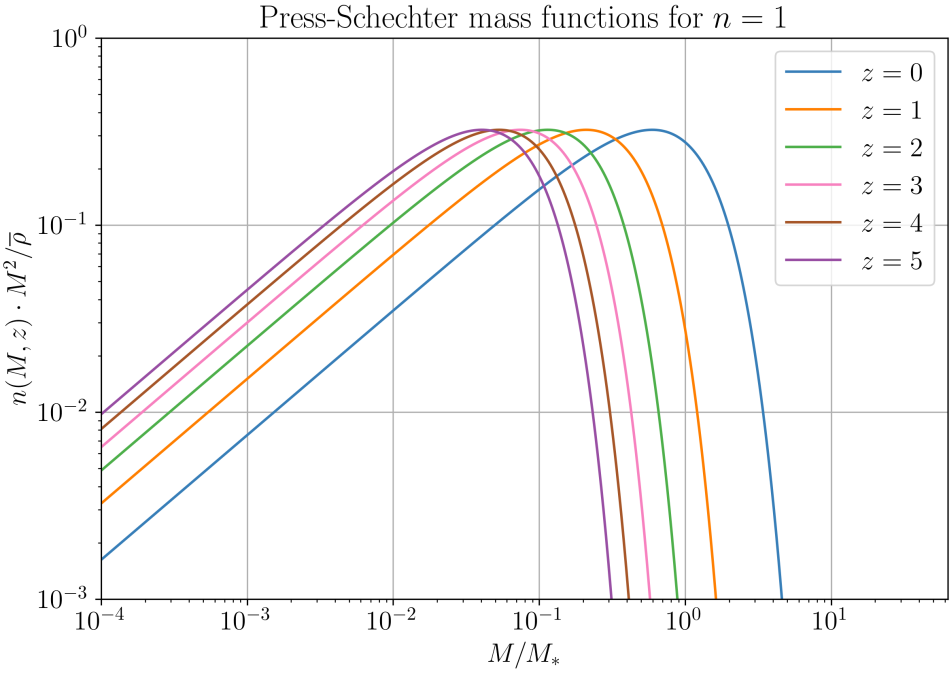

Figure 4.2: The Press-Schechter mass function $n(M,t)$ as derived in Eq. 4.15, multiplied by $M^2/\overline{\rho}$. For the spectral index in the power law, a value of $n = 1$ was chosen. The time-dependence enters via Eq. 4.14 into the characteristic mass, and is plotted as five different values for the redshift z.

power law spectrum $P(k)$ expressed in terms of M^* is given by:

$$n(M,t)\,\mathrm{d}M = \frac{\overline{\rho}}{M^2}\frac{1+n/3}{\sqrt{\pi}}\left(\frac{M}{M^*}\right)^{(n+3)/6} \exp\left\{-\left(\frac{M}{M^*}\right)^{(n+3)/3}\right\}\mathrm{d}M. \tag{4.15}$$

This equation is plotted for a range of redshift values in Fig. 4.2 in an $n = 1$ universe. Note the physical implications of this result. First of all, it is clear that the exponential term signifies an exponential decay for large mass halos: the number density of collapsed structures hence approaches zero as $M \to \infty$. Secondly, in the moving-barrier picture, $\delta_c(t)$ is a strictly decreasing function of time. Hence, as the universe evolves, the characteristic mass in Eq. 4.14 starts to increase, such that extremely heavy halos can start to appear. From the physical point of view, this can be understood from later halos having had enough time to merge with other overdensities to form larger objects as time progresses. The PS mass function has for instance been used to calculate the number densities of galaxies [Cole and Kaiser 1989; White and Frenk 1991; Kauffmann, White, and Guiderdoni 1993], clusters of galaxies [Zhan 1990; Bartlett and Silk 1993] and Lyman-α clouds [Kauffmann and Charlot 1994; Mo and Miralda-Escude 1994]. Moreover, it has also led to the development of models of halo substructures and mergers [Rodrigues and Thomas 1996; Bower 1991; Lacey and Cole 1993; Lacey and Cole 1994].

4.2 Extended Press-Schechter Formalism

The mathematical rigor that the original Press-Schechter formalism lacked, in particular the magical fudge factor 2, was later provided by what is now referred to as the Extended Press-

Schechter theory or the Excursion Set Formalism [Bond et al. 1991]. The seminal paper by Bond, Cole, Efstathiou, and Kaiser (BCEK) showed how the same results of regular PS theory could be obtained from a different point of view by considering so-called excursion sets. The quantity σ_M^2 takes a central role in this approach and is therefore often denoted by S for shorthand notation. As noted before, in a hierarchical model for cosmic structure formation, S is in a one-to-one relation with the filter mass M or, equivalently, the filter size R: for a given S, one can always find the corresponding R or M, or vice versa.

Excursion sets will be of particular importance in the last chapter of this work when they are applied in the context of the evolution of voids. For now, this section focuses on deriving and understanding the EPS theory first for the simpler overdense halos. As for the PS formalism described before, this will be significantly easier than the full story, because now only the critical barrier for halos δ_c has to be taken care of. In the last chapter, besides the cloud-in-cloud problem, there will be three additional problems that are best handled by using excursion sets.

4.2.a Excursion Sets

In the excursion set method, the behaviour of the density field δ_S smoothed on a scale R (and thereby S) is analyzed for each point in the field for a range of radii. By plotting them as a graph of points (S, δ_S), the neighbourhood around this point is, so to say, being scanned for over- and underdense regions. δ_S drops to zero when the filter mass approaches infinity since the whole universe would then be smoothed to the average density $\overline{\rho}$, such that the fluctuation has to drop to zero. So, the starting point of such a graph has to be the point $(0, 0)$. After that, decreasing M will lead δ_S to take on non-zero values if embedded in a universe with non-zero density fluctuations. Of course, the precise path taken subsequently depends on the surroundings of the point of interest. If two points close together are compared to one another, one would see that at the largest M scales, the paths taken would be almost identical. However, when the filter size decreases to the order of magnitude of the distance between the two points, the corresponding paths will also naturally start to differ. Within the EPS formalism, of particular interest is the filter scale R where the path crosses the δ_c border for the first time. This is dubbed the first up-crossing and signifies the mass M of the halo in which the point will eventually be included. Fig. 4.3 shows an example of such a trajectory, taken from a 2D GRF with spectral index $n = -2.5$. The smoothing of the random field was done using a top-hat filter of varying radius, so the resulting trajectory is strictly speaking not a true Markovian random walk. Nevertheless, the path $\delta(S)$ can be seen to correspond to the cloud-in-cloud problem, where an overdense region is surrounded by matter that also ultimately collapses to a bound structure.

In the EPS formalism, the window function is chosen to be the sharp k-space filter, defined in Eq. 1.28, rather than the simpler real space top-hat function or the Gaussian smoothing filter. For the sharp k-space filter of size R (and corresponding mass M and variance S), the smoothed density profile is given by:

$$\delta_S(\vec{x}) = \int \mathrm{d}\vec{k}\ \delta(\vec{k})\ \hat{W}(\vec{k}R) e^{i\vec{k}\cdot\vec{x}} = \int_{k<k_c} \mathrm{d}\vec{k}\ \delta(\vec{k}) e^{i\vec{k}\cdot\vec{x}}, \tag{4.16}$$

with $k_c = 1/R$. Now, whenever S is increased, we know by the one-to-one correspondence that M decreases. Thereby, R decreases and k_c increases: when slightly increasing S, $\delta_S(\vec{x})$ takes on the same value as before plus the contribution of the shell by which the k-sphere increases. For a Gaussian random field, this means we are adding independent modes to the new value of δ_S, which bare no resemblance to any previous values. This would not be true for other smoothing functions, thereby marking a major advantage of the sharp k-space filter [Mo, Van den Bosch,

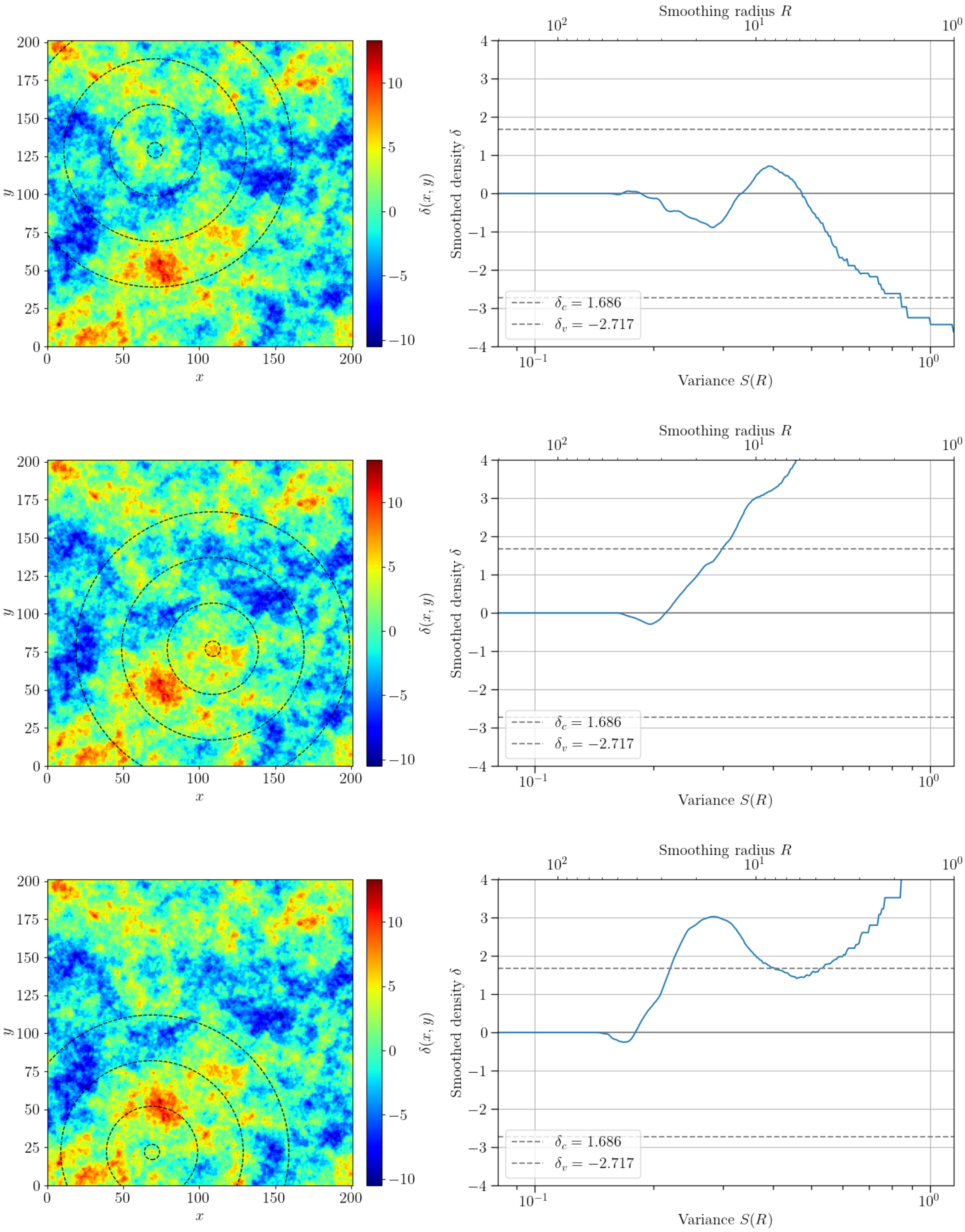

Figure 4.3: Three examples of a smoothed density trajectory as calculated in a 2D GRF with spectral index $n = -2.5$ and a top-hat filtering function. The plots in the left column show the GRF and the point at which the trajectory was taken. The surrounding circles indicate the increasing size of the top-hat function. The plots on the right show the corresponding trajectories $\delta(S)$. The mass element in the bottom row turns out to be a cloud-in-cloud: the overdensity is surrounded by another overdense region.

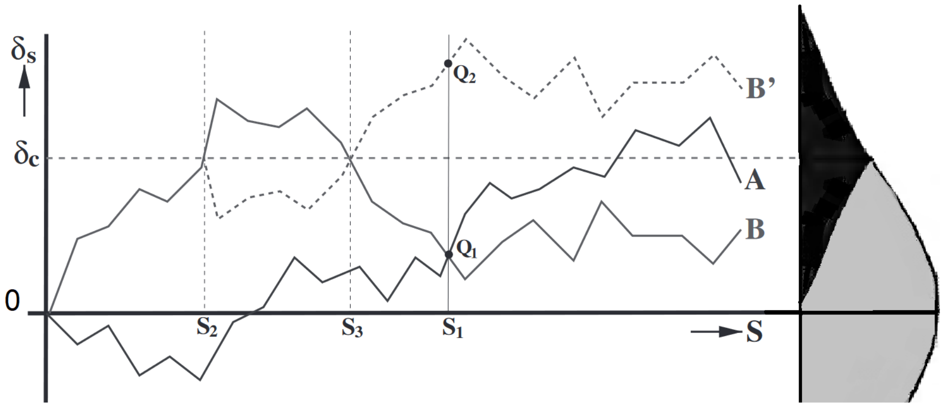

Figure 4.4: An example of three random walks, obtained by calculating δ_S for a range of S values for three hypothetical points in the density field. Path B' is obtained by mirroring path B for all $S > S_1$ in the dashed line. This line represents the collapse barrier for halos and would be moving downward over time in the moving-barrier picture. The shaded region in the Gaussian on the right above the barrier δ_c represents the fraction of trajectories above the barrier at S. Since trajectories B and B' are equally likely, an area of exactly the same size should be shaded underneath the barrier, reflecting the fraction of trajectories that end up below the barrier, but surpassed it at some point. Adapted from Mo, Van den Bosch, and White 2010; Bond et al. 1991.

and White 2010]. In essence, the new modes being independent with randomly distributed phases implies that the paths (S, δ_S) are Markovian random walks, for which the mathematics involved can be worked out analytically.

Fig. 4.4 shows an example of three such random walks, where path B' is obtained by reflecting path B in the dashed line, which represents the collapse barrier δ_c. If these hypothetical paths were obtained by smoothing the GRF with a sharp k-space filter, then each of these trajectories would be a Markovian random walk. In particular, this means that paths B and B' are equally likely to occur. The same figure also shows the shortcomings of the assumption made in the original PS. This ansatz stated that the fraction of lines that lie above δ_c at S_1 should be equal to the fraction of matter that ends up in halos with a mass exceeding the mass M_1 that corresponds to S_1. Surely, this would not be the case for the mass element of trajectory B since it has a density $Q_1 < \delta_c$ for the smoothing size S_1. Its density, however, does rise above the critical collapse barrier between S_2 and S_3, and so the mass element would end up in a collapsed structure of mass $M > M_3 > M_1$. But this immediately contradicts the previous statement, hence one must conclude that the PS ansatz is in hindsight not self-consistent. Trajectories like path B are not properly taken care of in the original formalism and is thereby not accounted for when calculating number densities, but the solution to this apparent problem is surprisingly simple. Path B' is consistently described by the PS ansatz, and because of the use of the sharp k-space filter, it is equally likely to appear as path B. Since it holds true that any failing path has one, and only one, succeeding mirror version, the number density can simply be doubled to take care of any missed trajectories. This explains precisely the origin of the fudge factor 2 in the original PS formalism.

4.2.b The Diffusion Equation

The PS ansatz is now replaced by the EPS ansatz:

> The fraction of trajectories that have their first up-crossing through the critical collapse barrier $\delta_S > \delta_c(t)$ at a scale $S > S_1$ is equivalent to the mass fraction that is incorporated in halos of mass $M < M_1$ at that time t.

If $M \to 0$ as $S \to \infty$, as is the case for the hierarchical structure formation models, essentially each path will at some large S have a positive density fluctuation, such that over time all matter elements will have to be part of some collapsed structure. Now as noted before for pure Brownian random walks, when S increases by ΔS then δ changes by an amount $\mathrm{d}\delta$, where this increment is completely determined by the contribution of new Fourier modes in the infinitesimal shell in k-space. The trajectories $\delta(S)$ will thereby satisfy the diffusion equation [Mo, Van den Bosch, and White 2010]:

$$\frac{\partial Q}{\partial S} = \frac{1}{2}\frac{\partial^2 Q}{\partial \delta^2}, \tag{4.17}$$

where $Q(\delta, S)$ denotes the number density of trajectories at S within the range $[\delta, \delta + \mathrm{d}\delta]$.[2] Boundary conditions should be imposed on the differential equation in order to get sensible results. The trajectories $\delta(S)$ have to pass through the point $(\delta_S, S) = (0, 0)$ and reach (δ_S, S) without have crossed an $S' < S$ for which $\delta(S') > \delta_c$. The second condition is equivalent to putting an absorbing barrier right at δ_c.

Including the boundary conditions, Eq. 4.17 can be solved analytically [Chandrasekhar 1943]:

$$Q(\delta_S, S, \delta_c(t)) = \frac{1}{\sqrt{2\pi S}}\left(\exp\left\{-\frac{\delta_S^2}{2S}\right\} - \exp\left\{-\frac{(\delta_S - 2\delta_c)^2}{2S}\right\}\right) \tag{4.18}$$

The fraction of trajectories $F(> S)$ that have their first up-crossing at an $S' > S$ is then given by the integral:

$$F(> S) = \int_{-\infty}^{\delta_c} Q(\delta_{S'}, S', \delta_c(t))\,\mathrm{d}S'. \tag{4.19}$$

Finally, the first-crossing distribution is calculated explicitly as:

$$f(S, \delta_c)\,\mathrm{d}S = \frac{\partial F(> S)}{\partial S}\,\mathrm{d}S = \frac{1}{\sqrt{2\pi}}\frac{\delta_c}{S^{3/2}}\exp\left\{-\frac{\delta_c^2}{2S}\right\}\mathrm{d}S, \tag{4.20}$$

and substituting in the first equality of Eq. 4.10, one obtains:

$$n(M, t)\,\mathrm{d}M = \frac{\overline{\rho}}{M}\frac{\partial \mathbb{F}}{\partial M}\mathrm{d}M = \frac{\overline{\rho}}{M} f(S, \delta_c)\left|\frac{\mathrm{d}S}{\mathrm{d}M}\right|\mathrm{d}M \tag{4.21}$$

$$= \frac{\overline{\rho}}{M^2}\sqrt{\frac{2}{\pi}}\frac{\delta_c}{\sqrt{S}}\exp\left\{-\frac{\delta_c^2}{2S^2}\right\}\left|\frac{\mathrm{d}\ln\sqrt{S}}{\mathrm{d}\ln M}\right|\mathrm{d}M. \tag{4.22}$$

The mass function as predicted by the excursion set formalism exactly matches that of the PS approach in Eq. 4.10. In this case, there was no need to include any ad hoc fudge factors to make the solution consistent. The excursion set formalism hence provides the mathematical backbone that the original Press-Schechter perspective sometimes slightly lacked.

---

[2] BCEK showed that this partial differential equation is only slightly adapted in the case of smoothing functions other than the sharp k-space filter applied here. The generalized version includes two new parameters: the drift and variance parameters [Bond et al. 1991].

4.2.c Excursion Sets in Other Applications

The excursion set theory forms the mathematical backbone of the Extended Press-Schechter formalism, though there exist many more applications within the field of cosmology. For instance, it has been used to predict characteristic bubble sizes of HII regions during the epoch of reionization and their statistical distribution [Furlanetto, Zaldarriaga, and Hernquist 2004; Lin et al. 2016; McQuinn et al. 2007]. The size distributions in the reionization bubble network is essential in determining the progress and duration of the reionization epoch, and for instance also affects the CMB anisotropies [McQuinn et al. 2005; Zahn et al. 2005; Iliev et al. 2006a; Iliev et al. 2006b]. The correspondence between the analytical model, which once again assumes the bubbles being perfectly spherical, and radiative transfer simulations of reionization are remarkable [Zahn et al. 2007; Mesinger and Furlanetto 2007; Zahn et al. 2011].

The next chapter focuses on applying set excursion theory to the objects that have been left untouched till now: the cosmic voids. As will soon become clear, to properly describe the underdense pockets, the second barrier δ_v should somehow be included in the story. This imposes extra conditions on the smoothed density trajectories, since now two barriers have to be accounted for instead of one [Sheth and Van de Weygaert 2004]. The details are left to the next chapter. As it turns out, both the overdense halos as well as the underdense voids can be described in terms of excursion set theory. It might not come as a surprise that this formalism can then also be used to analytically compute the evolution of other components in the cosmic web: sheets and filaments [Shen et al. 2006]. In a sense, these two can be interpreted as the higher-dimensional siblings of halos: sheets refer to objects that collapsed along one axis, filaments to those that collapsed along two, and halos to those objects which completed their triaxial collapse [Sheth, Mo, and Tormen 2001]. Applying set excursion theory on this configuration allows one to compute the mass fraction of the universe contained in each of these three objects. In hierarchical structure formation models, sheets are composed of filaments, which in turn are made up of halos, while every halo at a some time used to be a filament of the same mass, and much before that, a sheet [Shen et al. 2006].

4.3 Halo Merging: Lacey & Cole Formalism

The (Extended) Press-Schechter theory has proved useful in predicting the number densities of dark matter halos for a given mass and time. This later lead to the halo merger formalism introduced by [Lacey and Cole 1993], which provides access to, for instance, the probability mass distribution for the progenitors of a halo of a given mass. In their binary model, the EPS formalism can then be used to deduce the merger and absorption rates of the overdensities, in which the former refers to the fusion of two halos of similar size, and where the latter refers to the continuous accumulation of matter on the existing halo. This rate naturally not only depends on the masses of the two halos involved, but also on the properties of the cosmology through the spectral index n and the density Ω_0 Much effort is put in N-body codes to simulate the gravitational interactions on some initial mass configuration, including advanced feedback mechanisms such as energy injections due to star formation, which could then be used to numerically determine these rates. Although these models might result in accurate results, having access to analytical models to calculate halo merger rates is essential to shed light on the delicate physics involved. The next chapter will derive the mathematical expressions discussed so far in the context of voids and compares these to what the halo theory of Lacey & Cole predicts.

Merger trees play a crucial role in the Lacey & Cole formalism, offering a comprehensive un-

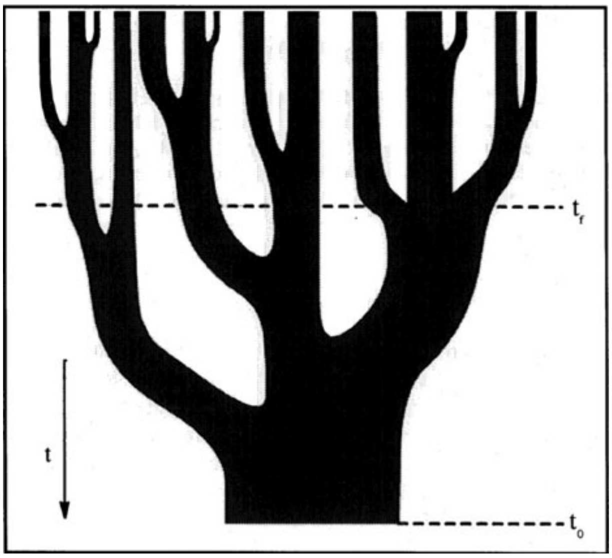

Figure 4.5: Merger Tree. This figure schematically shows how separated clumps of mass (parent halos) at earlier times (top of the diagram) merge under the effect of gravity into ever larger structures. When two branches collide, a merging event takes place. The horizontal line t_0 indicates the present time with a single halo of mass M. The time t_f represents the first time time that a parent halo has a mass $M' > M/2$. Note that this binary model assumes that merging events always take place with two bodies involved. Source: [Lacey and Cole 1993].

derstanding of the hierarchical structure formation and merging history of dark matter halos. These trees provide a powerful tool for tracking the evolution of structures and investigating the growth of overdensities as time progresses. In this formalism, a merger tree represents the merging history of dark matter halos and graphically illustrates how smaller halos combine to form larger overdensities, as depicted in Fig. 4.5. At the root of the merger tree, which corresponds very contradictory to the top of the diagram, lies the initial conditions of the universe in terms of the primordial density fluctuations. As the universe evolves over time, these fluctuations start to grow and merge under the influence of gravity. Each branch of the merger tree represents a merger event, where two halos combine to form a more massive halo. The branches connect halos of possibly vastly different sizes at different cosmic epochs, which reflects the assembly history of cosmic structures, all while conserving the total mass. The LC formalism utilizes the statistical properties of these density fluctuations to determine the merger rates and construct the merger tree. It is important to remember that this is built upon the assumption that merging is a binary event, in which two halos collide to form one larger object. Many algorithms have been developed with the specific purpose of calculating the merger tree [Kauffmann, White, and Guiderdoni 1993; Sheth and Lemson 1999; Somerville and Kolatt 1999; Cole et al. 2000; Neistein and Dekel 2008].

Chapter 5

Hierarchical Evolution of the Void Population

The Press-Schechter theory discussed so far, and for that matter also the excursion set formalism, only concerns the structure formation of overdense halos. In the context of the Extended Press-Schechter formalism, combining the notion of excursion sets and the critical density collapse barrier δ_c leads to the diffusion equation in Eq. 4.17. After imposing the relevant boundary conditions, the solution to this partial differential equation can be directly related to the halo mass function. This approach is nowadays preferred over the original work of Press & Schechter. The main difficulty in their theory arose in the context of double counting the halos enclosed in larger overdense structures. This cloud-in-cloud problem could be averted in the extended formalism by introducing the absorbing barrier condition while solving the differential equation.

Counting voids is inherently more complex than counting halos. A first guess might be to simply replace the critical density for collapse δ_c by the critical density for expanding voids δ_v in the EPS formalism. However, as it turns out, voids are to be treated with more delicacy. As will soon become clear, even though the GRF treats over- and underdensities on an equal footing, voids should not be regarded as the negative mirror image of their overdense counterparts. Interactions between voids and halos destroy the apparent symmetry between the two. This makes the same problem immediately a lot more challenging, for now two barriers have to be taken into account: the single-barrier excursion set formalism ought to be extended to intrinsically more complex double-barrier theory. Physically speaking, dealing with both the halo and void barrier leads to four typical mass configurations that could be found in the density field [Sheth and Van de Weygaert 2004] (also see Figs. 5.1 and 5.2):

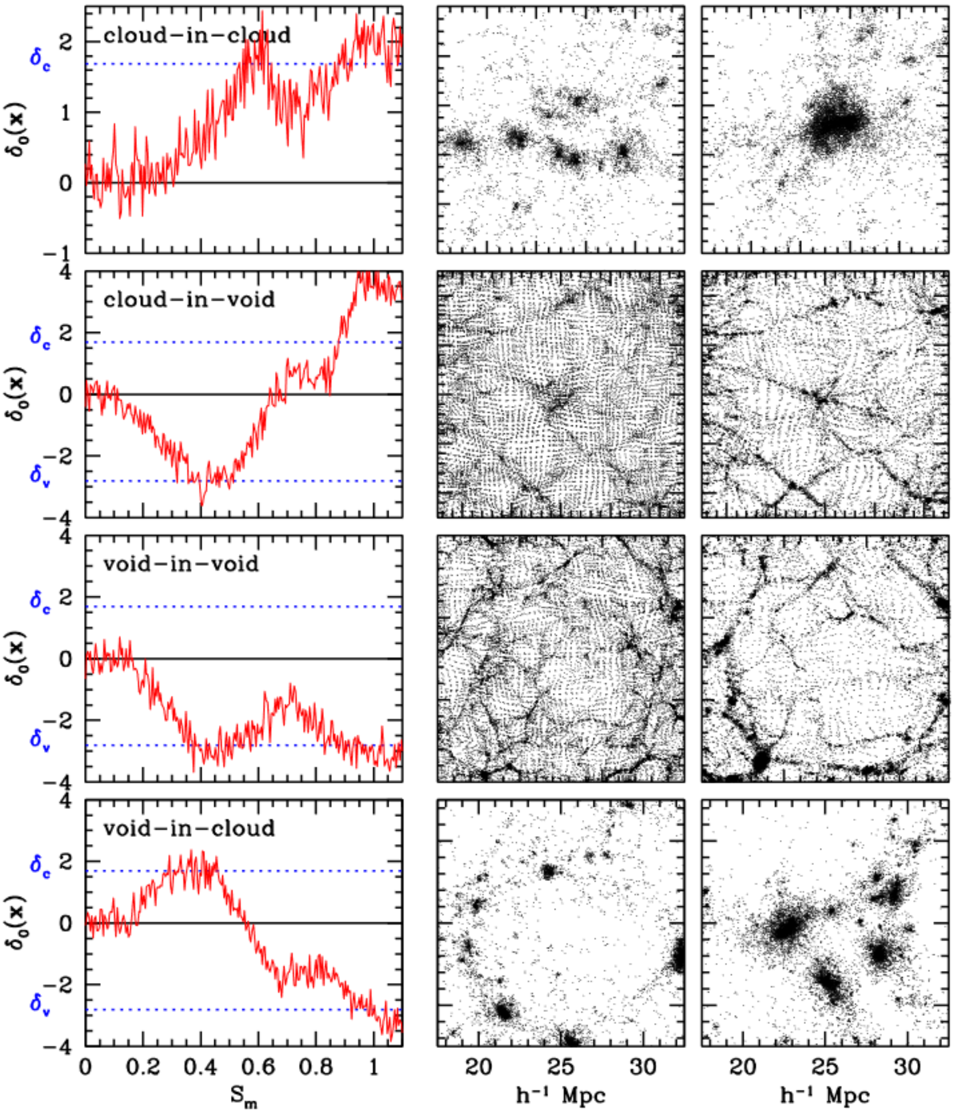

Figure 5.1: The four modes in the extended excursion set formalism for voids. Each row shows one of the characteristic mass configurations when including both halos and voids in the model. The first column shows the smoothed density trajectories $\delta(S)$, where the dashes lines indicate the halo and void barriers, while the second and third column graphically show the evolution of such a mass distribution as predicted by an N-body simulation. Source: [Sheth and Van de Weygaert 2004].

Cloud-in-Cloud: This mode is inherited from the halo theory and refers to collapsing clumps embedded in larger overdense regions. These smaller subhalos should no longer be taken into account when counting halos, since they are already part of a greater structure. Only the largest cloud should therefore be counted.

Cloud-in-Void: Collapsed structures can also be embedded in an expanding void. The halos are not easily torn apart by the expansion of the surrounding void, making this mode relatively unimportant for halo formation [Sheth and Van de Weygaert 2004].

Void-in-Cloud: Although the naming suggests that this could perhaps be regarded as the complement of the previous mode, the void-in-cloud configuration is inherently different from the cloud-in-void. As time progresses, the subvoid naturally tries to expand while the surrounding overdensity compresses to form a virialized halo. The void will not survive this process. This is often phrased as the void being squeezed out of existence by the collapse of the surrounding overdensity [Sheth and Van de Weygaert 2004]. It is this particular process that leads to a symmetry breaking that requires halos and voids to be treated differently.

Void-in-Void: The final configuration is analogous to the cloud-in-cloud problem. It describes a situation in which underdense subvoids are embedded in bigger, still underdense, structures. The largest void is selected when counting voids and the smaller subvoids should be disregarded.

Together, these four modes show two important physical interactions. On the one hand, as was the case in overdense halos, voids may combine with other voids in merger events. An illustrative example is shown in the first row in Fig. 5.6. Using an N-body simulation, each panel shows the time evolution of some initial density configuration, where over time a web-like structure appears. Of particular interest in this context is the appearance of small voids in the center panel. As time progresses, these subvoids merge together into ever larger voids until one large underdense structure remains in the last panels, surrounded by filaments and similarly grown underdensities. On the other hand, besides growing through combining, voids can also cease to exist. This process is encapsulated in the void-in-cloud mode and has no direct analog in halo theory. The bottom row in Fig. 5.6 shows this process in practice for three different voids. In each panel, the void depicted in the center is surrounded by matter moving towards the underdensity, as is denoted by the arrows representing velocity vectors. None of these three voids can escape their fate: sooner or later, matter penetrates the underdensity after which the void size inevitably drops, until at some point they are simply eradicated.

This chapter is structured as follows. The excursion set formalism introduced in the last chapter is made compatible with voids by including the second barrier, in what has become known as the Sheth & Van de Weygaert Model. The second section combines the results of the first section with the mathematical techniques of Lacey & Cole, introduced in the previous chapter. In time, this leads to conditional void size distributions, void merger rates, and void absorption rates. These are key quantities that help in understanding the evolutionary properties and dynamics of voids.

5.1 Void Excursion Sets

To count the number of voids, one is interested in those trajectories that reach the critical density value for voids δ_v at some scale S, without having crossed the critical density value for halos δ_c at some earlier pseudotime $S' < S$. The trajectories for which this last statement is not true are those that are underdense regions on the small scales and overdense regions on the larger scales. These are precisely the void-in-clouds that should be omitted when counting voids, for they are known to cease to exist when the trajectory surpasses δ_c and the surrounding cloud collapses. As calculated in the spherical model for voids, a natural choice for the void barrier is $\delta_v = -2.717$. The story is slightly more complicated for the halo barrier. Choosing the value $\delta_c = 1.686$ supposes that the overdensities already collapsed into bound structures. Voids that are trapped in such overdense structures are subject to the infall of matter, decreasing their radii until at full collapse they simply disappear. Any void embedded in an overdensities that already surpassed the point of turn-around will also already see its diameter shrinking. Hence, by imposing $\delta_c = 1.686$, the voids in collapsed structures are taken to have a zero radius, while those in collapsing structures are not altered. This choice of the void barrier value thereby overestimates

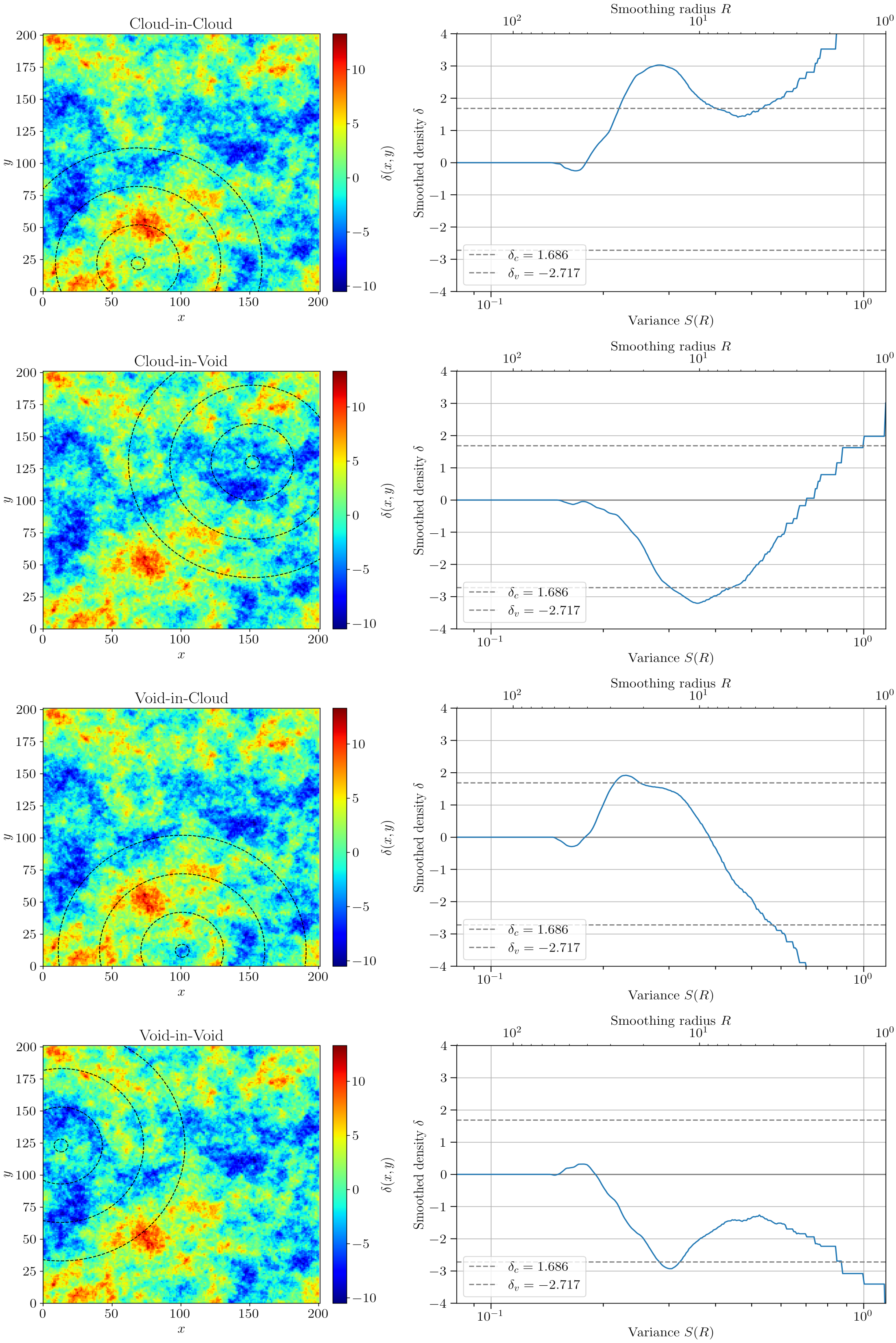

Figure 5.2: Four trajectories as calculated in a 2D GRF with spectral index $n = -2.5$ and a top-hat filtering function. The plot on the left shows the GRF and the point at which the trajectory will be taken, and on the right, the corresponding smoothed density paths are shown. From top to bottom, this shows the cloud-in-cloud, cloud-in-void, void-in-cloud, and void-in-void modes.

the size of embedded voids. A value of $\delta_{\text{t-a}} = 1.062$, conversely, underestimates the size of voids. In this case, all voids that are embedded in halos that underwent turn-around are taken to have a diameter of zero, even though they could very well have some non-zero radius. Ongoing research tries to find an optimal choice of δ_c in this void-in-cloud problem, for now a value of 1.686 is adopted when necessary, while keeping in mind that this overestimates the typical void size.

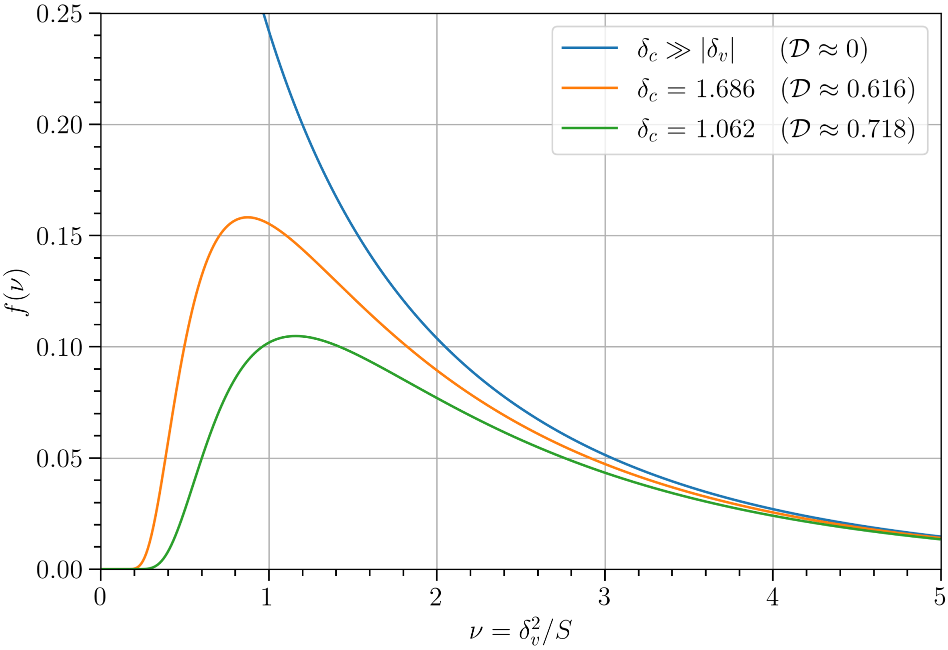

Figure 5.3: Scaled void size distribution. The curves show the simplified distribution $f(\nu)$ of the fraction of trajectories crossing δ_v without having crossed δ_c at some lower S, according to Eq. 5.5 with three different values for the cloud-and-void parameter. A constant value of $\delta_v = -2.717$ was adopted for the void barrier. Three different values for the halo barrier are used: $\delta_c = 1.686$ as predicted by the spherical collapse model in an EdS, $\delta_c = 1.062$ as the turn-around factor found in the same model, and $\delta_c \to 0$ as a limiting case in which the void-in-cloud problem is completely irrelevant. More massive voids correspond to lower S and thereby higher $\nu \equiv \delta_v^2/S$. The void-in-cloud problem is irrelevant for them.

5.1.a Void Size Distribution

The excursion set formalism for halos has been extended to include the effects of the void barrier δ_v by Sheth and Van de Weygaert 2004. This chapter is built entirely upon these results. Let $\mathcal{F}$ denote the fraction of trajectories that cross δ_v at some pseudotime S, without having crossed δ_c at some $S' < S$. Physically speaking, $\mathcal{F}$ should be equal to the first-crossing distribution (Eq. 4.20) through the threshold δ_v minus the number of trajectories that cross δ_c for some smaller S:

$$\mathcal{F}(S, \delta_v, \delta_c) = f(S, \delta_v) - \int_0^S f(S', \delta_c) \cdot f\left(S, \delta_v \,\middle|\, S', \delta_c\right) \,\mathrm{d}S'. \tag{5.1}$$

The first term in the integrand represents those trajectories that pass through the collapse barrier δ_c at time S', the second term filters out those paths that pass through δ_v at scale S, given that they already passed through the point (S', δ_c). Integrating the product thereby gives the number of trajectories that pass through (S, δ_v) and (S', δ_c) with $S' < S$. This removes all the void-in-cloud underdensities, but leaves for example the cloud-in-void situations untouched. The solution to Eq. 5.1 can be found through Laplace transformations [Sheth and Van de Weygaert 2004]:

$$S\,\mathcal{F}(S, \delta_v, \delta_c) = \sum_{j=1}^{\infty} \frac{j^2\pi^2\mathcal{D}^2}{\delta_v^2/S} \frac{\sin(j\pi\mathcal{D})}{j\pi} \exp\left\{-\frac{j^2\pi^2\mathcal{D}^2}{2\delta_v^2/S}\right\}, \tag{5.2}$$

where $\mathcal{D}$ denotes the void-and-cloud parameter:

$$\mathcal{D} \equiv \frac{|\delta_v|}{\delta_c + |\delta_v|}. \tag{5.3}$$

This parameter quantifies the influence of halo evolution on the evolving population of clouds. Its meaning becomes clearer upon integrating $\mathcal{F}$ [Sheth and Van de Weygaert 2004]:

$$\int \mathcal{F}(S, \delta_v, \delta_c)\, \mathrm{d}S = 1 - \mathcal{D} = \frac{\delta_c}{\delta_c + |\delta_v|}, \tag{5.4}$$

which represents the fraction of mass contained in voids. When the void-and-cloud parameter is small, then the probability that the smallest voids disappear through the void-in-cloud process decreases. By the above relation, that implies that most of the mass is incorporated in voids. The converse states that the bigger $\mathcal{D}$ becomes, the smaller the mass fraction in voids will be since the void-in-cloud process effectively removes engulfed voids from the counting process.

Infinite series are somewhat cumbersome to work with since the true functional form is not directly visible. For $\delta_c/|\delta_v| \geq 1/4$, Sheth and Van de Weygaert 2004 approximate Eq. 5.2 to:[1]

$$\nu f(\nu) \approx \sqrt{\frac{\nu}{2\pi}} \exp\left\{-\frac{\nu}{2}\right\} \exp\left\{-\frac{|\delta_v|}{\delta_c}\frac{\mathcal{D}^2}{4\nu} - \frac{2\mathcal{D}^4}{\nu^2}\right\}, \tag{5.5}$$

where $\nu \equiv \delta_v^2/S = \delta_v^2/\sigma^2$ is the fractional underdensity and $\nu f(\nu)\, \mathrm{d}\nu/\nu \approx S\mathcal{F}\, \mathrm{d}S/S$. The first exponential shows the decaying number density for large voids, while the second exponential suppresses the existence of tiny voids. The peak of the distribution can be determined graphically to correspond to $\nu \approx 1$. Eq. 5.5 can be rewritten using the chain rule in terms of S and the barriers explicitly:

$$f(\nu)\, \mathrm{d}\nu = f(\delta_v^2/S)\, \mathrm{d}(\delta_v^2/S) = \frac{1}{\sqrt{2\pi}} \frac{\delta_v}{S^{3/2}} \exp\left\{-\frac{\delta_v^2}{2S}\right\} \exp\left\{-\frac{|\delta_v|}{\delta_c}\frac{\mathcal{D}^2 S}{4\delta_v^2} - \frac{2\mathcal{D}^4 S^2}{\delta_v^4}\right\} \mathrm{d}S \tag{5.6}$$

Note that in the limit where $\mathcal{D} \to 0$, corresponding to a universe in which the void-in-cloud process can be safely ignored, the second exponential term approaches unity. This restores the broken symmetry between the void-in-cloud and cloud-in-void modes: both do not significantly contribute to the counting of voids. In this limit, the resulting expression for the void distribution in Eq. 5.6 takes on the same mathematical form as Eq. 4.20 for the halo distribution.

---

[1] Jennings, Li, and Hu 2013 argued that the accuracy of this approximation is uncontrolled in certain limits and instead propose to use a piecewise continuous approximation, where four terms of Eq. 5.2 remain. However, this work will stick to Eq. 5.5 due to its validity in the relevant regime and due to the fact that it is easy to see that it reduces to Eq. 4.20 in the limit where $\mathcal{D}$ approaches zero.

5.1.b The Void Mass Function

Determining the mass of halos is relatively easy. After all, they form overdensities whose gravitational effect could technically speaking be measured and reverse-engineered to mass distributions. This becomes slightly more challenging in the context of the cosmic underdensities. One way to infer the mass for a void is to use the simplest conversion from volume to mass via the average density: $M = \rho \cdot V/(1.697)^3$, where the value 1.697 corresponds to the factor by which the co-moving radius of a matured void increased according to Eq. 3.53. Similar to the result in halo excursion theory, the number density n of voids of masses within $[M, M + \mathrm{d}M]$ at time t can be determined to be:

$$n(M,t)\,\mathrm{d}M = S\mathcal{F}\frac{\bar{\rho}}{m^2}\left|\frac{\mathrm{d}\ln S}{\mathrm{d}\ln M}\right|\,\mathrm{d}M \tag{5.7}$$

$$= \sqrt{\frac{\nu}{2\pi}}\exp\left\{-\frac{\nu}{2}\right\}\exp\left\{-\frac{|\delta_v|}{\delta_c}\frac{\mathcal{D}^2}{4\nu}-\frac{2\mathcal{D}^4}{\nu^2}\right\}\frac{\bar{\rho}}{M^2}\frac{\mathrm{d}\ln S}{\mathrm{d}\ln M}\,\mathrm{d}M, \tag{5.8}$$

where again the time dependence enters via the barrier values. Besides a formulation in terms of mass M, one can equally well describe the void distribution in terms of volume or radius:

$$\sigma^2(M) = S(M) = \delta_{\text{lin}}^2\left(\frac{M}{M_*}\right)^{-\alpha} = \delta_{\text{lin}}^2\left(\frac{V}{V_*}\right)^{-\alpha} = \delta_{\text{lin}}^2\left(\frac{R}{R_*}\right)^{-3\alpha}, \tag{5.9}$$

where $\alpha = (n+3)/3$ and where a pure power spectrum $P(k) \propto k^n$ was assumed. The void scale distribution in Eq. 5.6 may therefore equally well be rewritten in terms of mass, volume or radius:

$$f(S)\,\mathrm{d}S \propto f(M)\,\mathrm{d}M \propto f(V)\,\mathrm{d}V \propto f(R)\,\mathrm{d}R. \tag{5.10}$$

The cumulative mass fraction $\mathbb{P}(> M, t)$ found in voids can be found upon integrating Eq. 5.6:

$$\mathbb{P}(> M,t) = \int_M^\infty \frac{1}{\sqrt{2\pi}}\frac{\delta_v(t)}{S^{3/2}(M')}\exp\left\{-\frac{\delta_v^2(t)}{2S(M')}\right\}\exp\left\{-\frac{|\delta_v(t)|}{\delta_c(t)}\frac{\mathcal{D}^2 S(M')}{4\delta_v^2(t)}-\frac{2\mathcal{D}^4 S^2(M')}{\delta_v^4(t)}\right\}\mathrm{d}M'. \tag{5.11}$$

In particular, in the limit where $\mathcal{D} \to 0$, this approaches:

$$\mathbb{P}(> M,t) = \int_M^\infty \frac{1}{\sqrt{2\pi}}\frac{\delta_v(t)}{S^{3/2}(M')}\exp\left\{-\frac{\delta_v^2(t)}{2S(M')}\right\}\mathrm{d}M' = \mathrm{erfc}\left(\frac{\delta_v(t)}{\sqrt{2S(M)}}\right), \tag{5.12}$$

where erfc(x) denotes the complimentary error function. Indeed, as $M \to 0$ and hence $S \to \infty$, it follows from this result that $\mathbb{P}(> 0, t) = 1$.

5.2 Merging & Absorption

The trajectories $\delta(S)$ discussed so far can be used to explore the merging histories of halos and voids. Following these merging events in the normal temporal sequence means that the trajectories start at early times t with low masses and grow over time. In terms of trajectory plots, reading off the accretion events should then be done by starting at a high S and continuing to the left. The mass of the object is taken to correspond to the lowest S for which the trajectory crosses the barriers δ_c or δ_v. The horizontal jumps when moving from one barrier-crossing to the other corresponds to sudden increases in the mass of the object. These can be interpreted as merging events [Lacey and Cole 1993], as is depicted graphically in Fig. 5.6. In fact, any time δ increases can be interpreted as tiny accretions of mass. Following the work by Lacey and Cole 1993 on halo merger rates in hierarchical models, this section is dedicated to finding the analogous result for voids. These calculations were already performed for the largest voids by Russell 2013, by taking the limit $\mathcal{D} \to 0$.

5.2.a Conditional Void Size Distribution

Recall that the general formula for the fraction of trajectories passing through (S, δ_v), only permitted to pass through δ_c for some $S' > S$, is given by Eq. 5.6. The probability that a trajectory has its first barrier-crossing at $|\delta_{v,1}|$ in the range $[S_1, S_1 + \mathrm{d}S_1]$, given that it already passes through $|\delta_{v,2}| < |\delta_{v,1}|$ at $S_2 < S_1$, will be denoted by $f_{S_1}\left(S_1, \delta_{v,1} \;\middle|\; S_2, \delta_{v,2}\right) \mathrm{d}S_1$. By realizing that this is nothing more than Eq. 5.6 after shifting the origin to new starting position $(S_2, \delta_{v,2})$, a simple variable transformation $|\delta_v| \to |\delta_{v,1}| - |\delta_{v,2}|$, $S \to S_1 - S_2$ and $\delta_c \to \delta_{c,1} - |\delta_{v,2}|$ is enough to calculate the conditional probability [Lacey and Cole 1993; Bond et al. 1991; Bower 1991]:

$$f\left(S_1, |\delta_{v,1}| \;\middle|\; S_2, |\delta_{v,2}|\right) \mathrm{d}S_1 = \frac{1}{\sqrt{2\pi}} \frac{|\delta_{v,1}|-|\delta_{v,2}|}{(S_1 - S_2)^{3/2}} \exp\left\{-\frac{(|\delta_{v,1}|-|\delta_{v,2}|)^2}{2(S_1 - S_2)}\right\} \exp\left\{-\frac{|\delta_{v,1}|-|\delta_{v,2}|}{\delta_{c,1} - |\delta_{v,2}|} \frac{\overline{\mathcal{D}}^2 (S_1 - S_2)}{4(|\delta_{v,1}|-|\delta_{v,2}|)^2} - \frac{2\overline{\mathcal{D}}^4 (S_1 - S_2)^2}{(|\delta_{v,1}|-|\delta_{v,2}|)^4}\right\} \mathrm{d}S_1. \tag{5.13}$$

where now the adapted void-and-cloud parameter $\overline{\mathcal{D}}$ takes the specific form:

$$\overline{\mathcal{D}} = \frac{|\delta_{v,1}|-|\delta_{v,2}|}{\delta_{c,1} - |\delta_{v,2}| + |\delta_{v,1}| - |\delta_{v,2}|} = \frac{|\delta_{v,1}|-|\delta_{v,2}|}{\delta_{c,1} + |\delta_{v,1}| - 2|\delta_{v,2}|}. \tag{5.14}$$

Meanwhile, Eq. 5.9 can be used to find the derivative of S with respect to M, V and R:

$$\left|\frac{\mathrm{d}\ln S}{\mathrm{d}\ln M}\right| = \left|\frac{\mathrm{d}\ln S}{\mathrm{d}\ln V}\right| = \alpha \quad \text{and} \quad \left|\frac{\mathrm{d}\ln S}{\mathrm{d}\ln R}\right| = 3\alpha, \tag{5.15}$$

which allows for the conditional probability in Eq. 5.13 to be re-expressed in terms of the corresponding radii:

$$\begin{aligned} f\left(R_1, |\delta_{v,1}| \;\middle|\; R_2, |\delta_{v,2}|\right) \left|\frac{\mathrm{d}S_1}{\mathrm{d}R_1}\right| \mathrm{d}R_1 = {} & \frac{3\alpha \delta^2_{\mathrm{lin},v,1} (|\delta_{v,1}|-|\delta_{v,2}|)}{\sqrt{2\pi} R_1 \left(\delta^2_{\mathrm{lin},v,1} \left(\frac{R_1}{R_*}\right)^{-3\alpha} - \delta^2_{\mathrm{lin},v,2} \left(\frac{R_2}{R_*}\right)^{-3\alpha}\right)^{3/2}} \left(\frac{R_1}{R_*}\right)^{-3\alpha} \\ & \exp\left\{-\frac{(|\delta_{v,1}|-|\delta_{v,2}|)^2}{2\left(\delta^2_{\mathrm{lin},v,1} \left(\frac{R_1}{R_*}\right)^{-3\alpha} - \delta^2_{\mathrm{lin},v,2} \left(\frac{R_2}{R_*}\right)^{-3\alpha}\right)}\right\} \\ & \exp\left\{-\frac{|\delta_{v,1}|-|\delta_{v,2}|}{\delta_{c,1} - |\delta_{v,2}|} \frac{\overline{\mathcal{D}}^2 \left(\delta^2_{\mathrm{lin},v,1} \left(\frac{R_1}{R_*}\right)^{-3\alpha} - \delta^2_{\mathrm{lin},v,2} \left(\frac{R_2}{R_*}\right)^{-3\alpha}\right)}{4(|\delta_{v,1}|-|\delta_{v,2}|)^2}\right\} \\ & \exp\left\{-\frac{2\overline{\mathcal{D}}^4 \left(\delta^2_{\mathrm{lin},v,1} \left(\frac{R_1}{R_*}\right)^{-3\alpha} - \delta^2_{\mathrm{lin},v,2} \left(\frac{R_2}{R_*}\right)^{-3\alpha}\right)^2}{(|\delta_{v,1}|-|\delta_{v,2}|)^4}\right\} \mathrm{d}R_1. \end{aligned} \tag{5.16}$$

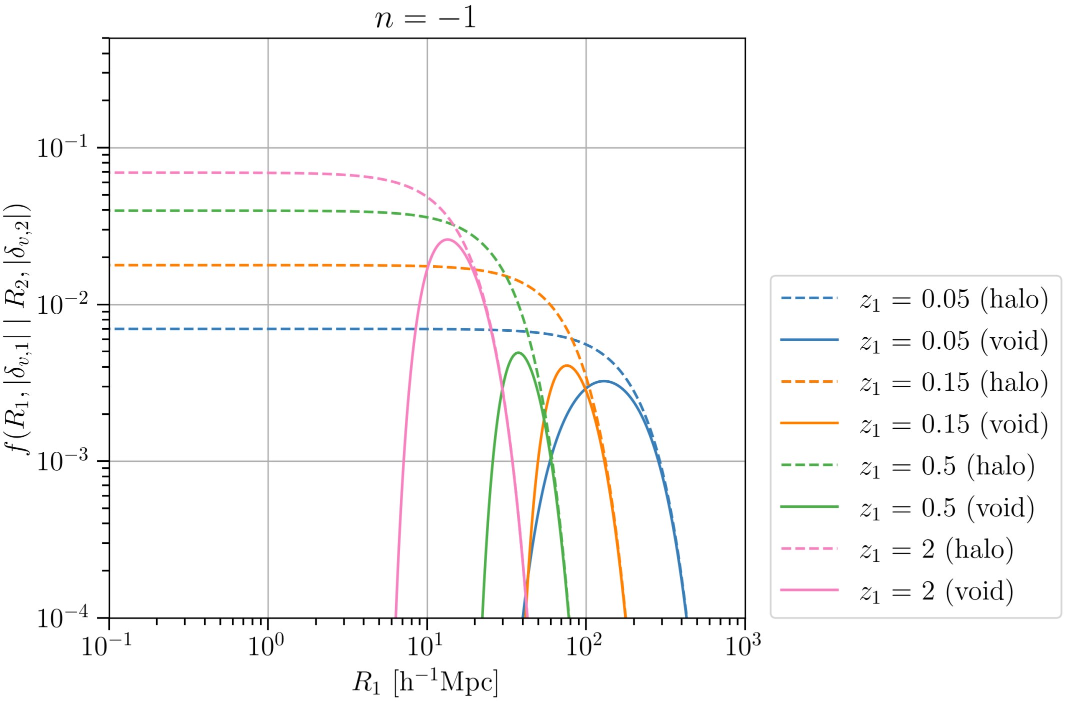

Figure 5.4: Conditional void size distribution. The plot shows the conditional probability of a void of size R_1 at time $\delta_{v,1} = \delta_v(1 + z_1)$ later being merged into a void of size $R_2 = 2R_1$ at time $\delta_{v,2} = \delta_v$, as calculated in Eq. 5.16 with a universe in which $n = -1$. A characteristic radius of $R_* = 8\,\mathrm{h^{-1}Mpc}$ and $\sigma_8 = 0.8$ were chosen for normalisation. The dashed lines represent the result for halos, the solid curves the same configuration but then for voids. The exponential cut-off for halos at large radii is also apparent for the voids. Note how this decay moves to higher radii for more recent redshifts, which is indicative of hierarchical structure formation. A second cut-off at relatively low radii is unique to voids and stems from the void-in-cloud problem.

This quantity can be interpreted as the conditional probability that a void of size R_1 at time t_1 incorporates into a void of size R_2 at a later time t_2. In a binary model, choosing $R_2 = 2R_1$ could be used to get an indication of the conditional probability of doubling in size in a certain time frame. This is shown in Fig. 5.4 for the case of an $n = -1$ universe and where $z_2 = 0$ was set for convenience. For both halos and voids, there is an exponential cut-off at large scales in the size probability distribution that moves to higher radii for smaller redshifts. It is also clear that the distribution reaches the highest values for increasing redshift. In a hierarchical model for structure formation for halos, this could be interpreted as the merging of high redshift overdensities to form larger objects in more recent times [Lacey and Cole 1993; Russell 2013]. The void-in-cloud asymmetry breaking causes the void distribution to have a second exponential decay at low radii: a tiny void cannot merge into a void double its size, since the latter were already removed by void collapse at that redshift. As expected in hierarchical models, also this cut-off moves to higher radii for decreasing redshift.

5.2.b Power Law Dependence

The conditional void size probability in Fig. 5.4 was calculated for an $n = -1$ power spectrum, though it is interesting to compare this to other toy universes. In an $n = 0$ universe for instance, the initial conditions do not contain as many large blobs as compared to the $n = -1$ model. The

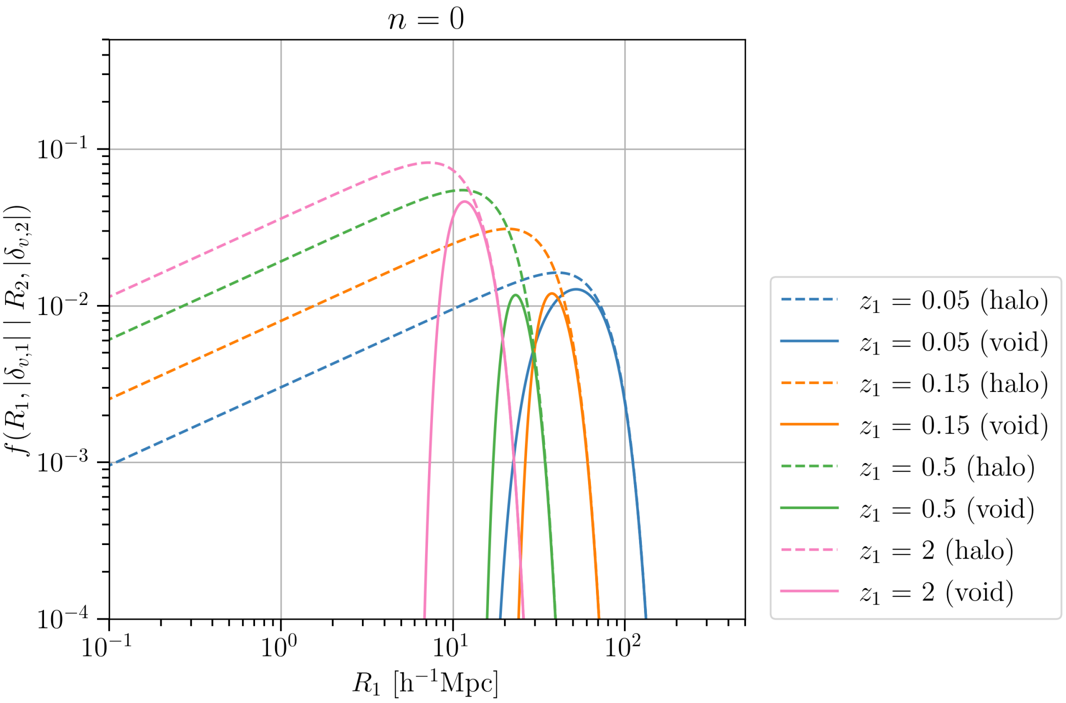

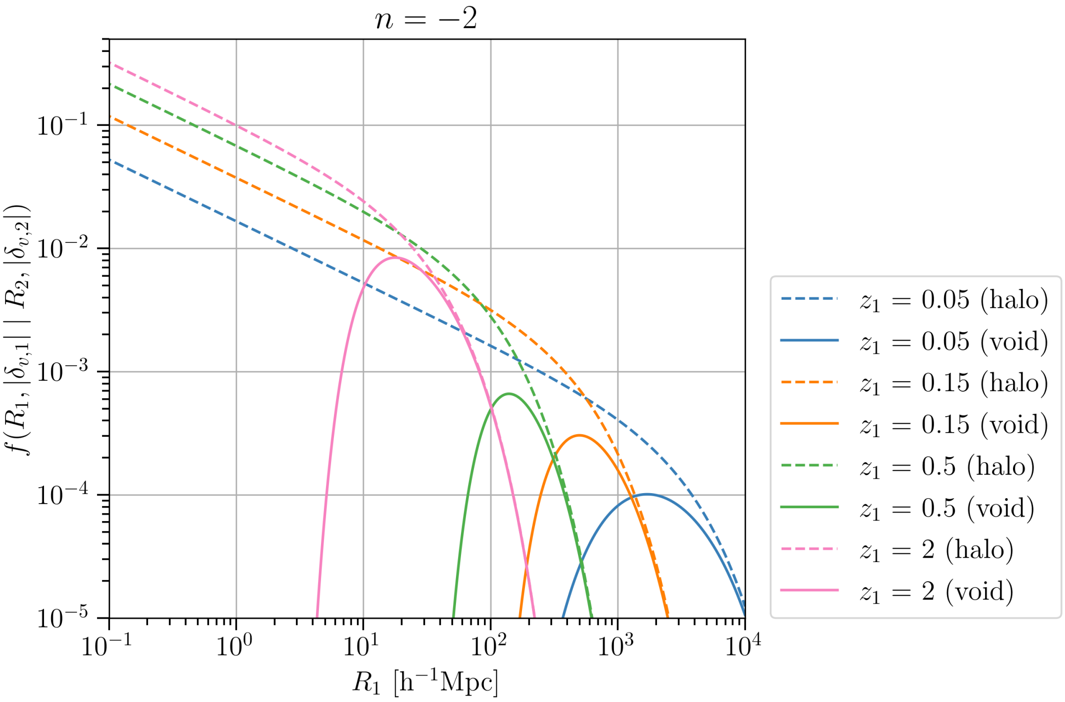

Figure 5.5: The conditional probability of a void of size R_1 at time $\delta_{v,1} = \delta_v(1 + z_1)$ later being merged into a void of size $R_2 = 2R_1$ at time $\delta_{v,2} = \delta_v$, as calculated in Eq. 5.16. The figure at the top corresponds to a pure power law universe with $n = 0$, while the bottom figure corresponds to $n = -2$. Again, the solid lines indicate the results for voids, while the halo lines represent the halo theory. The dissimilarity is caused by the void-in-cloud problem. As for the case where $n = -1$, halos have a single exponential decay at high radii, whereas voids also have a second cut-off at lower radii.

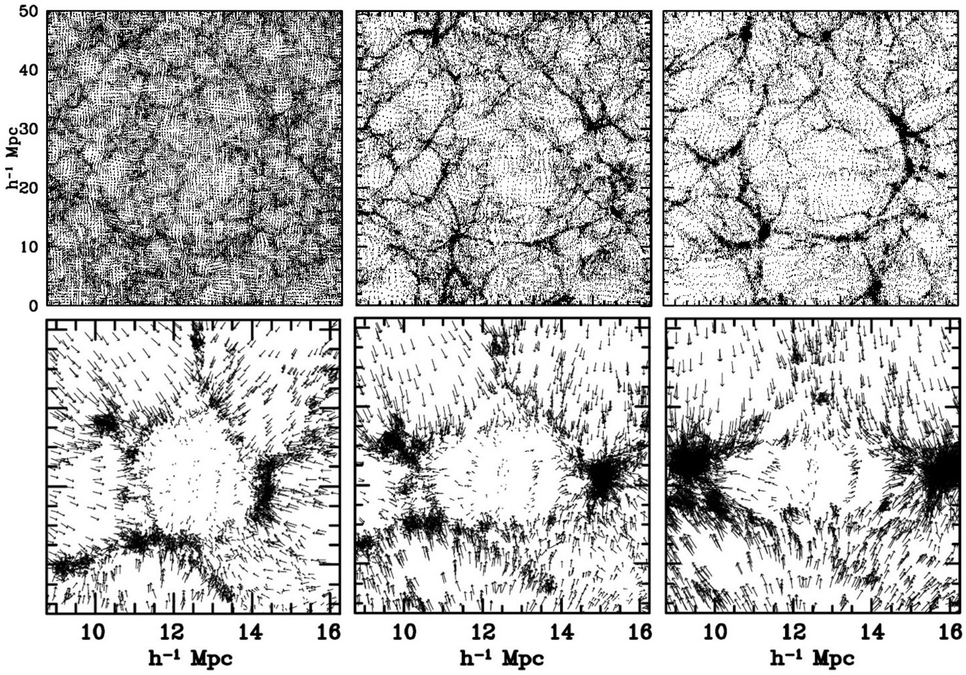

Figure 5.6: Void merging (top row) and collapsing (bottom row). This schematic graphic aims to show the two main modes in the evolution of voids. The top row shows the result of an N-body simulation in increasing time order. As time progresses, a web-like structure emerges with clearly visible underdensities. These voids slowly merge to form the larger underdensity visible in the rightmost panel. The bottom row shows three separate instances of void collapse, with slightly different mass configurations. The arrows indicate velocity vectors. Over time, the voids located at the center of each panel cease to exist as matter hails down. Source: [Van de Weygaert and Van Platen 2009].

conditional void size probability for this particular system, as is visible in the top diagram of Fig. 5.5, is shifted to slightly lower radii. The main difference is the behaviour for the smaller halos: in an $n = -1$ system, the probabilities locally remained constant as a function of small radius, but in an $n = 0$ this likelihood decreases for smaller and smaller halos. The conditional halo size distribution all peak at some radius between 10 and $100\,\mathrm{h}^{-1}$Mpc in the curves drawn. Exactly the opposite happens in an $n = -2$ universe, in which larger structures appear in the initial density field: for halos, the conditional probability rises as the radius decreases. The high radius cut-off for both structure types move to higher radii, as visible in the bottom diagram of Fig. 5.5.

5.2.c Merger Rates

In order to calculate the merging and absorption rate, first another conditional probability has to be calculated. The conditional probability that a trajectory first moves through $(S_1, \delta_{v,1})$ and then develops to move through $\delta_{v,2}$ within some range $[S_2, S_2 + \mathrm{d}S_2]$ can be directly obtained from Eq. 5.13 and is given by the following expression:

$$
\begin{aligned}
f\left(S_2,\delta_{v,2}\,\middle|\,S_1,\delta_{v,1}\right)\,\mathrm{d}S_2 &= \frac{f_{S_1}\left(S_1,\delta_{v,1}\,\middle|\,S_2,\delta_{v,2}\right)\,\mathrm{d}S_1\cdot f_{S_2}\left(S_1,\delta_{v,1}\right)\,\mathrm{d}S_2}{f_{S_1}\left(S_1,\delta_{v,1}\right)\,\mathrm{d}S_1}\\
&= \frac{1}{\sqrt{2\pi}}\frac{|\delta_{v,1}|-|\delta_{v,2}|}{(S_1-S_2)^{3/2}}\frac{\delta_{v,2}}{\delta_{v,1}}\left(\frac{S_1}{S_2}\right)^{3/2}\exp\left\{-\frac{\left(S_1|\delta_{v,2}|-S_2|\delta_{v,1}|\right)^2}{2S_1S_2(S_1-S_2)}\right\}\\
&\quad\exp\left\{-\frac{|\delta_{v,1}|-|\delta_{v,2}|}{\delta_{c,1}-|\delta_{v,2}|}\frac{\overline{\mathcal{D}}^2(S_1-S_2)^2}{4(|\delta_{v,1}|-|\delta_{v,2}|)^2}-\frac{2\overline{\mathcal{D}}^4(S_1-S_2)^2}{(|\delta_{v,1}|-|\delta_{v,2}|)^4}\right\}\\
&\quad\exp\left\{-\frac{\mathcal{D}^2}{4\delta_{c,1}}\left(\frac{S_2^2}{\delta_{v,2}}-\frac{S_1^2}{\delta_{v,1}}\right)-2\mathcal{D}^4\left(\frac{S_2^2}{\delta_{v,2}^4}-\frac{S_1^2}{\delta_{v,1}^4}\right)\right\}\mathrm{d}S_2
\end{aligned}
\tag{5.17}
$$

This quantity is interpreted as the probability that a void of a mass M_1 at time t_1 will have merged at a time $t_2 > t_1$ and gained a mass in the range $[M_2, M_2 + \mathrm{d}M_2]$. The mean transition rate is obtained by taking the limit of Eq. 5.17 when $|\delta_{v,2}|\rightarrow|\delta_{v,1}|\equiv\delta_v$ and $|\delta_{c,1}|\equiv\delta_c$, such that $|\delta_{v,1}|-|\delta_{v,2}|=\mathrm{d}\delta_v$ [Lacey and Cole 1993]. To first order in $\mathrm{d}\delta_v$, this becomes:

$$
\begin{aligned}
\frac{\mathrm{d}^2p}{\mathrm{d}S_2\,\mathrm{d}|\delta_v|}(S_2\to S_1\mid\delta_v) &= \frac{1}{\sqrt{2\pi}}\left(\frac{S_1}{S_2(S_1-S_2)}\right)^{3/2}\exp\left\{-\frac{|\delta_v|^2(S_1-S_2)}{2S_1S_2}\right\}\\
&\exp\left\{-\frac{2(S_1-S_2)^2}{(\delta_c-|\delta_v|)^4}-\frac{\mathcal{D}^2}{4\delta_c}\left(\frac{S_2^2-S_1^2}{\delta_v}\right)-2\mathcal{D}^4\left(\frac{S_2^2-S_1^2}{\delta_v^4}\right)\right\}\mathrm{d}S_2\,\mathrm{d}|\delta_v|
\end{aligned}
\tag{5.18}
$$

The analogous result derived for halos is interpreted as an indicator for merger events, happening in some step with size $\Delta\delta_v$ [Lacey and Cole 1993]. In the infinitesimal case shown above, this reduces so a single accumulation event, hence Eq. 5.18 can be understood as the probability that a void of a volume congruent to S_1 merges with another void with a volume congruent to S_2-S_1 in a time interval $\mathrm{d}|\delta_v|$. From now on, Eq. 5.18 will be referred to as the void transition probability.

The void merging rate is defined to be the rate of change in the transition probability in terms of the total increment in volume due to merging events, all per unit time [Lacey and Cole 1993; Russell 2013]. The void merging rate is thereby:

$$
\begin{aligned}
\frac{\mathrm{d}^2p}{\mathrm{d}\ln\Delta V\,\mathrm{d}\ln t}(V_1\to V_2\mid t) &= \frac{\mathrm{d}^2p}{\mathrm{d}S_2\,\mathrm{d}|\delta_v|}\cdot\left|\frac{\mathrm{d}|\delta_v|}{\mathrm{d}\ln t}\right|\cdot\left|\frac{\mathrm{d}S_2}{\mathrm{d}\ln\Delta V}\right|\\
&= \sqrt{\frac{2}{\pi}}\frac{|\delta_v|}{\sqrt{S_2}}\frac{\Delta V}{V_2}\left(\frac{S_1}{S_1-S_2}\right)^{3/2}\exp\left\{-\frac{|\delta_v|^2(S_1-S_2)}{2S_1S_2}\right\}\cdot\left|\frac{\mathrm{d}\ln|\delta_v|}{\mathrm{d}\ln t}\right|\\
&\exp\left\{-\frac{2(S_1-S_2)^2}{(\delta_c-|\delta_v|)^4}-\frac{\mathcal{D}^2}{4\delta_c}\left(\frac{S_2^2-S_1^2}{\delta_v}\right)-2\mathcal{D}^4\left(\frac{S_2^2-S_1^2}{\delta_v^4}\right)\right\}\cdot\left|\frac{\mathrm{d}\ln\sqrt{S_2}}{\mathrm{d}\ln V_2}\right|.
\end{aligned}
\tag{5.19}
$$

This quantity, $\mathrm{d}^2p/\mathrm{d}\ln\Delta V\,\mathrm{d}\ln t$, represents the number of voids of size $\Delta V\equiv V_2-V_1$ that are merged in one Hubble time by a void of volume V_1. For an EdS universe specifically, $|\,\mathrm{d}\ln|\delta_v|/\mathrm{d}\ln t\,| = 2/3$. The resulting void merging rate in an $n=-1$ universe is shown in the left plot of Fig. 5.7, against the same result for halos in the graph on the right. The region in the top-left corresponds to the minor merging events and the area in the bottom-right to the major merging events. The latter is mainly applicable for the smaller objects since the largest objects do not have many neighbors of similar sizes to merge with. It is not easy to see how the results for underdensities differ from that of the overdensities in this particular figure, so Fig. 5.8 specifically shows the difference in the curves as halos minus voids. The plot suggests

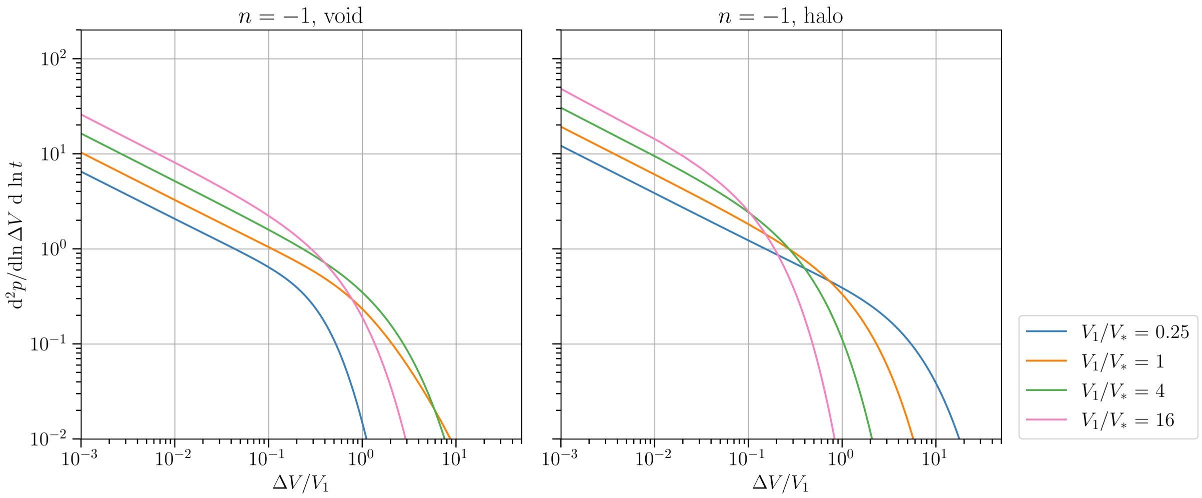

Figure 5.7: Void and halo merger rates. The plot on the left shows the rate at which the growing voids merge as predicted by Eq. 5.19 for an $n = -1$ universe, and the plot on the right shows the analogous results for halos. Four different values for V_1/V_* are followed, essentially corresponding to voids of four different initial sizes. Again, the values $R_* = 8\,\mathrm{h}^{-1}\mathrm{Mpc}$ and $\sigma_8 = 0.8$ were used for normalisation. The top-left region of each plot corresponds to the minor merger events in which, for example, relatively small objects collide with an initially large V_1. The bottom-right area can be associated with big merger events, in which the mass of the final product is much larger than that of the main progenitor. Note how functional form starts to differ between voids and halos in this region.

that small merger events are more common for halos than for voids. Recalling that small merger events consist of the accretion of relatively small objects onto existing larger structures, this observation could be tied to the fact that the number density of small voids is severely limited by the void-in-cloud problem, as opposed to halos.

A power spectrum with a smaller value of the spectral index n has more power on large scales compared to small scales, which would make major merger events more frequent. This reasoning is indeed confirmed when performing the same calculations in an $n = -2$ universe, as can be checked in Fig. A.13. The opposite reasoning holds true for higher spectral indices: more power is found on the smaller scales, making minor merger events more common. This is again confirmed by the results of Fig. A.15.

5.2.d Absorption Rates

The accretion rate for halos is defined to be the rate of mass increase due to minor mergers, and the absorption rate is defined to be the analogous quantity but for voids. This rate can be interpreted as the mass- or volume-weighted merger rate, so its functional form for voids simply comes down to multiplying 5.19 by $\Delta V/V_1$ [Lacey and Cole 1993]:

$$\begin{aligned}\frac{\Delta V}{V_1}\frac{\mathrm{d}^2p}{\mathrm{d}\ln\Delta V\,\mathrm{d}\ln t} &= \sqrt{\frac{2}{\pi}}\,\frac{|\delta_v|}{\sqrt{S_2}}\,\frac{\Delta V^2}{V_1V_2}\left(\frac{S_1}{S_1-S_2}\right)^{3/2}\exp\left\{-\frac{|\delta_v|^2(S_1-S_2)}{2S_1S_2}\right\}\\ &\exp\left\{-\frac{2(S_1-S_2)^2}{(\delta_c-|\delta_v|)^4}-\frac{\mathcal{D}^2}{4\delta_c}\left(\frac{S_2^2-S_1^2}{\delta_v}\right)-2\mathcal{D}^4\left(\frac{S_2^2-S_1^2}{\delta_v^4}\right)\right\}\cdot\left|\frac{\mathrm{d}\ln|\delta_v|}{\mathrm{d}\ln t}\right|\cdot\left|\frac{\mathrm{d}\ln\sqrt{S_2}}{\mathrm{d}\ln V_2}\right|.\end{aligned}\tag{5.20}$$

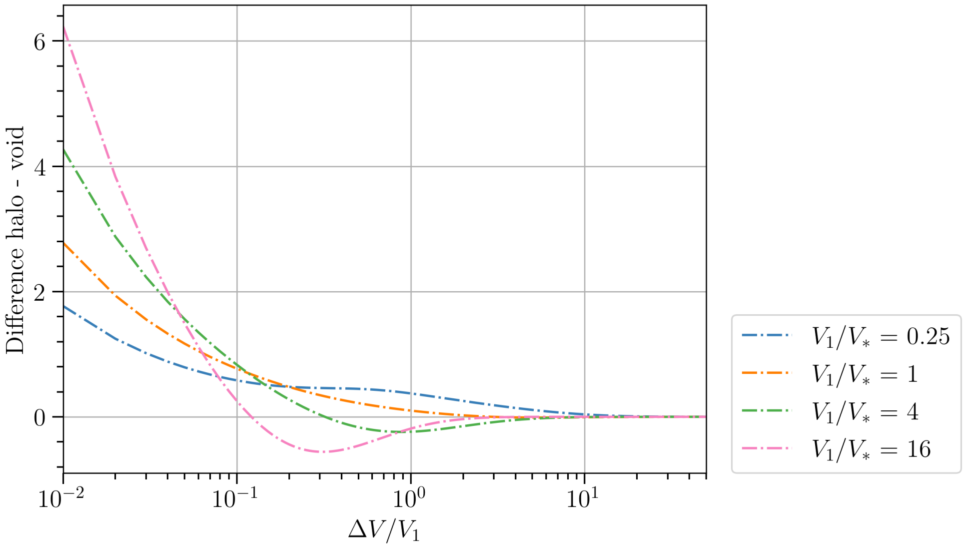

Figure 5.8: Halo - void merger rate difference. These curves show the difference between the halo merger rate and void merger rate for the $n = -1$ universe, as depicted in Fig. 5.7. Note how the y-axis is no longer log-scale. The difference between the two is the largest for minor merger events, indicating that small mergers are more common for halos than for voids. Beware that the difference goes to zero for the largest merger events, but that this simply follows from both merger rates approaching zero in that limit.

In other words, the quantity $\Delta V/V_1 \cdot \mathrm{d}^2p/\mathrm{d}\ln\Delta V\,\mathrm{d}\ln t$ may be interpreted as the fractional mass accreted during one Hubble time. An example is shown in Fig. 5.9, in which the absorption rate is compared between voids and halos. Unlike merger rates, the absorption and accretion rates are well-peaked at a value of $\Delta V/V_1 \sim 10^{-1} - 10^{0}$, indicating that these structures gain most of their mass by merging with objects of very similar sizes. The overall shape of the distribution has a complex dependence on the initial void size V_1/V_* in the case of voids but shows a clear ordering when returning to the halo example. Also note how, for instance, the $V_1/V_* = 0.25$ curve is heavily attenuated in the case of voids. As of now, it is not yet clear how the vast difference between these results arises and has to be studied in future work. For reference, also the difference between the curves is explicitly shown in Fig. 5.10.

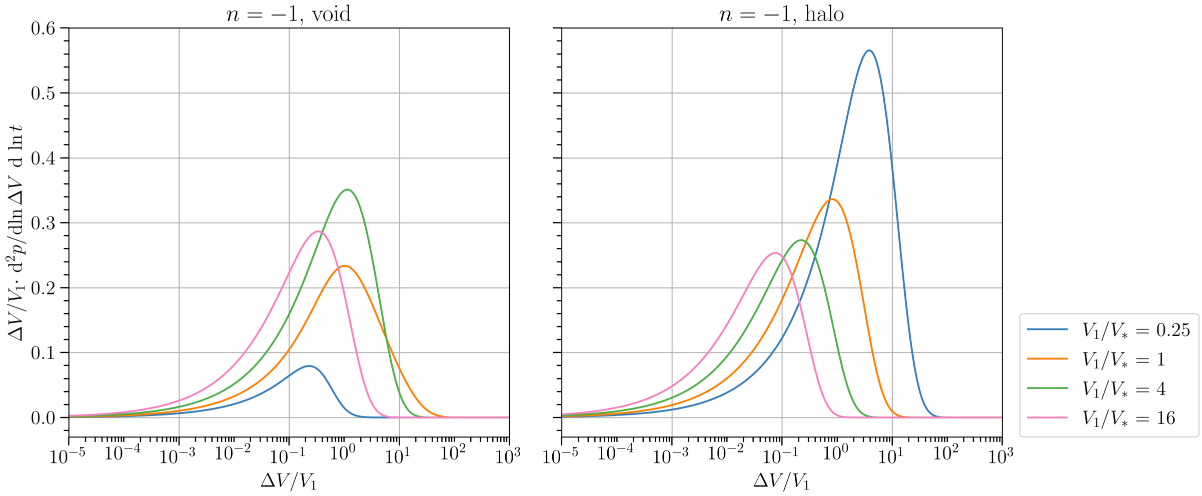

Figure 5.9: Void absorption and halo accretion rates. The plot on the left shows the absorption rate for voids as predicted by Eq. 5.20 for an $n = -1$ universe, and the plot on the right shows the analogous accretion results for halos. Four different values for V_1/V_* are followed, essentially corresponding to voids of four different initial sizes. Again, the values $R_* = 8\,\mathrm{h}^{-1}\mathrm{Mpc}$ and $\sigma_8 = 0.8$ were used for normalization. For both voids and halos, the distributions are well-peaked for $\Delta V/V_1 \sim 10^{-1} - 10^0$. This shows that these structures gain most of their mass by merging with objects of approximately equal sizes. Also note how the curves corresponding to the same initial void sizes have vastly different scales when comparing voids to halos. The clear ordering in the four curves seen for halos is suddenly lost in the case of voids.

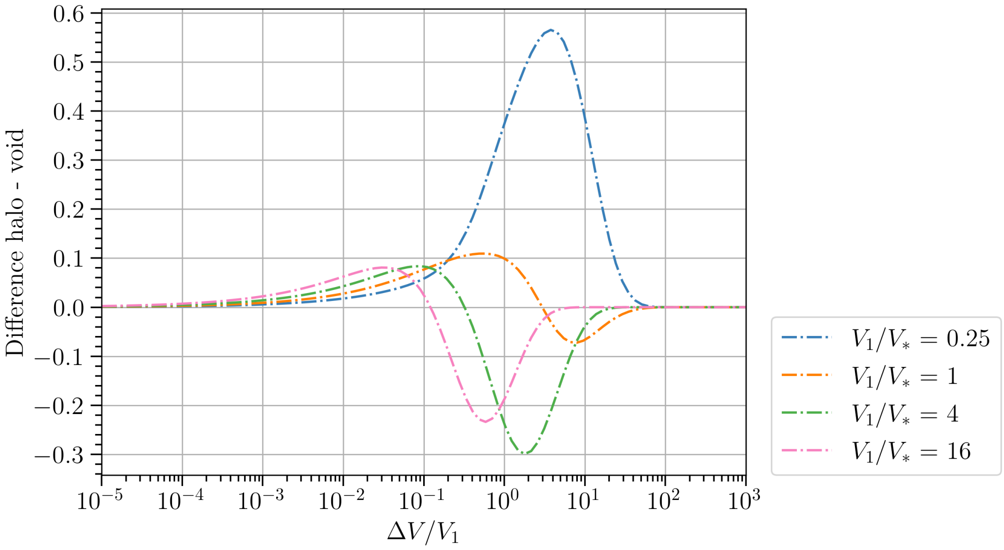

Figure 5.10: Halo - void accretion rate difference. These curves show the difference between the halo accretion rate and void absorption rate for the $n = -1$ universe, as depicted in Fig. 5.9. Note how the y-axis is no longer log-scale. The curves show a strong dependence on the initial void size V_1/V_*. As explained in the main body, what exactly leads to these seemingly peculiar results has not yet been determined and should be studied in future work.

Summary & Discussion

The grand tapestry of the cosmos, where celestial ballets unfold and mysteries abound, continues to amaze generations of scientists. This thesis specialized in the formation of structures on the largest cosmic scales and explored the differences that arise between overdense halos and underdense voids. The first three chapters laid the foundation by discussing the evolution of the primordial density fluctuation field with the help of linearized gravity and the spherical model. Often assumed to be a Gaussian Random Field, the density field could be fully described in terms of its first and second moments, or equivalently in terms of the power function. The complex subsequent evolution of these blobs under the force of gravity is practically impossible to calculate analytically, but by using the spherically symmetric shell model, the non-linear regime could still be probed by means of the linearized theory. For halos, the infall epoch of overdense clouds could be connected to the linearly extrapolated density excess, leading to the critical collapse value δ_c. Similarly, for voids the epoch of shell-crossing was used to explore the underdense regions in the non-linear regimes, which led to the critical value for shell-crossing δ_c.

Based on δ_c and the assumption of the primordial density field being a Gaussian Random Field, Press & Schechter deduced a heuristic formula for the halo mass function. This model was later formalized by Bond, Cole, Efstathiou, and Kaiser by approaching the same problem from the point of view of excursion sets. The well-known cloud-in-cloud problem could now be accounted for and led to a self-consistent theory. However, in order to include the cosmic voids in the model, the excursion set formalism had to be extended to include the void barrier δ_v. This was pioneered in the work of Sheth & Van de Weygaert. Adding voids does not simply add a single number to the framework, because three new problems naturally arose: the void-in-cloud, cloud-in-void and void-in-void modes. Especially the void-in-cloud model proved problematic for its ability to remove small voids when these are embedded in overdense structures. Moreover, this mode destroyed the symmetry between the halos and voids, though their similarity remained for the biggest of voids. In the extended excursion set formalism, the two-barrier problem led to the size distribution of voids and showed that indeed the number densities of small voids is attenuated by the void-in-cloud mode. In the final subsection, conditional size probabilities, merger rates, and absorption and accretion rates were compared between voids and halos. This revealed that these quantities behave in a more complex, perhaps even erratic, manner than halos. The underlying physical processes are yet to be understood in detail.

A natural next step for future research would be to try to understand the physical processes shaping the void merger rates and void absorption rates and compare these analytical results to numerical simulations. In particular, the void conditional size distribution, merger rate, and absorption rate could be tested against these algorithms, to help identify for what void sizes the analytical results derived in this work are valid and applicable. Creating such a code is in reality much harder than it seems, for it has to implement certain void-finding algorithms [Aikio and Mahonen 1998; Einasto, Einasto, and Gramann 1989; Ryden 1995; Ryden and Melott 1996]. This essentially comes down to how a void should be defined in N-body simulations. In this work, shell-crossing was used as an indicator for void maturity, but none of the numerical void locators implement this condition. One of the main challenges is hence to build a numerical framework that can handle the non-linear evolution of evolving voids.

Moreover, future work could look into the dependency of the void merger tree algorithm on cosmological parameters and initial conditions. For example, the spherical model assumed an Einstein-de Sitter universe for simplicity. In section 3.3 it was shown how these results generalize to other cosmologies for the overdensities and subsequently concluded that the halo collapse barrier only slightly changed for different cosmological parameters. It could be interesting to analyze to what extent this remains true for voids. In the case that the void barrier is again weakly depending on $\Omega_{m,0}$, then that confirms that at least the results from the spherical void model stay relatively constant. In the same section, the ellipsoidal model for halos was introduced, which turned out to be a more reliable model for reality than assuming perfect spherically symmetric overdensities. However, such an extension for the spherical void model would be irrelevant because of their tendency towards sphericity over time. In any case, it might be useful to look specifically into the effect of other physical effects, such as the tidal forces mentioned before.

Finally, another interesting path to take is to complete the remaining applications of Lacey & Cole's halo theory to voids. The work of Russell 2013 already provides these in the case of the largest voids, where the two-barrier problem essentially reduces to a single barrier. This work, however, derived the conditional void size probabilities, void merging rates, and absorption rates for voids of general sizes. Possible extensions of the void merger tree algorithm could look into the void formation and survival times. The formation time of a void of mass M would be defined as the time at which a parent void with a mass exceeding M appears for the first time in the merger tree [Lacey and Cole 1993]. The void survival time could, for instance, be defined as the time it takes before a void is incorporated into a void of double its size. Once again, the functional forms for these quantities were already derived in Russell 2013 for the largest voids, but the objective would be to generalize this to voids of arbitrary size.

In conclusion, the study of cosmic voids unveils the awe-inspiring tapestry of the universe's grand design. These vast chasms, where emptiness and darkness hold sway, provide an underresearched decor for understanding the universe. Cosmic voids are celestial laboratories, where the cosmic dance of gravity and expansion draws clear parallels and contrasts with the overdense halos. Through the exploration of their formation, evolution, and statistical properties, a heroic quest to unravel the mysteries of the universe awaits.

Bibliography

Bond, J. R. and Myers, S. T. (Mar. 1996). “The Peak-Patch Picture of Cosmic Catalogs. I. Algorithms”. In: *Astrophysical Journal Supplement Series* 103, pp. 1–1. DOI: `10.1086/192267`.

Gunn, J. E. and Gott J. Richard, I. (Aug. 1972). “On the Infall of Matter Into Clusters of Galaxies and Some Effects on Their Evolution”. In: *The Astrophysical Journal* 176, p. 1. DOI: `10.1086/151605`.

Press, W. H. and Schechter, P. L. (Feb. 1974). “Formation of Galaxies and Clusters of Galaxies by Self-Similar Gravitational Condensation”. In: *The Astrophysical Journal* 187, pp. 425–425. DOI: `10.1086/152650`.

Bardeen, J. M. et al. (May 1986). “The Statistics of Peaks of Gaussian Random Fields”. In: *The Astrophysical Journal* 304, p. 15. DOI: `10.1086/164143`.

Bond, J. R. et al. (Oct. 1991). “Excursion set mass functions for hierarchical Gaussian fluctuations”. In: 379, pp. 440–440. DOI: `10.1086/170520`.

Sheth, R. K. and Van de Weygaert, R. (May 2004). “A hierarchy of voids: much ado about nothing”. In: 350, pp. 517–538. DOI: `10.1111/j.1365-2966.2004.07661.x`.

Van de Weygaert, R. and Van Platen, E. (Dec. 2009). “Cosmic Voids: structure, dynamics and galaxies”. In: 01, pp. 41–66. DOI: `10.1142/s2010194511000092`.

Lacey, C. and Cole, S. (Dec. 1993). “Merger Rates in Hierarchical Models of Galaxy Formation”. In: *Monthly Notices of the Royal Astronomical Society* 271, pp. 676–692. DOI: `10.1093/mnras/271.3.676`.

Russell, E. (Dec. 2013). “Merging tree algorithm of growing voids in self-similar and CDM models”. In: 436, pp. 3525–3546. DOI: `10.1093/mnras/stt1830`.

Peebles, P. J. E. (1980). *Large-Scale Structure Of The Universe.* Princeton University Press.

Allen, S. W., Evrard, A. E., and Mantz, A. B. (Sept. 2011). “Cosmological Parameters from Observations of Galaxy Clusters”. In: *Annual Review of Astronomy and Astrophysics* 49, pp. 409–470. DOI: `10.1146/annurev-astro-081710-102514`.

Hoessel, J. G., Gunn, J. P., and Thuan, T. X. (Oct. 1980). “The photometric properties of brightest cluster galaxies. I - Absolute magnitudes in 116 nearby Abell clusters”. In: 241, pp. 486–486. DOI: `10.1086/158363`.

Bahcall, N. A. and Soneira, R. M. (July 1983). “The spatial correlation function of rich clusters of galaxies.” In: *The Astrophysical Journal* 270, 20â€“38. DOI: `10.1086/161094`.

Voit, G. M. (Apr. 2005). “Tracing cosmic evolution with clusters of galaxies”. In: *Reviews of Modern Physics* 77, pp. 207–258. DOI: `10.1103/revmodphys.77.207`.

Ryden, B. (2017). *Introduction to Cosmology.* Cambridge University Press.

Fabian, A. C. (Jan. 1992). *Clusters and Superclusters of Galaxies.* DOI: `10.1007/978-94-011-2482-9`.

Sparke, L. S. and Gallagher, J. S. (Feb. 2007). *Galaxies in the Universe.* Cambridge University Press.

Kirshner, R. P. et al. (Sept. 1981). “A million cubic megaparsec void in Bootes ?” In: *The Astrophysical Journal* 248, L57â€“L60. DOI: `10.1086/183623`.

Geller, M. J. and Huchra, J. P. (Nov. 1989). “Mapping the Universe”. In: *Science* 246, pp. 897–903. DOI: `10.1126/science.246.4932.897`.

da, N. et al. (Mar. 1994). “A complete southern sky redshift survey”. In: 424, pp. L1–L1. DOI: `10.1086/187260`.

Van de Weygaert, R. and Bond, J. R. (Jan. 2008). “Observations and Morphology of the Cosmic Web”. In: pp. 409–468. DOI: `10.1007/978-1-4020-6941-3_11`.

Pisani, A., Massara, E., and Spergel, D. N. (Mar. 2019). “Cosmic voids: a novel probe to shed light on our Universe”. In.

Adler, R. J. (Jan. 2009). *The Geometry of Random Fields.* SIAM.

Guth, A. H. (Jan. 1981). “Inflationary universe: A possible solution to the horizon and flatness problems”. In: *Physical Review D* 23, pp. 347–356. DOI: `10.1103/physrevd.23.347`.

Linde, A. (Feb. 1982). “A new inflationary universe scenario: A possible solution of the horizon, flatness, homogeneity, isotropy and primordial monopole problems”. In: *Physics Letters B* 108, pp. 389–393. DOI: `10.1016/0370-2693(82)91219-9`.

Hawking, S. W. (Sept. 1982). “The development of irregularities in a single bubble inflationary universe”. In: *Physics Letters B* 115, pp. 295–297. DOI: `10.1016/0370-2693(82)90373-2`.

Starobinsky, A. (Nov. 1982). “Dynamics of phase transition in the new inflationary universe scenario and generation of perturbations”. In: *Physics Letters B* 117, pp. 175–178. DOI: `10.1016/0370-2693(82)90541-x`.

Liddle, A. and Lyth, D. H. (Apr. 2000). “Cosmological Inflation and Large-Scale Structure”. In: DOI: `10.1017/cbo9781139175180`.

Brandenberger, R. (Mar. 2011). “Introduction to Early Universe Cosmology”. In: DOI: `10.22323/1.124.0001`.

Peacock, J. A. (1999). *Cosmological physics.* Cambridge University Press.

Rubi, J. and Bedeaux, D. (Oct. 1988). “Brownian motion in a fluid in elongational flow”. In: 53, pp. 125–136. DOI: `10.1007/bf01011549`.

Cardy, J. (Apr. 1996). *Scaling and Renormalization in Statistical Physics.* Cambridge University Press.

Katok, A. and Hasselblatt, B. (1995). *Introduction to the modern theory of dynamical systems.* Cambridge University Press.

Shutta, K. H. et al. (Sept. 2022). “Gaussian graphical models with applications to omics analyses”. In: *Statistics in Medicine* 41, pp. 5150–5187. DOI: `10.1002/sim.9546`.

Roth, S. and Black, M. M. (June 2005). “Fields of Experts: A Framework for Learning Image Priors”. In: *Computer Vision and Pattern Recognition.* DOI: `10.1109/cvpr.2005.160`.

Boykov, Y. and Funka-Lea, G. (Nov. 2006). “Graph Cuts and Efficient N-D Image Segmentation”. In: *International Journal of Computer Vision* 70, pp. 109–131. DOI: `10.1007/s11263-006-7934-5`.

Van de Weygaert, R. (2020). *Stochastic Primordial Density Field: Starting Conditions.*

Coles, P. (2014). *Large-scale Structure, Theory and Statistics.* ned.ipac.caltech.edu.

Narayanan, V. and Croft, R. (June 1998). “Recovering the Primordial Density Fluctuations: A Comparison of Methods”. In: 515, pp. 471–486. DOI: `10.1086/307040`.

Scoccimarro, R. (2021). *Gaussian Random Fields.*

Wiener, N. (1930). “Generalized harmonic analysis”. In: *Acta Mathematica* 55, pp. 117–258. DOI: `10.1007/bf02546511`.

Champeney, D. C. (Aug. 1987). *A Handbook of Fourier Theorems.* Cambridge University Press.

Einstein, A. (Jan. 1914). "Methode pour la determination de valeurs statistiques d'observations concernant des grandeurs soumises a des fluctuations irregulires". In: *Archives des Sciences* 37, pp. 254–256.

Harrison, E. R. (May 1970). "Fluctuations at the Threshold of Classical Cosmology". In: *Physical Review D* 1, pp. 2726–2730. DOI: `10.1103/physrevd.1.2726`.

Zeldovich, Y. (Oct. 1972). "A Hypothesis, Unifying the Structure and the Entropy of the Universe". In: 160, 1P–3P. DOI: `10.1093/mnras/160.1.1p`.

Coles, P. and Lucchin, F. (1995). *Cosmology: The Origin and Evolution of Cosmic Structure, Second Edition.* John Wiley, p. 512.

Planck Collaboration (Oct. 2019). "Planck 2018 results. X. Constraints on inflation". In: *Astronomy & Astrophysics.* DOI: `10.1051/0004-6361/201833887`.

Burenin, R. A. (Nov. 2018). "Measurements of the Matter Density Perturbation Amplitude from Cosmological Data". In: *Astronomy Letters* 44, pp. 653–663. DOI: `10.1134/s1063773718110038`.

Planck Collaboration (Apr. 2020a). "Planck 2018 results. VI. Cosmological parameters". In: *Astronomy & Astrophysics.* DOI: `10.1051/0004-6361/201833910`.

Mo, H., Van den Bosch, F., and White, S. (2010). *Galaxy formation and evolution.* Cambridge University Press.

Weinberg, D. H. et al. (Feb. 2015). "Cold dark matter: Controversies on small scales". In: *Proceedings of the National Academy of Sciences* 112, pp. 12249–12255. DOI: `10.1073/pnas.1308716112`.

Nadler, E. O. et al. (June 2019). "Constraints on Dark Matter Microphysics from the Milky Way Satellite Population". In: 878, pp. L32–L32. DOI: `10.3847/2041-8213/ab1eb2`.

Fraternali, F. (2023). *Notes on Astrophysical Hydrodynamics.*

Van de Weygaert, R. (2004a). *Linear Perturbation Theory.*

— (2004b). *Going Nonlinear: Progressing Complexity.*

Dodelson, S. (2003). *Modern cosmology.* Academic Press.

Padmanabhan, T. (1999). *Structure formation in the universe.* Cambridge University Press.

Van de Weygaert, R. (1995). *Spherical Model Notebook: Void Evolution.*

Padmanabhan, T. (Sept. 1996). *Cosmology and Astrophysics Through Problems.* Cambridge University Press.

Straumann, N. (Nov. 2014). *General Relativity.* Springer.

Newton, I. (1687). *Philosophia naturalis principia mathematica.* Watchmaker.

Arens, R. (Jan. 1990). "Newton's observations about the field of a uniform thin spherical shell". In: 10, pp. 39–45. DOI: `10.1285/i15900932v10supn1p39`.

Lyth, D. H. and Liddle, A. R. (June 2009). *The Primordial Density Perturbation: Cosmology, Inflation and the Origin of Structure.*

Shi, X. (2017). *Self-similar Spherical Collapse.*

Van den Bosch, F. (2022). *Lecture Notes: Non-Linear Collapse & Virialization.*

Fillmore, J. A. and Goldreich, P. (June 1984). "Self-similar gravitational collapse in an expanding universe". In: *The Astrophysical Journal* 281, p. 1. DOI: `10.1086/162070`.

Williams, L., Babul, A., and Dalcanton, J. J. (Mar. 2004). "Investigating the Origins of Dark Matter Halo Density Profiles". In: 604, pp. 18–39. DOI: `10.1086/381722`.

Del Popolo, A., Pace, F., and Lima, J. (Jan. 2013). "Spherical collapse model with shear and angular momentum in dark energy cosmologies". In: 430, pp. 628–637. DOI: `10.1093/mnras/sts669`.

Bertschinger, E. (May 1985). "Self-similar secondary infall and accretion in an Einstein-de Sitter universe". In: 58, pp. 39–39. DOI: `10.1086/191028`.

Hoffman, Y. A. and Shaham, J. (Oct. 1985). "Local density maxima - Progenitors of structure". In: *The Astrophysical Journal* 297, p. 16. DOI: `10.1086/163498`.

Avila-Reese, V., Firmani, C., and Hernandez, X. (Sept. 1998). "On the Formation and Evolution of Disk Galaxies: Cosmological Initial Conditions and the Gravitational Collapse". In: *The Astrophysical Journal* 505, pp. 37–49. DOI: `10.1086/306136`.

Ryden, B. S. and Gunn, J. E. (July 1987). "Galaxy formation by gravitational collapse". In: *The Astrophysical Journal* 318, p. 15. DOI: `10.1086/165349`.

Subramanian, K., Cen, R., and Ostriker, J. P. (Aug. 2000). "The Structure of Dark Matter Halos in Hierarchical Clustering Theories". In: *The Astrophysical Journal* 538, pp. 528–542. DOI: `10.1086/309152`.

Ascasibar, Y. et al. (Aug. 2004). "On the physical origin of dark matter density profiles". In: 352, pp. 1109–1120. DOI: `10.1111/j.1365-2966.2004.08005.x`.

Hoffman, Y. (Sept. 1986). "The dynamics of superclusters - The effect of shear". In: *The Astrophysical Journal* 308, p. 493. DOI: `10.1086/164520`.

Zaroubi, S. and Hoffman, Y. (Oct. 1993). "Gravitational Collapse in an Expanding Universe: Asymptotic Self-similar Solutions". In: *The Astrophysical Journal* 416, p. 410. DOI: `10.1086/173246`.

Lacey, C. and Cole, S. (Dec. 1994). "Merger rates in hierarchical models of galaxy formation. Part II: Comparison with N-body simulations". In: *Monthly Notices of the Royal Astronomical Society* 271, pp. 676–692. DOI: `10.1093/mnras/271.3.676`.

Sheth, R. K. and Tormen, G. (Sept. 1999). "Large-scale bias and the peak background split". In: *Monthly Notices of the Royal Astronomical Society* 308, pp. 119–126. DOI: `10.1046/j.1365-8711.1999.02692.x`.

Doroshkevich, A. G. (Jan. 1970). "The space structure of perturbations and the origin of rotation of galaxies in the theory of fluctuation." In: 6, pp. 581–600.

White, S. and Silk, J. (1979). "231 IW". In: *The Astrophysical Journal* 231, pp. 1–9.

Eisenstein, D. J. and Loeb, A. (Feb. 1995). "An analytical model for the triaxial collapse of cosmological perturbations". In: *The Astrophysical Journal* 439, p. 520. DOI: `10.1086/175193`.

Sheth, R. K., Mo, H. J., and Tormen, G. (May 2001). "Ellipsoidal collapse and an improved model for the number and spatial distribution of dark matter haloes". In: *Monthly Notices of the Royal Astronomical Society* 323, pp. 1–12. DOI: `10.1046/j.1365-8711.2001.04006.x`.

Icke, V. (Jan. 1984). "Voids and filaments". In: 206, 1P–3P. DOI: `10.1093/mnras/206.1.1p`.

Ryden, B. S. and Peterson, B. M. (2011). *Foundations of astrophysics.* Pearson.

Aragon-Calvo, M. A. and Szalay, A. S. (Feb. 2013). "The hierarchical structure and dynamics of voids". In: 428, pp. 3409–3424. DOI: `10.1093/mnras/sts281`.

Centrella, J. and Melott, A. L. (Sept. 1983). "Three-dimensional simulation of large-scale structure in the Universe". In: *Nature* 305, pp. 196–198. DOI: `10.1038/305196a0`.

Foster, C. and Nelson, L. (June 2009). "The Size, shape and Orientation of Cosmological Voids in the SLOAN Digitial Sky Survey". In: 699, pp. 1252–1260. DOI: `10.1088/0004-637x/699/2/1252`.

Van Platen, E., Van de Weygaert, R., and Jones, B. (June 2008). "Alignment of voids in the cosmic web". In: 387, pp. 128–136. DOI: `10.1111/j.1365-2966.2008.13019.x`.

Park, D. and Lee, J. (Feb. 2007). "Void Ellipticity Distribution as a Probe of Cosmology". In: *Physical Review Letters* 98. DOI: `10.1103/physrevlett.98.081301`.

Shandarin, S. F. et al. (Apr. 2006). "Shapes and sizes of voids in the Lambda cold dark matter universe: excursion set approach". In: 367, pp. 1629–1640. DOI: `10.1111/j.1365-2966.2006.10062.x`.

Colberg, J. M., Krughoff, K. S., and Connolly, A. J. (May 2005). "Intercluster filaments in a CDM Universe". In: 359, pp. 272–282. DOI: `10.1111/j.1365-2966.2005.08897.x`.

Mathis, H. and White, S. D. M. (Dec. 2002). “Voids in the simulated local Universe”. In: *Monthly Notices of the Royal Astronomical Society* 337, pp. 1193–1206. DOI: `10.1046/j.1365-8711.2002.06010.x`.

Jedamzik, K. (July 1995). “The Cloud-in-Cloud Problem in the Press-Schechter Formalism of Hierarchical Structure Formation”. In: DOI: `10.1086/175936`.

Planck Collaboration (Sept. 2020b). “Planck 2018 results. VIII. Gravitational lensing”. In.

Van de Weygaert, R. (2004c). *Hierarchical Structure Formation: Press-Schechter Formalism.*

Cole, S. and Kaiser, N. (Apr. 1989). “Biased clustering in the cold dark matter cosmogony”. In: *Monthly Notices of the Royal Astronomical Society* 237, pp. 1127–1146. DOI: `10.1093/mnras/237.4.1127`.

White, S. D. M. and Frenk, C. S. (Sept. 1991). “Galaxy formation through hierarchical clustering”. In: *The Astrophysical Journal* 379, p. 52. DOI: `10.1086/170483`.

Kauffmann, G., White, S. D. M., and Guiderdoni, B. (Sept. 1993). “The formation and evolution of galaxies within merging dark matter haloes*”. In: *Monthly Notices of the Royal Astronomical Society* 264, pp. 201–218. DOI: `10.1093/mnras/264.1.201`.

Zhan, Y. (1990). “The mass function of galaxy clusters”. In: *The Astrophysical Journey* 355.

Bartlett, J. G. and Silk, J. (Apr. 1993). “Galaxy clusters and the COBE result”. In: *The Astrophysical Journal* 407, p. L45. DOI: `10.1086/186802`.

Kauffmann, G. and Charlot, S. (Aug. 1994). “Constraints on models of galaxy formation from the evolution of damped Lyman alpha absorption systems”. In: *The Astrophysical Journal* 430, p. L97. DOI: `10.1086/187447`.

Mo, H. J. and Miralda-Escude, J. (July 1994). “Damped Lyman-alpha systems and galaxy formation”. In: *The Astrophysical Journal* 430, p. L25. DOI: `10.1086/187429`.

Rodrigues, D. D. and Thomas, P. A. (1996). “Halo evolution in Hierarchical Cosmogonies”. In: *ASP Conference Series* 92.

Bower, R. G. (Jan. 1991). “The evolution of groups of galaxies in the Press-Schechter formalism”. In: 248, pp. 332–352. DOI: `10.1093/mnras/248.2.332`.

Chandrasekhar, S. (Jan. 1943). “Stochastic Problems in Physics and Astronomy”. In: *Reviews of Modern Physics* 15, pp. 1–89. DOI: `10.1103/revmodphys.15.1`.

Furlanetto, S. R., Zaldarriaga, M., and Hernquist, L. (Sept. 2004). “The Growth of HII Regions During Reionization”. In: *The Astrophysical Journal* 613, pp. 1–15. DOI: `10.1086/423025`.

Lin, Y. et al. (June 2016). “The distribution of bubble sizes during reionization”. In: *Monthly Notices of the Royal Astronomical Society* 461, pp. 3361–3374. DOI: `10.1093/mnras/stw1542`.

McQuinn, M. et al. (May 2007). “The morphology of H II regions during reionization”. In: *Monthly Notices of the Royal Astronomical Society* 377, pp. 1043–1063. DOI: `10.1111/j.1365-2966.2007.11489.x`.

McQuinn, M. et al. (Sept. 2005). “The Kinetic Sunyaev-Zelovich Effect from Reionization”. In: 630, pp. 643–656. DOI: `10.1086/432049`.

Zahn, O. et al. (Sept. 2005). “The Influence of Nonuniform Reionization on the CMB”. In: 630, pp. 657–666. DOI: `10.1086/431947`.

Iliev, I. T. et al. (Dec. 2006a). “kSZ from patchy reionization: The view from the simulations”. In: *New Astronomy Reviews* 50, pp. 909–917. DOI: `10.1016/j.newar.2006.09.012`.

Iliev, I. T. et al. (June 2006b). “Simulating cosmic reionization at large scales - I. The geometry of reionization”. In: *Monthly Notices of the Royal Astronomical Society* 369, pp. 1625–1638. DOI: `10.1111/j.1365-2966.2006.10502.x`.

Zahn, O. et al. (Jan. 2007). “Simulations and Analytic Calculations of Bubble Growth during Hydrogen Reionization”. In: *The Astrophysical Journal* 654, pp. 12–26. DOI: `10.1086/509597`.

Mesinger, A. and Furlanetto, S. (Nov. 2007). “Efficient Simulations of Early Structure Formation and Reionization”. In: *The Astrophysical Journal* 669, pp. 663–675. DOI: `10.1086/521806`.

Zahn, O. et al. (Apr. 2011). “Comparison of reionization models: radiative transfer simulations and approximate, seminumeric models”. In: *Monthly Notices of the Royal Astronomical Society* 414, pp. 727–738. DOI: `10.1111/j.1365-2966.2011.18439.x`.

Shen, J. et al. (July 2006). “An Excursion Set Model of the Cosmic Web: The Abundance of Sheets, Filaments, and Halos”. In: 645, pp. 783–791. DOI: `10.1086/504513`.

Sheth, R. K. and Lemson, G. (Apr. 1999). “Biasing and the distribution of dark matter haloes”. In: 304, pp. 767–792. DOI: `10.1046/j.1365-8711.1999.02378.x`.

Somerville, R. S. and Kolatt, T. S. (May 1999). “How to plant a merger tree”. In: 305, pp. 1–14. DOI: `10.1046/j.1365-8711.1999.02154.x`.

Cole, S. et al. (Apr. 2000). “Hierarchical galaxy formation”. In: *Monthly Notices of the Royal Astronomical Society* 319, pp. 168–204. DOI: `10.1046/j.1365-8711.2000.03879.x`.

Neistein, E. and Dekel, A. (Aug. 2008). “Merger rates of dark matter haloes”. In: 388, pp. 1792–1802. DOI: `10.1111/j.1365-2966.2008.13525.x`.

Jennings, E., Li, Y., and Hu, W. (Apr. 2013). “The abundance of voids and the excursion set formalism”. In: 434, pp. 2167–2181. DOI: `10.1093/mnras/stt1169`.

Aikio, J. and Mahonen, P. (Apr. 1998). “A Simple Void-searching Algorithm”. In: *The Astrophysical Journal* 497, pp. 534–540. DOI: `10.1086/305509`.

Einasto, J., Einasto, M., and Gramann, M. (May 1989). “Structure and formation of superclusters -IX. Self-similarity of voids.” In: *Monthly Notices of the Royal Astronomical Society* 238, pp. 155–177. DOI: `10.1093/mnras/238.1.155`.

Ryden, B. S. (Oct. 1995). “Measuring Q0 from the Distortion of Voids in Redshift Space”. In: *The Astrophysical Journal* 452, p. 25. DOI: `10.1086/176277`.

Ryden, B. S. and Melott, A. L. (Oct. 1996). “Voids in Real Space and in Redshift Space”. In: *The Astrophysical Journal* 470, p. 160. DOI: `10.1086/177857`.

Appendix A: Figures

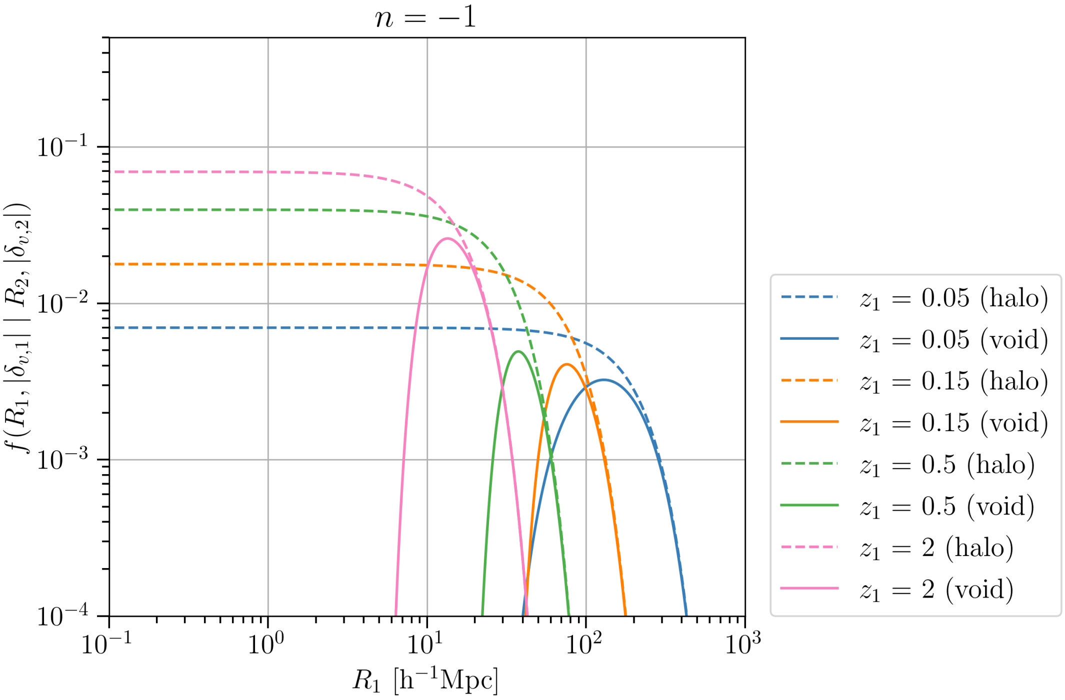

Figure A.11: Conditional void size distribution. The plot shows the conditional probability of a void of size R_1 at time $\delta_{v,1} = \delta_v(1 + z_1)$ later being merged into a void of size $R_2 = 2R_1$ at time $\delta_{v,2} = \delta_v$, as calculated in Eq. 5.16 with a universe in which $n = -1$. A characteristic radius of $R_* = 8\,\mathrm{h}^{-1}$Mpc and $\sigma_8 = 0.8$ were chosen for normalisation. The dashed lines represent the result for halos, the solid curves the same configuration but then for voids. The exponential cut-off for halos at large radii is also apparent for the voids. Note how this decay moves to higher radii for more recent redshifts, which is indicative of hierarchical structure formation. A second cut-off at relatively low radii is unique to voids and stems from the void-in-cloud problem.

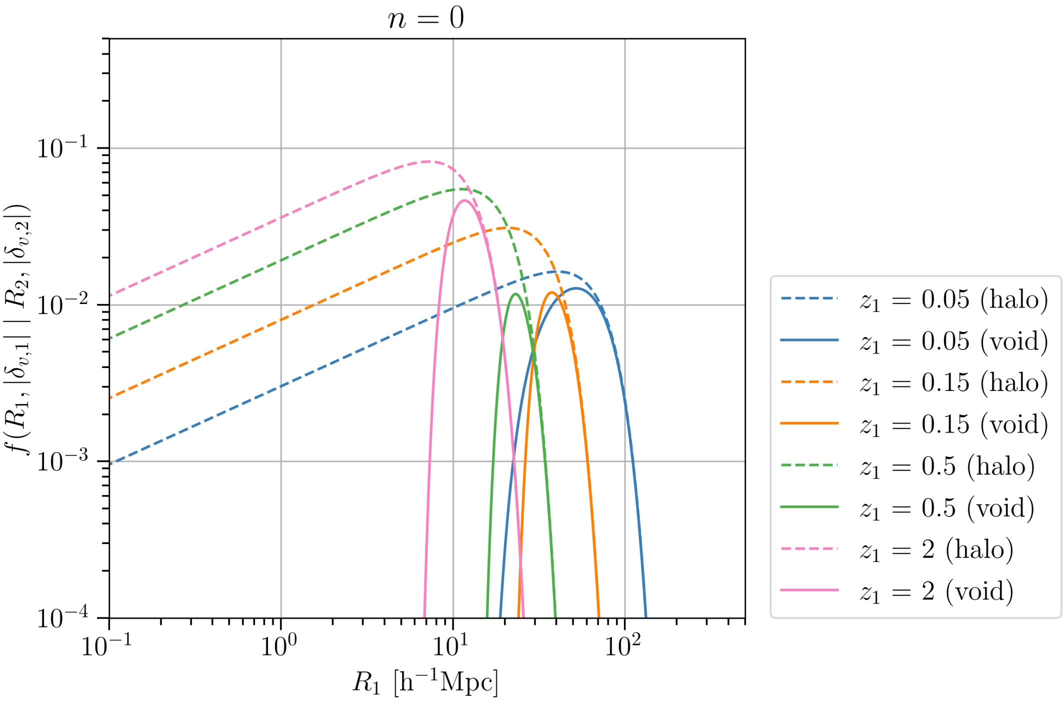

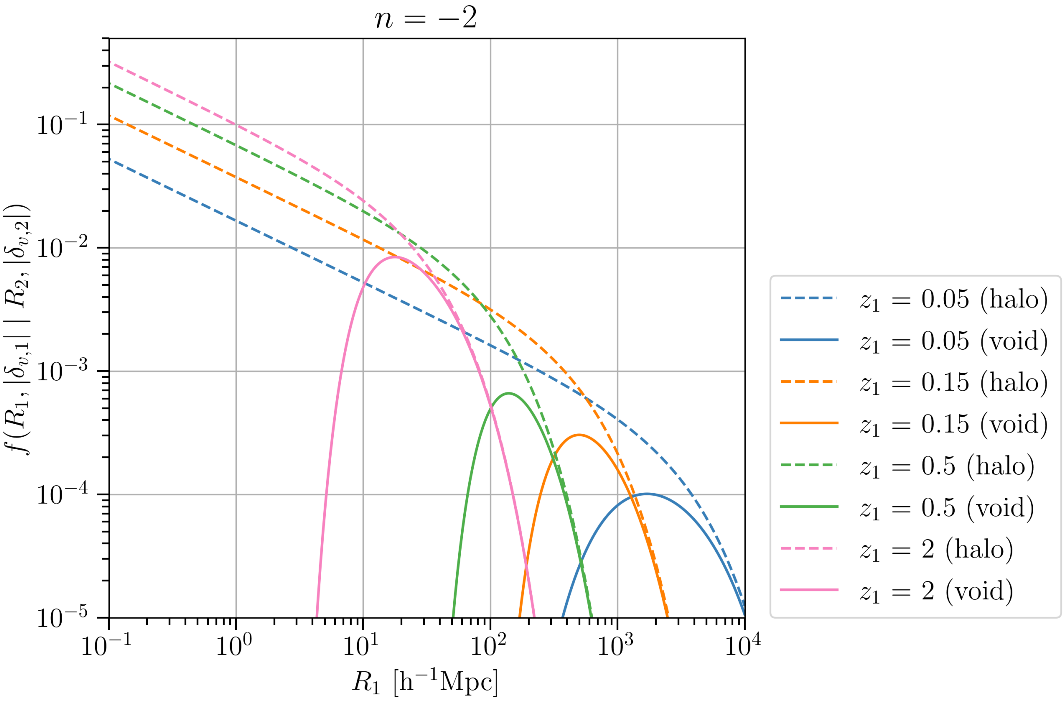

Figure A.12: The conditional probability of a void of size R_1 at time $\delta_{v,1} = \delta_v(1 + z_1)$ later being merged into a void of size $R_2 = 2R_1$ at time $\delta_{v,2} = \delta_v$, as calculated in Eq. 5.16. The figure at the top corresponds to a pure power law universe with $n = 0$, while the bottom figure corresponds to $n = -2$.

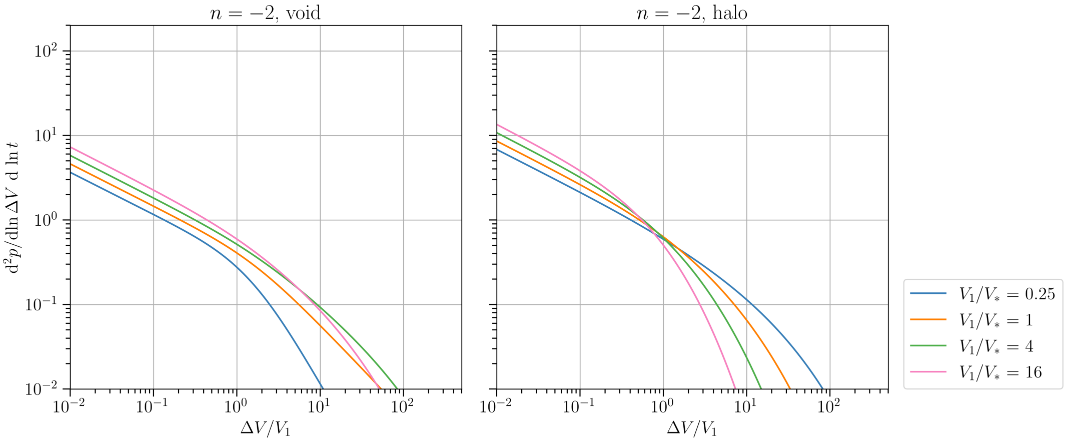

Figure A.13: The void merging rate as predicted by Eq. 5.19, against the same result for halos in an $n = -2$ universe.

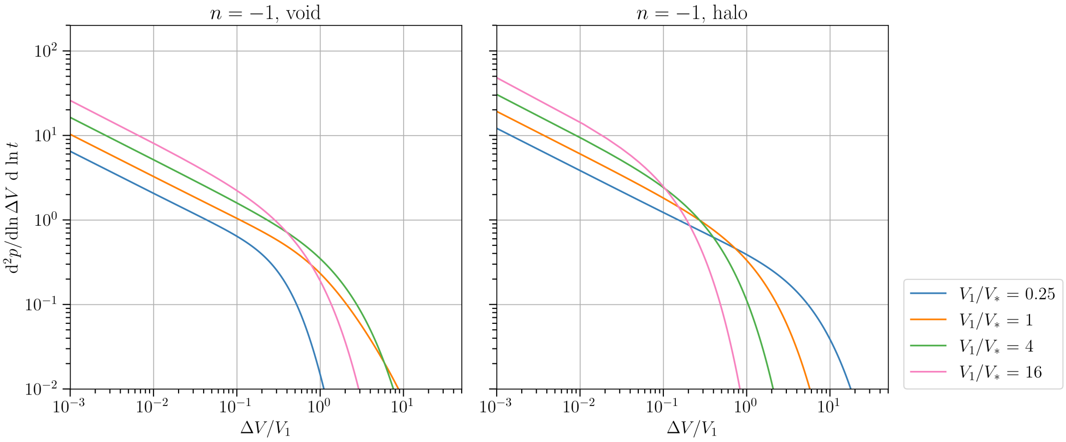

Figure A.14: The void merging rate as predicted by Eq. 5.19, against the same result for halos in an $n = -1$ universe.

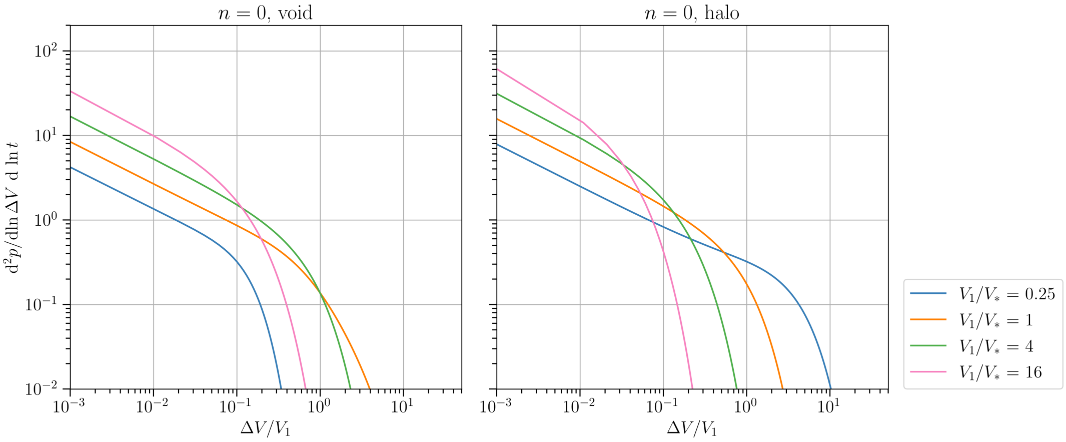

Figure A.15: The void merging rate as predicted by Eq. 5.19, against the same result for halos in an $n = 0$ universe.

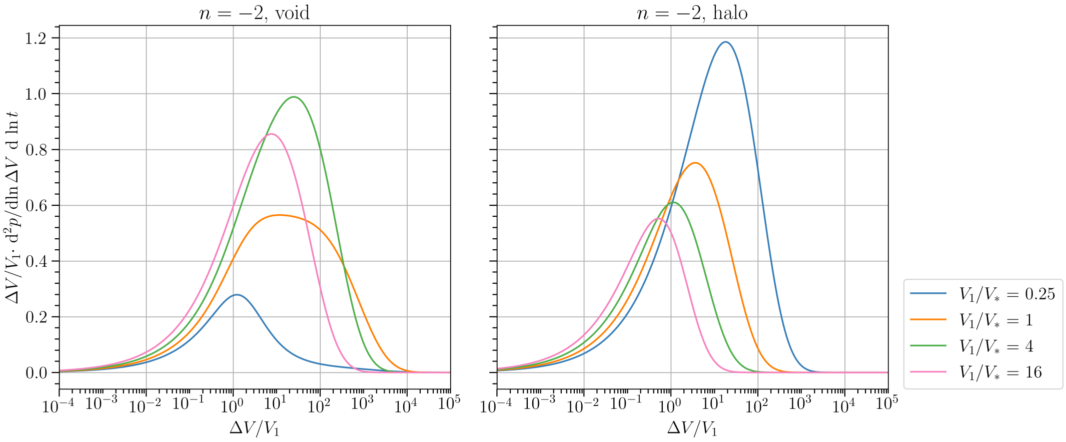

Figure A.16: The void absorption rate as predicted by Eq. 5.20, against the same result for halos, against the same result for halos in an $n=-2$ universe.

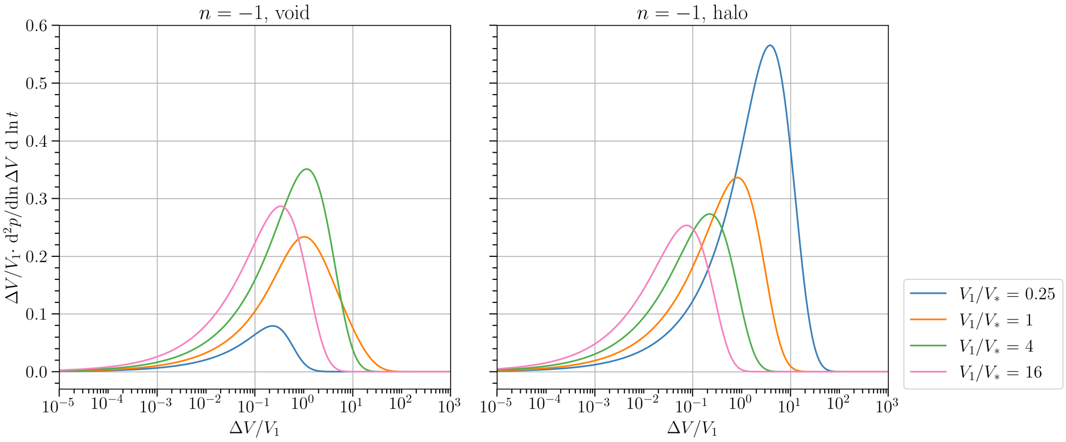

Figure A.17: The void absorption rate as predicted by Eq. 5.20, against the same result for halos, against the same result for halos in an $n=-1$ universe.

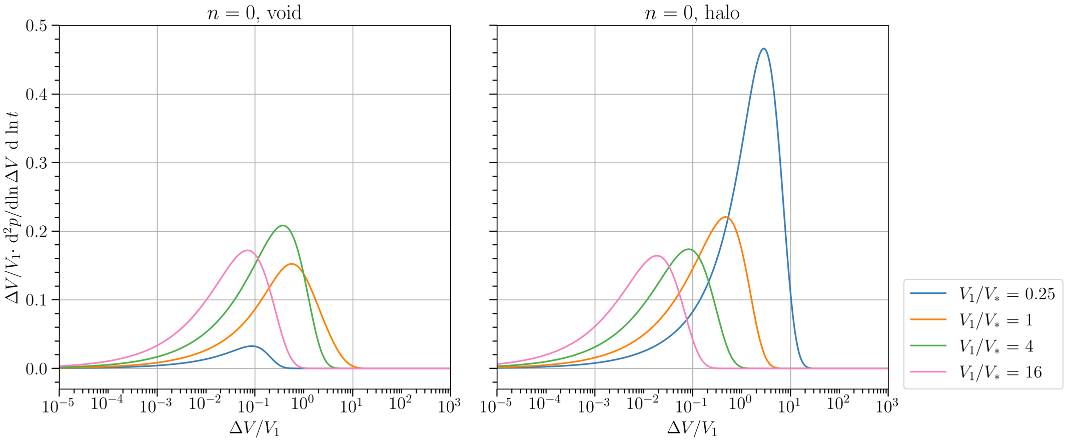

Figure A.18: The void absorption rate as predicted by Eq. 5.20, against the same result for halos, against the same result for halos in an $n=0$ universe.